

# Chapter 2

## Flexural Motion Due to Laser Heating Applications

**Abstract** Laser evaporative heating of solid surfaces involves phase change process and recoil pressure generation in between the vapor and liquid phases. Recoil pressure remains high during a short period of time, which in turn causes mechanical vibration of the body irradiated by a laser beam. When the body resembles a cantilever arrangement and if the laser radiation takes place at the free end of the cantilever beam, the body undergoes a flexural motion. Depending on the laser pulse intensity and duration, the displacement characteristics of the cantilever beam provide information on the mechanical properties of the irradiated beam. In this chapter, laser pulse heating is formulated and thermal stress developed in the heated region is analyzed. In addition, flexural behavior of the cantilever beam is presented in detail.

**Keywords** Laser heating • Temperature • Stress • Flexural motion

### 2.1 Laser Induced Evaporation Process

In the analysis of the flexural characteristics of the beam, the formulation and findings of the previous study [1] are considered.

Consider the flexural wave generated during the laser ablation of steel surface. The pressure rise at the interface zone can be translated into a force acting normal to the surface of the substrate. The resulting force is then considered to generate flexural waves along the substrate. In the following, the pressure rise at the surface during the laser-workpiece interaction is formulated and wave equations are solved numerically to obtain the flexural wave characteristics due to the normal pressure force.

#### 2.1.1 Temperature and Pressure

The analytical solution is limited to the temperature range where the plasma formation is negligible as compared to vapor emission from the surface.

### 2.1.1.1 Surface Temperature

The surface temperature of the evaporating surface can be written as [2]

$$T_s = \frac{I_0 \alpha}{k V} - \frac{\alpha \rho L_v}{k} \quad (2.1)$$

where  $I_0$  is the peak power intensity and  $V$  is the velocity of the surface, which is

$$V = \left( \frac{k_B T_s}{2\pi m} \right)^{1/2} \exp\left( -\frac{m L_v}{k_B T_s} \right) \quad (2.2)$$

where  $m$  is the mass of an atom,  $k_B$  is Boltzmann's constant, and  $L_v$  is latent heat of evaporation.

### 2.1.1.2 Interface Pressure

The pressure acting on the surface is taken as the time averaged rate of momentum change which, although it might appear dubious in view of the small periods of time over which the surface ablates, correlates reasonably well with measured results [3]. When omitting the aggregation of substrate vapor above the target surface and the expulsion of liquid globules, the recoil pressure (which is the pressure that was generated in the interface of evaporated surface and acted onto the substrate) can be formulated through the conservation of momentum. Denoting the surface recession velocity as  $V_s$  (Fig. 2.1a), mass continuity requires

$$\rho_s V_s = \rho_v (V_v + V_s), \quad (2.3)$$

where  $v$  and  $s$  refer to the vapor and the liquid phases at interface, respectively. The momentum equation across the interface is

$$P_s + \rho_s V_s^2 = P_v + \rho_s V_s (V_v + V_s). \quad (2.4)$$

The recoil pressure ( $P_s$ ) can be calculated after knowing the vapor pressure, vapor density (the value is taken from the previous study [4]), recession velocity, and the liquid density (taken as the density of the substrate at the melting temperature). Consequently, determination of vapor pressure and recession velocity are necessary to determine the recoil pressure. The recoil pressure is determined from Eq. (2.4) and it is validated using the equation derived from the previous study [5] which is

$$P_s = \frac{I_v V_v}{[L_v + \frac{1}{2} V_v^2]}, \quad (2.5)$$

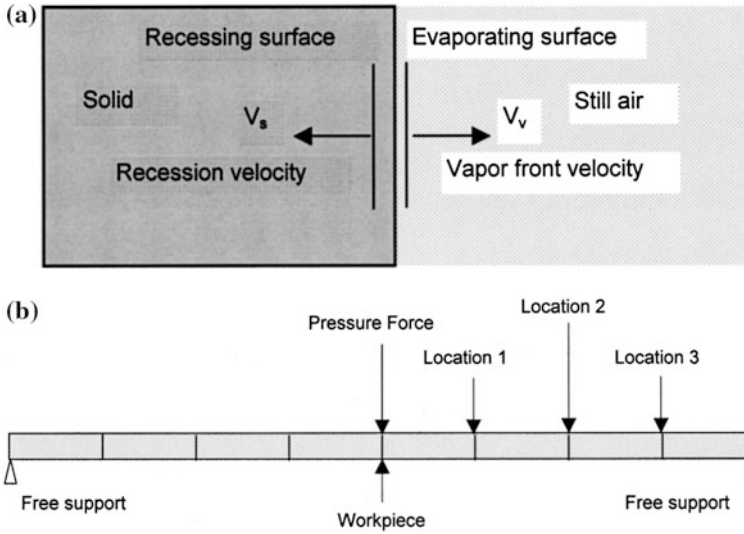


**Fig. 2.1** a Schematic view of interface. b Schematic view of workpiece and elements used in the analysis [1]

where  $I_v$  is the energy consumed during the evaporation process and it is given by

$$I_v = \int_{T_1}^T C_p dT + L_v \tag{2.6}$$

**2.1.1.3 Vapor Pressure**

The vapor expands into the still air, where the gauge pressure is zero. Hence, the vapor pressure can be written after considering the momentum equation across the vapor front and the still air as

$$P_v = \rho_s V_s V_v, \tag{2.7}$$

where  $\rho_s V_s$  is the mass flow rate. The vapor pressure predicted from Eq. (2.7) is validated using the equation given in the previous study, [6] i.e.,

$$P_v = 1.82 \times 10^{-3} \frac{\sqrt{C_p T_v I_0}}{[C_p (T_v - T_0) + L_v]} \tag{2.8}$$

The unit of Eq. (2.8) is in bar.

### 2.1.2 Wave Analysis

The solution in the wave problem is in general a function of space and time. If the time variation of the solution is focused on at a particular point in space, then it can be presented by a spectral function. The spectral formulation starts with the equations of motion of the workpiece (as free supported beam) including inertia terms.

After dividing the workpiece into a number of elements, cross-sectional area and second moment of area at the midpoint of each element can be considered as constant over the entire element. Therefore, the equation of motion can be written as [7]

$$GA\kappa \left[ \frac{\partial^2 y}{\partial x^2} - \frac{\partial \phi}{\partial x} \right] = \rho A \frac{\partial^2 y}{\partial t^2} - q \quad (2.9)$$

and

$$\frac{\partial^2 \phi}{\partial x^2} + GA\kappa \left[ \frac{\partial y}{\partial x} - \phi \right] = \rho I \frac{\partial^2 \phi}{\partial t^2} \quad (2.10)$$

The displacement and the bending slope can be written in the spectral form as [8]

$$y(x, t) = \sum_n \hat{y}_n(x, \omega_n) e^{i\omega_n t} \quad (2.11)$$

and

$$\phi(x, t) = \sum_n \hat{\phi}_n(x, \omega_n) e^{i\omega_n t} \quad (2.12)$$

The spectral component  $\hat{y}_n$  and  $\hat{\phi}_n$  have the solution as

$$\hat{y}_n = A_1 e^{-ik_1 x} + B_1 e^{-ik_2 x} + C_1 e^{ik_1 x} + D_1 e^{ik_2 x} \quad (2.13)$$

and

$$\hat{\phi}_n = A_2 e^{-ik_1 x} + B_2 e^{-ik_2 x} + C_2 e^{ik_1 x} + D_2 e^{ik_2 x} \quad (2.14)$$

where  $k_1$  and  $k_2$  are the wave numbers and  $A_1, A_2, B_1, B_2, C_1, C_2$  and  $D_1, D_2$  are the frequency dependent coefficients, which are complex in nature. The first term in Eqs. (2.13) and (2.14) represent the waves moving in the forward direction while the last two describe the backward moving waves.

Substituting  $\hat{y}_n$  and  $\hat{\phi}_n$  in Eqs. (2.9) and (2.10), and considering the load to be applied at the modes, yields

$$\begin{aligned}
GA\kappa(-k_1^2 A_1 + ik_1 A_2) &= -\omega^2 \rho A(-A_1) \\
GA\kappa(-k_1^2 B_1 + ik_1 B_2) &= -\omega^2 \rho A(-B_1) \\
GA\kappa(-k_1^2 C_1 + ik_1 C_2) &= -\omega^2 \rho A(-C_1) \\
GA\kappa(-k_1^2 D_1 + ik_1 D_2) &= -\omega^2 \rho A(-D_1)
\end{aligned} \tag{2.15}$$

where the coefficients

$$\begin{aligned}
A_2 &= \left[ \frac{-\omega^2 \rho A + k_1^2 GA\kappa}{ik_1 GA\kappa} \right] A_1, & B_2 &= \left[ \frac{-\omega^2 \rho A + k_1^2 GA\kappa}{ik_1 GA\kappa} \right] B_1, \\
C_2 &= \left[ \frac{\omega^2 \rho A - k_1^2 GA\kappa}{ik_1 GA\kappa} \right] C_1, & D_2 &= \left[ \frac{\omega^2 \rho A - k_1^2 GA\kappa}{ik_1 GA\kappa} \right] D_1.
\end{aligned}$$

The shear force and momentum equations can be written as

$$\dot{Q} = -EI \frac{\partial^2 \hat{\phi}}{\partial x^2} - \omega^2 \rho I \hat{\phi} \tag{2.16}$$

and

$$\dot{M} = -EI \frac{\partial \hat{\phi}}{\partial x} \tag{2.17}$$

The dynamic stiffness is obtained by first relating the coefficients to the nodal displacement as

$$[A, B, C, D] = \hat{\alpha}[\hat{y}_1, \hat{\phi}_1, \hat{y}_2, \hat{\phi}_2], \tag{2.18}$$

where  $[\hat{\alpha}] = [\beta]$  and  $[\beta]^{-1}$  are given in [8].

The nodal loads are obtained by using the shear force and momentum Eqs. (2.16) and (2.17) i.e.,

$$[\hat{F}]^T = [\hat{k}][d]^T$$

where

$$[\hat{F}]^T = [\hat{Q}_1 \hat{M}_1 \dots \hat{Q}_n \hat{M}_n]$$

and

$$[d]^T = [\hat{y}_1 \hat{\phi}_1 \dots \hat{y}_n \hat{\phi}_n]$$

where n is the number of nodes.

### 2.1.2.1 Initial and Boundary Conditions

Initially the displacements and velocities are set to zero. The free supported boundary condition at the workpiece ends is considered. In this case, at free ends of the workpiece ( $x = 0$  and  $x = 1$ ), the bending moment is set to zero at all frequencies, i.e.,

$$\frac{d\hat{\phi}(I, \omega)}{dx} = 0.$$

In order to observe the effect of reflecting waves from the free ends of the workpiece, one end of the workpiece is assumed to be at infinity. This boundary condition (element extends to infinity) requires that the element behaves as a radiating beam which acts as a conduit for energy out of the system.

### 2.1.2.2 Method of Solution

In the analysis, the workpiece is divided into eight elements and each element can be treated as uniform (Fig. 2.1b). The displacement vector is then transformed from time domain into frequency domain using fast Fourier transformation (FFT). The transform response is fed back into the governing differential equations, which is solved at each frequency component using the finite element method. The transient response is recovered by using the inverse FFT. The input excitation signal, which is the load generated due to the normal component of the thermal stress, at discrete time steps needs to be converted into frequency domain by FFT. The sampling rate  $\Delta t$  must be in accordance with Nyquist frequency of the signal. The frequency step is obtained from

$$\Delta f = \frac{1}{N\Delta t}$$

where  $N$  is the number of data points in the power spectrum. The signal is bound limited between the minimum frequency ( $f_{\min}$ ) and the maximum frequency ( $f_{\max}$ ).

Beginning from the minimum frequency, the assembled dynamic stiffness matrix and the assembled load vector in frequency domain are obtained by the finite element method, i.e.,

$$[\hat{F}] = [\hat{K}][\hat{d}] \quad (2.19)$$

or

$$[\hat{d}] = [\hat{K}]^{-1}[\hat{F}]$$

**Table 2.1** Properties of steel used in the simulation and number of elements employed

E (GPa)	G (GPa)	$\rho$ (kg/m <sup>3</sup> )	$\kappa$	$\nu$	$\eta$
207	77.6	7,836	0.67	0.3	0.025

**Table 2.2** Workpiece size and number of elements used in simulations

Length (m)	Width (m)	Thickness (m)	Number of elements
1	0.2	0.002	8

After applying the boundary conditions to Eq. (2.19),  $[K]$  is inverted by the Gauss reduction method. Consequently, the response is obtained at  $f_{\min}$ . This procedure is repeated for other frequencies up to  $f_{\max}$ . Hence, the displacement vector  $[\hat{d}]$  is obtained at the desired element. The frequency dependent response is reconstructed with time domain by using the inverse Fourier transformation method. In order to improve the stability of the computation, damping is introduced through the wave number  $k$  in the form of

$$k = k_0(1 - i\eta),$$

where  $k_0$  is the undamped value and  $\eta$  is taken as 0.025. The material properties are given in Table 2.1 while workpiece size and number of elements used in the simulation are given in Table 2.2.

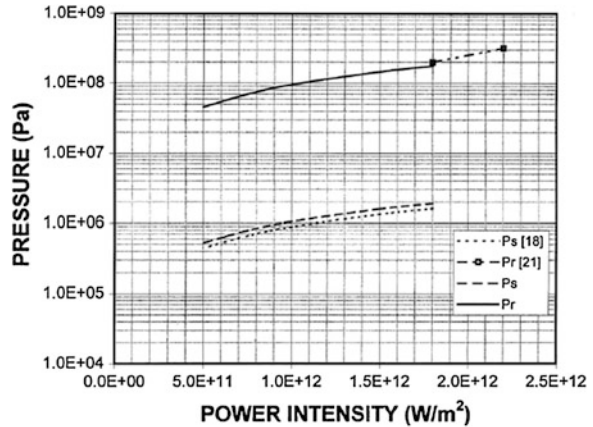
### 2.1.3 Results and Discussions

The pressure increase in the interface zone due to laser heating of the steel surface is determined. The force normal to the workpiece surface resulting from the pressure rise at the workpiece surface interface is considered to be an impulsive force generating the flexural wave motion in the workpiece. To observe the wave amplitude and frequency, three equally spaced locations in the plane of the workpiece surface are considered. In the analysis, the reflection of the traveling waves from the free ends of the workpiece is also considered. To investigate the effect of reflected waves on the traveling wave characteristics a radiating element at one end of the workpiece is considered.

Figure 2.2 shows the pressure predicted from the present study and the previous studies [4, 5]. The equation derived previously predicts the interface zone pressure to be as high as 300 MPa. The values of the pressure predicted from the present study agree well with the previous results. The small discrepancies between the findings are negligibly small.

Figure 2.3 shows the model of the temporal variation of the impulsive pressure force and the corresponding power spectrum density curve. The value of the force

**Fig. 2.2** Vapor and recoil pressures with power intensity [1]



is obtained by multiplying the pressure by the ablated surface area. It should be noted that the pressure distribution across the ablated surface is not known; therefore, it is assumed that it is uniform across the ablated surface. In the present study, the maximum frequency (Nyquist frequency) is taken as 2,000 (Fig. 2.3b). The flexural wave propagates in two modes provided that the second mode propagates faster than the first mode. In addition, the workpiece is a dispersive media, which modifies the wave characteristics during the wave propagation. Consequently, the propagating wave characteristics are modified due to dispersive media, interference of reflected waves, and overlapping of the wave modes.

Figure 2.4 shows the relative displacement of the flexural waves at the center of the workpiece. The amplitude of the displacement dies as the time progresses. This is because of the damping factor of the workpiece. The irregular wave pattern with time is due to one or all of the following facts: (i) overlapping of two modes of the wave, since the second mode propagates faster than the first mode, (ii) the reflected waves from the free ends of the workpiece modifies the wave amplitude, and (iii) the dispersive nature of the workpiece alters the wave characteristics. Moreover, as the time progresses, the wave displays a regular pattern provided that the effect of the reflected wave is evident in the tail of the wave pattern.

Figure 2.5 shows the flexural waves at three different locations at the workpiece surface. The locations are equally spaced and 12.5 cm apart. The wave amplitude is higher and has a spikey appearance in the first location at the workpiece surface, which is closer to the workpiece center where the pressure force is applied. No certain pattern is observed in the wave. In this case, the traveling wave amplitude and frequency are modified by the reflected waves from the free ends of the workpiece and by the dispersive nature of the workpiece material. As the location from the workpiece center moves toward the workpiece end, the amplitude of the wave reduces due to the damping effect of the workpiece material. The wave patterns changes, i.e., an almost regular pattern is observed after 2 ms of the propagation period at location 2. However, this time is shifted to 4 ms at location 3

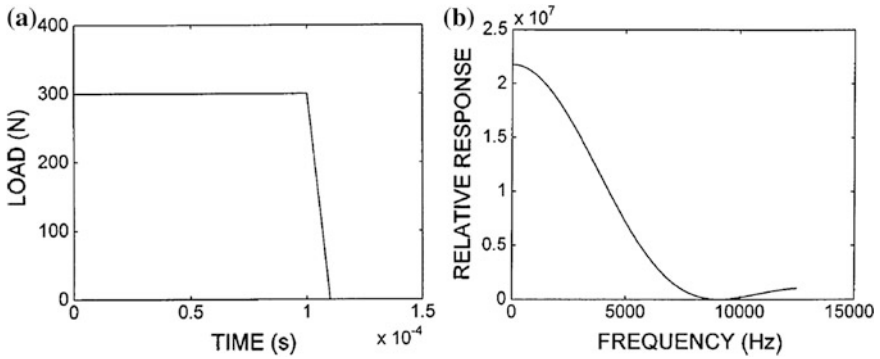


Fig. 2.3 a Temporal variation of pressure force. b Power spectrum density of pressure force [1]

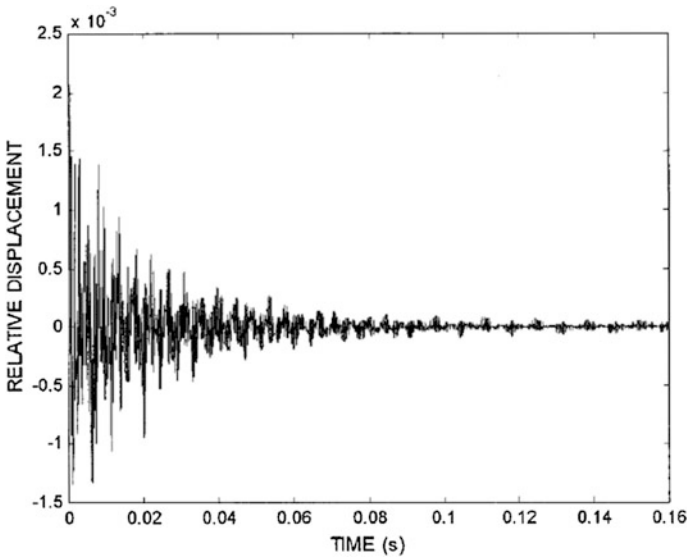


Fig. 2.4 Flexural wave motion generated at the center of the workpiece [1]

at the workpiece surface. In this case, the reflected wave interferes with the traveling wave resulting in the wave amplitude modification in the early period of wave propagation. Consequently, a common pattern in the traveling wave moves forward in time as the location at the surface moves towards the workpiece free end.

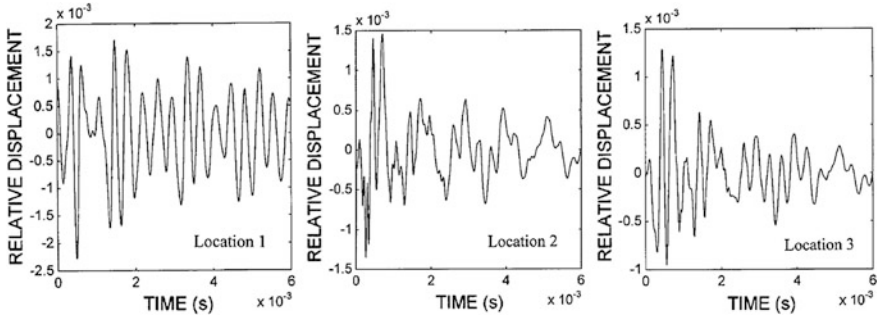


Fig. 2.5 Flexural waves at different locations at the workpiece surface [1]

## 2.2 Laser Evaporative Heating of Steel

The mathematical analysis and the findings are presented below in line with the previous study [9].

A stress field is developed during the flexural motion of workpieces when ablated by a laser beam. Consequently, when modeling the laser evaporative heating process, flexural wave motions and stress levels in the substrate material need to be included. In the following, laser evaporative heating of steel is modeled analytically. The vapor pressure generated during the evaporation process is obtained. The flexural motion and stress field in the substrate material are formulated. Consequently, the normal pressure force, the amplitude and frequency of the flexural waves and the stress levels in the substrate material are computed using the finite element method (FEM). The study is extended to include two geometric arrangements of the substrate material: a cantilever arrangement and a beam simply supported with both ends. Aluminum is introduced as an additional element in the steel in order to investigate the effect of an additional element, different to the substrate material, on displacement and on the stress field.

### 2.2.1 Heat Transfer Analysis

The Fourier heat transfer equation for a laser heating pulse can be written as

$$k \frac{\partial^2 T(x, t)}{\partial x^2} + \rho C_p V \frac{\partial T}{\partial x} + I_o (1 - r_f) \delta \exp(-\delta x) = \frac{\partial}{\partial t} [\rho C_p T(x, t)] \quad (2.20)$$

where  $r_f$  is the surface reflectivity,  $I_o$  is the power intensity of the step input pulse,  $\delta$  is the absorption depth,  $\rho$  is the density,  $C_p$  is the specific heat capacity,  $k$  is the

thermal conductivity, and  $V$  is the recession velocity of the surface, which can be determined from the energy balance at the surface [2], i.e.,

$$V = \frac{I_o}{\rho(CpT + L_{ev})} \quad (2.21)$$

where  $L_{ev}$  is the latent heat of evaporation. It should be noted that in Eq. (2.20), a laser step-input intensity pulse is considered, i.e. intensity does not vary with time, and therefore,  $I_o$  is constant. The initial and boundary conditions are as follows:

At

$$t = 0 \quad T(x, 0) = 0$$

and at the surface

$$\left. \frac{\partial T(x, t)}{\partial x} \right|_{x=0} = \frac{\rho}{k} VL_{ev}$$

and at  $x = \infty$

$$T(\infty, t) = 0.$$

where  $L_{ev}$  is the latent heat of evaporation.

Laplace transformation of Eq. (2.20) with respect to time allows the resultant second-order differential equation to be solved in the transformed plane. The mathematical derivation of the closed-form solution can be found in Ref. [10]. The resulting closed-form solution is

$$T(x, t) = \frac{I_o \delta \sqrt{\alpha}}{2\rho Cp(\alpha \delta - V)} \left( \begin{aligned} & 4ierfc\left(\frac{x}{2\sqrt{\alpha t}} + b\sqrt{t}\right) + \frac{3b^2 + c^2}{2b(b^2 - c^2)} erfc\left(\frac{x}{2\sqrt{\alpha t}} + b\sqrt{t}\right) \\ & + \frac{1}{2b} \exp\left(-\frac{2bx}{\alpha}\right) erfc\left(\frac{x}{2\sqrt{\alpha t}} - b\sqrt{t}\right) \\ & + \frac{1}{(b-c)} \exp[-[\delta x + (b^2 - c^2)]t] erfc\left[-\left(\frac{x}{2\sqrt{\alpha t}} + c\sqrt{t}\right)\right] \\ & + \frac{1}{(b+c)} \exp\left[\frac{x}{\sqrt{\alpha}}(b+c) + (b^2 - c^2)t\right] erfc\left[\left(\frac{x}{2\sqrt{\alpha t}} - c\sqrt{t}\right)\right] \\ & - \frac{2}{(b-c)} \exp(-\delta x) \end{aligned} \right) \\ - \frac{\rho VL_{ev}}{4bk} \left( \begin{aligned} & 4b\sqrt{\alpha t} erfc\left(\frac{x}{2\sqrt{\alpha t}} + b\sqrt{t}\right) \\ & - \sqrt{\left(\frac{x}{2\sqrt{\alpha t}} + b\sqrt{t}\right)} + \sqrt{\alpha} \exp\left(\frac{2bx}{\alpha}\right) erfc\left(\frac{x}{2\sqrt{\alpha t}} - b\sqrt{t}\right) \end{aligned} \right) \quad (2.22)$$

where  $b = \frac{V}{2\sqrt{\alpha}}$  and  $c = b - \delta\sqrt{\alpha}$ .

The quasi-steady solution for the temperature [Eq. (2.22)] can be obtained by an iterative procedure, i.e., setting the velocity and calculating the temperature, later correcting the velocity by inserting the temperature calculated in the velocity equation [Eq. (2.21)], and then repeating this procedure until Eqs. (2.21) and

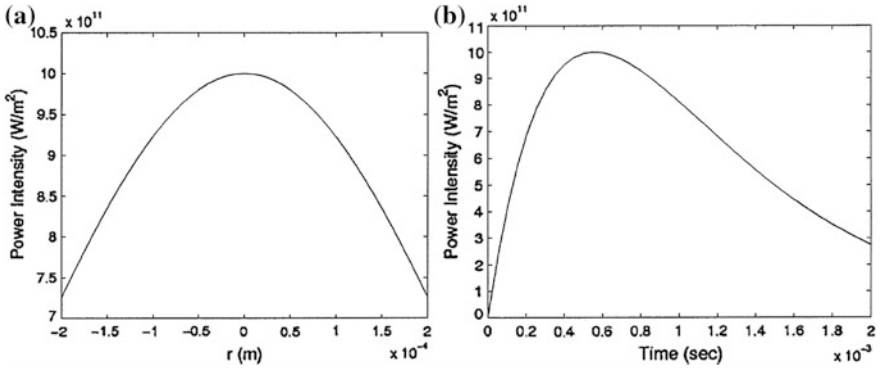


Fig. 2.6 a Spatial variation, and b temporal variation in the laser power intensity distribution [9]

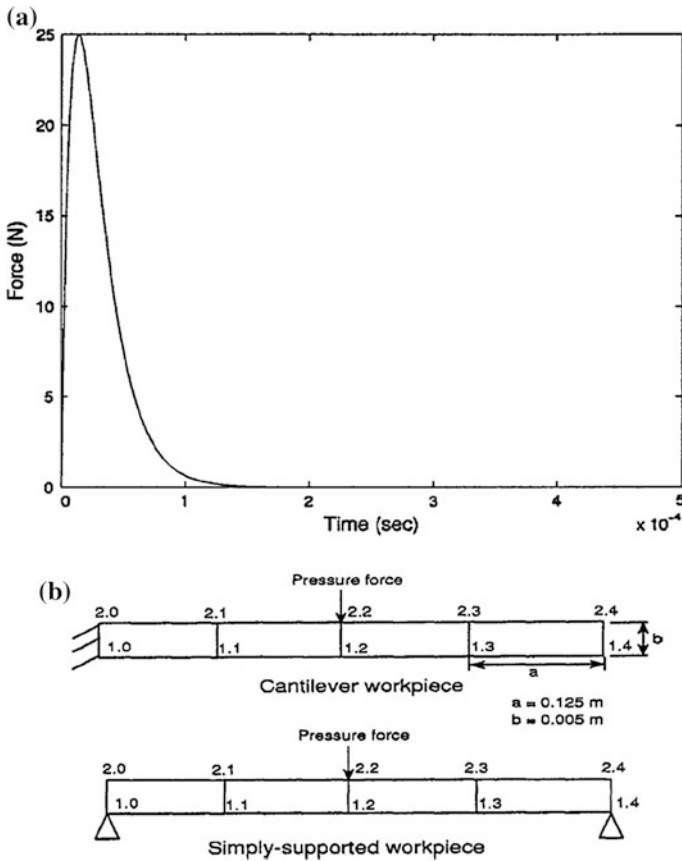


Fig. 2.7 a Force input applied to the workpiece, and b layout of the workpiece [9]

(2.22) are satisfied. Figure 2.6a, b shows the spatial and temporal variation in the laser power intensity distribution.

The recoil pressure can be calculated after considering the rate of momentum change across the receding surface [4]. The rate of momentum at the irradiated surface owing to the receding surface, as shown in Fig. 2.7a, is

$$AP_r = \dot{m}V_{ev}$$

where A is the area of the irradiated surface,  $P_r$  is the recoil pressure,  $\dot{m}$  is the rate of mass flow and  $V_{ev}$  is the evaporating front velocity, which can be formulated from Maxwell's law for the velocity distribution of molecules [11], i.e.,

$$V_{ev} = \sqrt{\frac{k_B T_s}{2\pi m}} \exp\left(-\frac{mL_{ev}(T)}{k_B T_s}\right)$$

where m is the mass of an atom,  $T_s$  is the surface temperature and  $k_B$  is the Boltzmann's constant.

The recoil pressure can be written as

$$P_r = \frac{\dot{m}}{A} V_{ev} \quad (2.23)$$

The energy dissipated by evaporation is the sum of the latent heat of evaporation and the kinetic energy of the evaporated molecules, i.e.

$$I_{ev} = \frac{\dot{m}\left(\frac{1}{2}V_{ev}^2 + L_{ev}\right)}{A}$$

Substitution of  $\dot{m}/A$  in the above equation yields

$$I_{ev} = \frac{P_r}{V_{ev}} \left(\frac{1}{2}V_{ev}^2 + L_{ev}\right)$$

Therefore, the recoil pressure can be written as

$$P_r = \frac{I_{ev}L_{ev}}{\left(\frac{1}{2}V_{ev}^2 + L_{ev}\right)} \quad (2.24)$$

The recoil pressure is computed from Eq. (2.24). The laser power intensity dissipated by evaporation is

$$I_{ev} \cong I_0 - \dot{q}_{solid}$$

where  $\dot{q}_{solid}$  is the energy dissipated in the solid phase. It should be noted that the energy dissipated by melting is considerably smaller than the energy dissipated during evaporation and can be neglected.

The pressure force acting normal to the substrate surface can be written as

$$F_o = \int_0^{r_e} 2\pi r_e P dr \quad (2.25)$$

where  $r_e$  is the radius of the evaporated surface ( $r_e = 0.4$  mm). The variation in normal pressure force with time is assumed to be exponential, i.e.,

$$F(t) = F_o(\exp(-\beta t) - \exp(-\gamma t))$$

where  $\beta$  and  $\gamma$  are constants. Figure 2.7a shows the normal pressure force.

### 2.2.2 Flexural Wave Analysis

The finite element method (FEM) is applied as a numerical tool for the analysis of flexural wave behavior for a workpiece as shown in Fig. 2.7b. The rectangular finite elements for the workpieces contain pseudo-internal degrees of freedom (DOF). The size of each element is schematically illustrated in Fig. 2.7b. The internal DOF are for better representation of bending moments generated by the external actuators and are condensed into the physical DOF using the Guyan reduction technique [12].

Hamilton's principle is given by

$$\delta \int_{t_1}^{t_2} (K_i - \Pi) dt = 0$$

where  $\Pi$  is the potential energy while  $K_i$  is the kinetic energy defined as

$$K_i = \frac{1}{2} \int_V \rho \dot{\mathbf{u}}^T \dot{\mathbf{u}} dV \quad (2.26)$$

where  $\dot{\mathbf{u}}$  is velocity vector and  $\mathbf{T}$  is the tensor notation. In Eq. (2.26), the potential energy  $\Pi$  is given by

$$\Pi = - \int_V \mathbf{u}^T \mathbf{P}_b dV - \int_S \mathbf{u}^T \mathbf{P}_s dS - \mathbf{u}^T \mathbf{P}_c$$

where  $\mathbf{P}_b$  is the vector of body forces applied to volume  $V$ ,  $\mathbf{P}_s$  is the vector of surface force and  $\mathbf{P}_c$  is the concentrated load vector.

The following relations are defined for the finite element formulation:

$$\mathbf{u}_e = N_u \mathbf{u}_i$$

where  $N_u$  is the shape function matrix and  $\mathbf{u}_i$  is the vector of nodal displacement. The subscript 'e' in the equations stands for the element. Relating strain to displacement

$$S_e = L_u \mathbf{u}_e = [L_u N_u] \mathbf{u}_i = B_u \mathbf{u}_i$$

where  $S_e$  is the elemental strain and  $L_u$  is the differential operator which is given by

$$L_u = \begin{bmatrix} \frac{\partial}{\partial x} & 0 \\ 0 & \frac{\partial}{\partial y} \\ \frac{\partial}{\partial y} & \frac{\partial}{\partial x} \end{bmatrix} \quad (2.27)$$

Substituting the above equations in (2.26) gives

$$M_{uu} \ddot{\mathbf{u}} + K_{uu} \mathbf{u} = \mathbf{F} \quad (2.28)$$

where  $\ddot{\mathbf{u}}$  is the acceleration vector and the element matrices and vectors are given by

$$M_{uu} = \int_{V_e} \rho N_u^T N_u dV : K_{uu} = \int_{V_e} B_u^T c B_u dV$$

$$\mathbf{F}_e = \int_{V_e} N_u^T \mathbf{P}_b dV + \int_{S_e} N_u^T \mathbf{P}_s dS + N_u^T \mathbf{P}_c$$

For a rectangular element of size  $(2a \times 2b)$  with  $W_s$  as the width, the shape functions are given as

$$N_1 = \frac{1}{4} \left(1 - \frac{x}{a}\right) \left(1 - \frac{y}{b}\right) \quad N_2 = \frac{1}{4} \left(1 + \frac{x}{a}\right) \left(1 - \frac{y}{b}\right)$$

$$N_3 = \frac{1}{4} \left(1 + \frac{x}{a}\right) \left(1 + \frac{y}{b}\right) \quad N_4 = \frac{1}{4} \left(1 - \frac{x}{a}\right) \left(1 + \frac{y}{b}\right) \quad (2.29)$$

Internal DOF are added to the element to give a better representation to the bending moments caused by the piezoelectric effects. Two shape functions are defined for this purpose, which are given as follows:

$$N_5 = \frac{a^2 - x^2}{a^2} \quad N_6 = \frac{b^2 - y^2}{b^2}$$

The shape functions vanish at the element boundaries when  $x = \pm a$  and  $y = \pm b$ . The displacement vector,  $\mathbf{u}_e$ , is now expressed as

$$\mathbf{u}_e = N_u \mathbf{u}_i + X \mathbf{a}_j \quad (2.30)$$

The strain vector,  $\mathbf{S}_e$ , is now written as

$$\mathbf{S}_e = B_u \mathbf{u}_i + Y \mathbf{a}_j \quad (2.31)$$

where  $\mathbf{a}_j$  is the added generalized coordinate vector and X and Y in the above equations are given by

$$X = \begin{bmatrix} 0 & 0 \\ N_5 & N_6 \end{bmatrix} \quad \text{and} \quad Y = L_u X = -2 \begin{bmatrix} 0 & 0 \\ 0 & y \\ x & 0 \end{bmatrix} \quad (2.32)$$

The new matrix,  $K_{uu}^*$  is the global elastic stiffness matrix which is composed of  $[K_{uu}]_e^*$  and given by

$$[K_{uu}]_e^* = [K_{uu}]_e - [K_{ua}]_e [K_{aa}]_e^{-1} [K_{au}]_e \quad (2.33)$$

where  $[K_{ua}]_e$  and  $[K_{aa}]_e$  are partitioned stiffness matrices given by

$$[K_{ua}]_e = \int_V B_u^T c Y dV \quad \text{and} \quad [K_{aa}]_e = \int_V Y_u^T c Y dV \quad (2.34)$$

where C is a constant matrix. Hence the final equation becomes

$$M_{uu} \ddot{\mathbf{u}} + K_{uu} \mathbf{u} = \mathbf{F} \quad (2.35)$$

### 2.2.2.1 Initial and Boundary Conditions

Initially, the displacements are set to zero for the cantilever and simply supported cases. Also, at  $x = 0$ , i.e. at the fixed end, the displacement is always zero, which is given as follows: at  $x = 0$ ,  $\mathbf{u} = 0$ ; for the simply supported case, at  $x = 1$ ,  $\mathbf{u} = 0$ .

### 2.2.2.2 Method of Solution

In the finite element analysis, the workpiece is divided into four elements where the number of divisions is uniform in the x direction and the thickness is considered to be uniform. The elemental stiffness and mass matrices are determined, which are then assembled to yield the global matrices.

### 2.2.2.3 State-Space Method

The equation of motion is converted into state-space form and for a deterministic system and is given as

$$\dot{z} = Az + BF \quad (2.36)$$

where  $\dot{z}$  is the velocity vector in the steady space and

$$\mathbf{u} = Cz \quad (2.37)$$

where  $z$  is the complete state vector,  $u$  is the required displacement.  $C$  is a matrix defining the location where displacement is required,  $A$ , and  $B$  are the system and input matrices, respectively, given as

$$A = \begin{bmatrix} 0 & I \\ -M_{uu}^{-1}K_{uu} & -M_{uu}^{-1}C_{uu} \end{bmatrix} \text{ and } B = \begin{bmatrix} 0 \\ -M_{uu}^{-1}F \end{bmatrix} \quad (2.38)$$

where  $C_{uu}$  is the proportional damping introduced through the following equations:

$$C_{uu} = \alpha M_{uu} + \beta K_{uu}$$

$\alpha$  and  $\beta$  being the damping coefficients. Matrix  $C$  in Eq. (2.37) defines the location where displacement is required. These matrices are introduced through Matlab code and simulated for a given force and time interval to obtain the displacement  $u$  at various locations.

### 2.2.2.4 Determination of Stresses

The strain for a given element is given by  $\mathbf{S}_e = B_u \mathbf{u}_e$ , where  $B_u = L_u N_u$  and  $N_u$  is given by

$$N_u = \begin{bmatrix} N_1 & 0 & N_2 & 0 & N_3 & 0 & N_4 & 0 \\ 0 & N_1 & 0 & N_2 & 0 & N_3 & 0 & N_4 \end{bmatrix}$$

The stress is then obtained by using the stress–strain relationship which is given by  $\sigma_e = E\mathbf{S}_e$ . These elemental stresses are properly mapped with respect to global node numbering to obtain the global stress. The global stress  $s$  obtained in this way is given by

$$\sigma = \begin{bmatrix} \sigma_x \\ \sigma_y \\ \tau_{xy} \end{bmatrix} \quad (2.39)$$

Hence, the equivalent stress is given by

$$\sigma_{eq} = \sqrt{\sigma_x^2 + \sigma_y^2} \quad (2.40)$$

### 2.2.3 Results and Discussion

The stress field due to flexural motion of the substrate material is determined by using FEM in the simulations. In order to examine the effect of an additional element, aluminum is introduced as the third element in Fig. 2.7b. It should be noted that no discontinuity of stress and displacement boundaries at the interface between aluminum and steel elements is considered; i.e. the continuity in the stress and displacement fields with change in the mechanical properties of the substrate is taken into account for the aluminum. The displacement and equivalent stress differences due to the additional element are computed. Two different arrangements of the workpiece are taken into account, namely a cantilever arrangement and with both ends simply supported.

Figure 2.8a shows the surface displacement of the workpiece for these two geometric arrangements of the substrate material. Displacement of the surface at the central position of the workpiece (Fig. 2.7b) is higher for the cantilever case than for the case where both ends are freely supported. This is because of the cantilever arrangement, in which case the workpiece moves freely from one end. This, in turn, enhances the amplitude of the surface displacement. Moreover, the amplitude of the surface displacement oscillates in the early period  $t \leq 40,006$  s, increases gradually, reaching its maximum at  $t \approx 0.085$  s, and then decreases; i.e. the temporal behavior of displacement does not show a regular pattern for the cantilever case. In the case of the workpiece with both ends simply supported, the amplitude of displacement damps out as time progresses. This is because of the simply supported system, which forces the displacement to decay with time. A peak amplitude of surface displacement of the order of  $2 \mu\text{m}$  occurs.

Figure 2.8b shows the temporal variation in the displacement difference at different locations (Fig. 2.7b). The displacement difference is obtained by subtracting the displacements corresponding to cases with and without additional aluminum. The displacement corresponding to the additional element is lower than that corresponding to a steel substrate. Moreover, the displacement difference decays with time for the cantilever arrangement and when both ends are simply supported. This indicates that the influence of the additional element on the displacement is significant in the early period, but that the effect decreases with time.

Figure 2.9a shows the temporal variation in the equivalent stress at four locations on the workpiece, as shown in Fig. 2.7b, for a cantilever arrangement. The equivalent stress level attains high values in the early period and decreases to zero before reaching its second peak. Moreover, as the location moves away from the

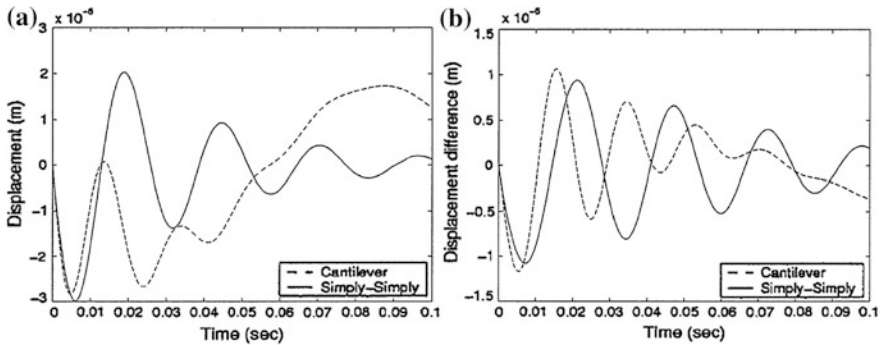


**Fig. 2.8** **a** Displacement of the flexural waves obtained at the center of the beam, and **b** displacement difference in the flexural waves obtained at the centre of the beam (the displacement difference corresponds to the displacement difference due to an additional element and no additional element) [9]

fixed end (locations 1.3 and 1.4), the magnitude of the equivalent stress decreases. This is because of the flexural motion of the workpiece, i.e. the stress levels drop as the displacement decreases. The zero equivalent stress indicates zero stress components. Zero stress components occur when the displacement decreases to zero, i.e. when the workpiece straightens. This corresponds to 0.0057 s for both Figs. 2.8a and 2.9a. The maximum equivalent stress is of the order of  $10^4$  Pa, which is considerably less than the yield stress of the substrate material (215 MPa).

Figure 2.4b shows the equivalent stress difference at different locations in the workpiece for the cantilever arrangement. The equivalent stress difference is obtained from the equivalent stress corresponding to steel and that corresponding to steel with additional aluminum. The equivalent stress attains high values at location 1.1 in the workpiece (Fig. 2.7b). This occurs because location 1.1 is close to the fixed end of the workpiece. The equivalent stress difference oscillates and damps out with time. The frequency of the oscillation appears to be regular; i.e., at all locations the stress level oscillates with almost the same frequency. Moreover, the stress level oscillations are out of phase at locations 1.2 and 1.3. Consequently, the additional element in the workpiece modifies the equivalent stress levels, in which case the magnitude of the stress levels decreases.

The bending of the workpiece during flexural motion results in shear stress development in the substrate material. This is shown in Fig. 2.10 at different locations (Fig. 2.7b). The magnitude of shear stress is almost twice the equivalent stress. The level of shear stress is negative in the region close to the fixed end. As the location moves towards the free end, the shear stress becomes positive. Moreover, the stress level oscillates with time. The level of the shear stress decreases to zero at 0.057 s, at which the displacement is also zero. The stress level decreases with time at a location close to the free end. The temporal behavior of the shear stress at locations 1.2 and 1.3 (Fig. 2.7b) is almost identical with opposite signs.

**Fig. 2.9** **a** Equivalent stress distribution, and **b** equivalent stress difference for a cantilever beam. Curves correspond to nodal points shown in Fig. 2.7b [9]

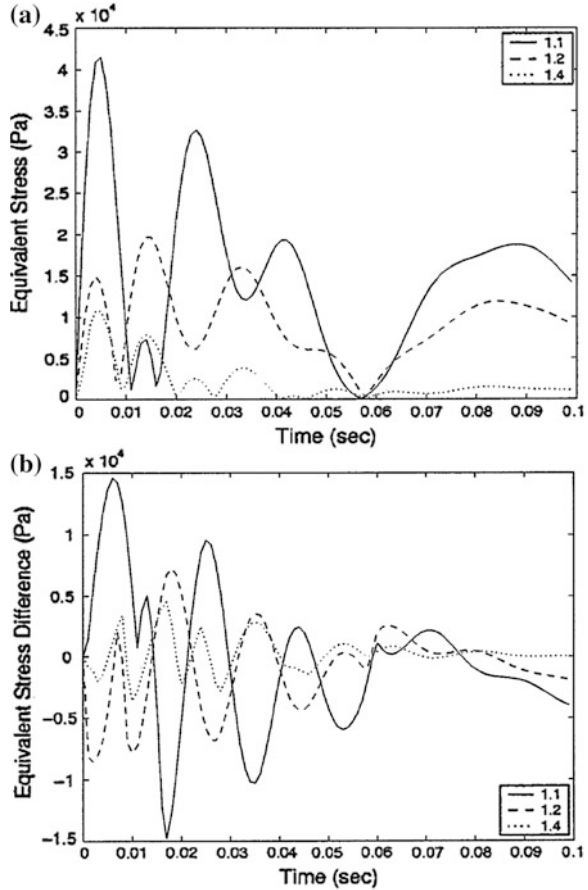
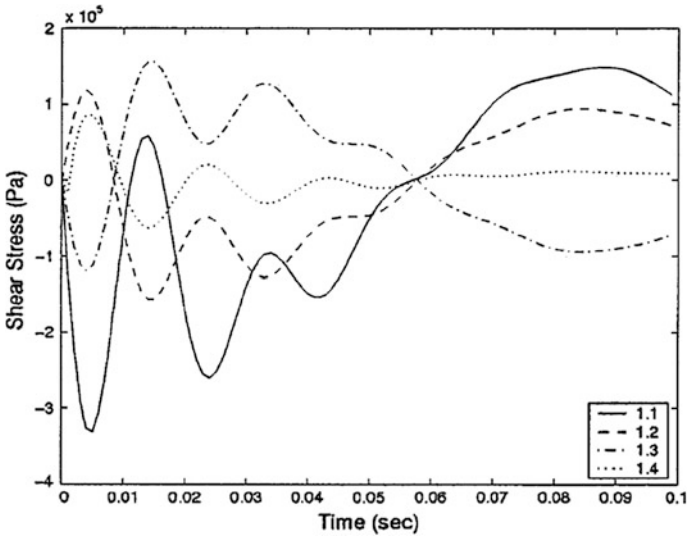


Figure 2.11a shows the temporal variation in the equivalent stress at different locations in the workpiece (Fig. 2.7b) for the case where both ends are simply supported. The equivalent stress decreases as time increases. This is because of the dying of the flexural motion of the workpiece. The equivalent stress decreases to zero at points where the displacement is zero. The equivalent stress decreases in the region close to the center of the workpiece (location 1.3). This occurs because of surface displacement in this region, which is small. Consequently, a small displacement gives low stress components, which, in turn, results in a low equivalent stress in this region.

Figure 2.11b shows the equivalent stress difference at different locations in the workpiece for the case where both ends are simply supported. The equivalent stress difference decreases with time for all locations. In general, the additional element reduces the equivalent stress levels, since the magnitude of the equivalent stress difference is positive. Moreover, the stress level difference is almost steady at points 1.1, 1.2 and 1.3 during the period  $0.01 \leq t \leq 0.07$  s. This indicates that



**Fig. 2.10** Shear stress distribution for a cantilever beam. Curves correspond to nodal points in Fig. 2.7b [9]

the temporal response of the workpiece is almost the same for these points during this period, provided that the equivalent stress corresponding to steel with additional aluminum results in lower equivalent stress levels. The frequency of oscillation of the stress difference is almost the same for each location. This indicates that flexural motions of the workpiece with and without additional aluminum are the same, but their amplitude varies, which, in turn, results in different stress levels at each point in the workpiece.

Figure 2.12 shows the temporal variation in shear stress at four locations in the workpiece (Fig. 2.7b) for the case with both ends simply supported. The magnitude of shear stress decreases with time. This is because of the temporal behavior of the displacement, which decreases with time. Moreover, opposite behavior in shear stress is observed for two consecutive points from the free supported end. The stress level decreases to low values at the center of the workpiece, which cannot be observed in Fig. 2.12. The opposite stress behavior at points 1.1 and 1.2 is due to flexural motion of the workpiece. The stress level is higher in the early heating period owing to the high amplitude of displacement in this period.

### 2.3 Laser Pulse Heating of Steel Surface

In the analysis of the flexural characteristics of the laser pulse heating of steel surface, the formulation and findings of the previous study [13] are considered.

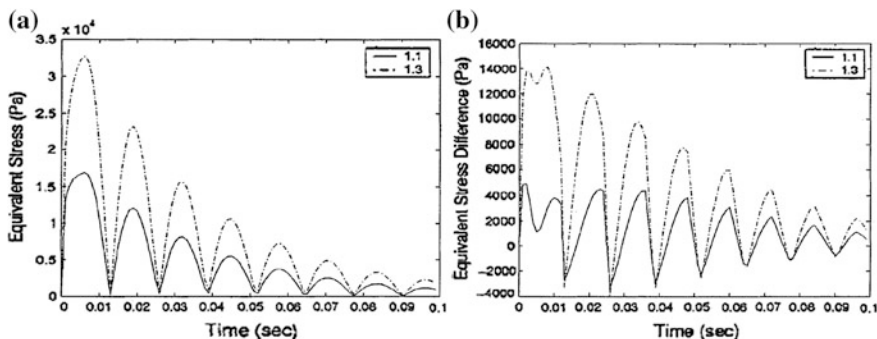


Fig. 2.11 a Equivalent stress distribution, and b equivalent stress difference for a simply supported beam. Curves correspond to nodal points shown in Fig. 2.7b [9]

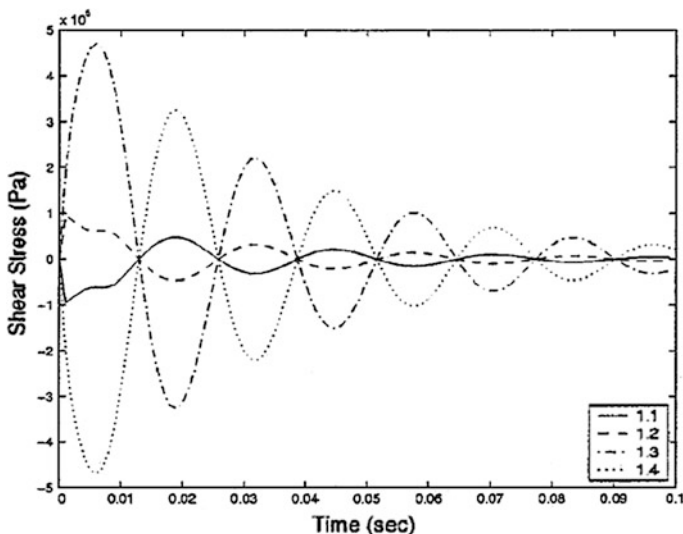


Fig. 2.12 Shear stress distribution for a simply supported beam. Curves correspond to nodal points shown in Fig. 2.7b [9]

Consider the flexural wave propagation in the substrate during the laser heating process. In this case, the thermal stresses developed in the substrate are predicted first and the wave generated due to axial stress component in the surface vicinity of the substrate is analyzed using a spectral finite element method. Since the workpiece has a certain length, the reflecting waves from the free supported ends of the workpiece are also considered in the analysis.

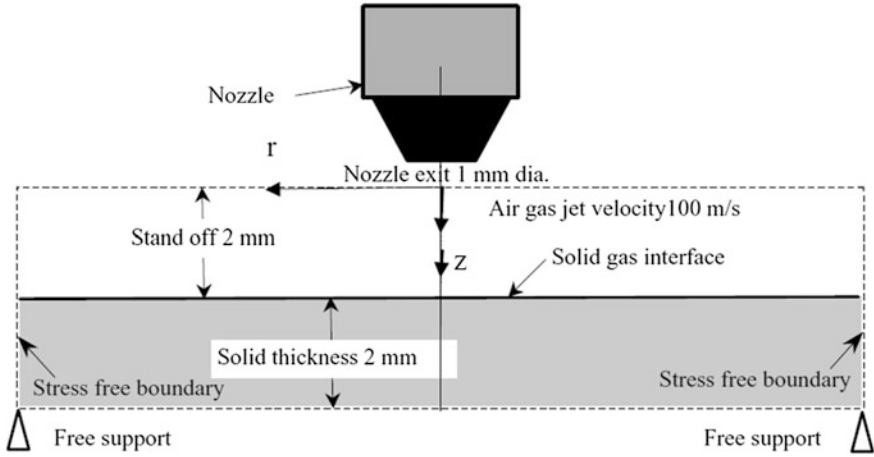


Fig. 2.13 A view of impinging gas and laser workpiece arrangement [13]

### 2.3.1 The Mathematical Model

The gas-assisted laser pulse heating process is considered when modelling the laser workpiece interaction provided that conduction limited heating case is taken into account in the present study [14]. Figure 2.13 shows the schematic view of the heating process.

#### 2.3.1.1 Flow and Heat Conduction Equations

The unsteady flow equations need to be solved to obtain the flow field due to axisymmetric gas jet impingement. The continuity and momentum equations are

$$\frac{\partial \rho}{\partial t} + \frac{\partial}{\partial x_i} (\rho U_i) = 0 \tag{2.41}$$

and

$$\frac{\partial}{\partial t} (\rho U_j) + \frac{\partial}{\partial x_i} (\rho U_i U_j) = \frac{\partial p}{\partial x_j} + \frac{\partial}{\partial x_i} \left[ (\mu_t + \mu) \frac{\partial U_j}{\partial x_i} \right], \tag{2.42}$$

where  $\mu_t$  is the eddy viscosity which has to be specified by a turbulence model. In the present study, low Reynolds number k-ε turbulence model is introduced to account for the turbulence effect of the impinging gas, which is air [14].

The partial differential equation governing the transport of thermal energy has the form

$$\frac{\partial T}{\partial t} + \frac{\partial}{\partial x_i}(U_i T) = \frac{\partial}{\partial x_i} \left[ \left( \frac{\mu_t}{Pr_t} + \frac{\mu}{Pr} \right) \frac{\partial T}{\partial x_i} \right]. \quad (2.43)$$

### 2.3.1.2 Boundary Conditions for Flow Equations

Laminar boundary conditions are set for the mean-flow variables, and the boundary conditions  $k = 0$  and  $d\varepsilon/dz = 0$  are applied at the wall. The low-Reynolds number extension does not employ wall functions; therefore, the grid employed normal to the main flow direction needs to be distributed so as to give a high concentration of grid cells near the wall, with the wall-adjacent node positioned at  $z^+ = \rho z u^*/\mu \leq 1.0$ .

Inlet to control volume:

$$U_i = \text{specified and } T = \text{constant}. \quad (2.44)$$

The kinetic energy of turbulence is estimated according to some fraction of the square of the average inlet velocity [15]

$$k = \lambda \bar{u}^2, \quad (2.45)$$

where  $\bar{u}$  is the average inlet velocity and  $\lambda$  is a fraction.

The dissipation is calculated according to the equation [16]

$$\varepsilon = C_\mu \frac{k^{3/2}}{bd} \quad (2.46)$$

where  $d$  is the inlet diameter. The values  $\lambda = 0.03$  and  $b = 0.005$  are commonly used and may vary slightly in the literature [15].

Outlet to control volume:

It is assumed that the flow extends over a sufficiently long domain; therefore, it is fully developed at the exit section. Thus, for any variable  $\phi$  the condition is

$$\frac{\partial(r\phi)}{\partial x} = 0 \quad (2.47)$$

where  $x$  is the arbitrary outlet direction.

Symmetry axis:

The radial derivative of the variables is set to zero at the symmetry axis, i.e.,

$$\frac{\partial\phi}{\partial r} = 0 \quad \text{and} \quad V = 0 \quad (2.48)$$

Solid fluid interface:

The temperature at the solid–gas interface is considered as the same, i.e.,

$$T_{w_{solid}} = T_{w_{gas}} \quad \text{and} \quad K_{solid} \frac{\partial T_{w_{solid}}}{\partial z} = K_{gas} \frac{\partial T_{w_{gas}}}{\partial z}.$$

The unsteady heat conduction equation:

$$\frac{\partial}{\partial t} (C_p \rho T) = \frac{\partial}{\partial x_i} \left[ K \frac{\partial T}{\partial x_i} \right] + S, \quad (2.49)$$

where  $S$  is the unsteady spatially varying laser output power intensity distribution and is considered as Gaussian with  $1/e^2$  points equal to 0.375 mm, from the center of the beam. Therefore,  $S$  is stated as follows:

$$S = \frac{I_0}{\sqrt{2\pi}a} \exp\left(-\frac{r^2}{a^2}\right) \delta \exp(-\delta z) f(t), \quad (2.50)$$

where  $\frac{I_0}{\sqrt{2\pi}a} \exp\left(-\frac{r^2}{a^2}\right)$  is the intensity distribution across the surface,  $\exp(-\delta z)$  is the absorption function, and  $f(t)$  is the function accommodating the time variation of the pulse shape. The pulse properties are given in Table 2.3.

Boundary conditions for the heat conduction equation:

Convection with a constant coefficient for still air is considered at the  $z = z_{\max}$  boundary for the plate. The continuity of temperature between the solid and the gas is enforced at the interface; and a constant temperature,  $T = T_{\text{amb}}$ , is assumed for the distance far away from the laser source.

### 2.3.1.3 Variable Properties

An equation of state is used for the impinging gas and the specific heat capacity and thermal conductivity for both air and steel were considered only as a function of temperature. The temperature dependence of properties is given in [17].

### 2.3.1.4 Calculation of the Flow Field Variables

The control volume approach is used when solving the governing equations of flow and heat transfer numerically. The differential equation is integrated over the control volume to yield the discretization equation. The main reasons for choosing the control-volume formulation for flow field are its simplicity and easy physical interpretation [18]. The discretization process is not given here due to lengthy arguments, but refer to [19].

**Table 2.3** Pulse properties used in the simulation

Rise time (ms)	Fall time (ms)	Total pulse length (ms)	Peak power intensity (W/m <sup>2</sup> )
0.2	1.08	1.48	10 <sup>9</sup>

The grid used in the present calculations has  $38 \times 70$  mesh points, provided that the grid independent test is satisfied. The details of the grid orientation and grid independent test results are given in [20].

The two problems of determining the pressure and satisfying continuity are overcome by adjusting the pressure field so as to satisfy continuity. This arrangement gives a convenient way of handling the pressure linkages through the continuity equation and is known as the Semi-Implicit Method for Pressure-Linked Equations (SIMPLE) algorithm. The details of this algorithm are found in [21].

The governing equation for heat conduction in solid [Eq. (2.49)] can be written in the form of flow equations. Thus, the discretization procedure leads to algebraic equations of the form similar to flow equations with temperature  $T$  replacing the general variable.

### 2.3.1.5 Thermal Stress Modelling

The temperature field results in the thermal stresses being generated in the substrate, which can lead to the elastic–plastic displacement in the substrate material. The stress is related to strains by

$$\{\sigma\} = [D]\{\varepsilon^e\}, \quad (2.51)$$

where  $\{\sigma\}$  is the stress vector, and  $[D]$  is the elasticity matrix.

$$\{\varepsilon^e\} = \{\varepsilon\} - \{\varepsilon^{th}\}$$

where  $\{\varepsilon\}$  is the total strain vector and  $\{\varepsilon^{th}\}$  is the thermal strain vector.

Equation (2.51) may also be written as

$$\{\varepsilon\} = [D]^{-1}\{\sigma\} + \{\varepsilon^{th}\} \quad (2.52)$$

Since the present case is axially symmetric, and the material is assumed to be isotropic, the above stress–strain relations can be written in cylindrical coordinates as

$$\begin{aligned} \varepsilon_{rr} &= \frac{1}{E}[\sigma_{rr} - \nu(\sigma_{\theta\theta} + \sigma_{zz})] + \alpha\Delta T(r, z, t) \\ \varepsilon_{\theta\theta} &= \frac{1}{E}[\sigma_{\theta\theta} - \nu(\sigma_{rr} + \sigma_{zz})] + \alpha\Delta T(r, z, t) \\ \varepsilon_{zz} &= \frac{1}{E}[\sigma_{zz} - \nu(\sigma_{rr} + \sigma_{\theta\theta})] + \alpha\Delta T(r, z, t) \\ \varepsilon_{rz} &= \frac{1}{G}\sigma_{rz} \end{aligned} \quad (2.53)$$

where  $E$ ,  $\nu$ , and  $\alpha$  are the modulus of elasticity, Poisson's ratio, and coefficient of thermal expansion, respectively.  $\Delta T(r, z, t)$  represents the temperature rise at a point  $(r, z)$  at time  $t$  with respect to that at  $t = 0$  corresponding to a stress-free condition. A typical component of thermal strain from Eq. (2.53) is

$$\begin{aligned}\varepsilon^{th} &= \alpha \Delta T(r, z, t) \\ &= \alpha(T(r, z, t) - T_{ref})\end{aligned}\quad (2.54)$$

where  $T_{ref}$  is the reference temperature at  $t = 0$ .

When  $\alpha$  a function of temperature then Eq. (2.54) becomes

$$\varepsilon^{th} = \int_{T_{ref}}^T \alpha(T) dT \quad (2.55)$$

The present study uses a mean or weighted-average value of  $\alpha$ , such that

$$\varepsilon^{th} = \bar{\alpha}(T)(T - T_{ref}), \quad (2.56)$$

where  $\bar{\alpha}(T)$  is the mean value of coefficient of thermal expansion and is given by

$$\bar{\alpha}(T) = \frac{\int_{T_{ref}}^T \alpha(T) dT}{T(r, z, t) - T_{ref}} \quad (2.57)$$

To develop a finite element procedure for stress computation, the standard displacement-based finite element method is used. The basis of this approach is the principle of virtual work, which states that the equilibrium of any body under loading requires that for any compatible small virtual displacements (which are zero at the boundary points and surfaces and correspond to the components of displacements that are prescribed at those points and surfaces) imposed on the body in its state of equilibrium, the total internal virtual work or strain energy ( $\delta U$ ) is equal to the total external work due to the applied thermally induced loads ( $\delta U$ ), i.e.,  $\delta U = \delta V$ . For the static analysis of problems having linear geometry and thermoelastic material behavior, one can derive the following equation using standard procedure [22].

$$\begin{aligned}& \int_{\forall} (\{\delta \varepsilon\}^T [D] \{\varepsilon\} - \{\delta \varepsilon\}^T [D] \{\varepsilon^{th}\}) dV \\ &= \int_{\forall} \{\delta U\}^T \{f^B\} dV + \int \{\delta U_s\}^T \{P\} d\Omega + \sum \{\delta \bar{U}\}^T \{\bar{F}\}\end{aligned}\quad (2.58)$$

where  $\{f^B\}$  is the applied body force,  $\{P\}$  the applied pressure vector,  $\{\bar{F}\}$  the concentrated nodal forces to the element,  $\{\delta U\}$  the virtual displacement,  $\{\delta U_s\}$  the virtual displacement on the boundary where pressure is prescribed, and  $\{\delta \bar{U}\}$  the virtual displacement of boundary nodes where concentrated load is prescribed.

The strains may be related to the nodal displacement by

$$\{\varepsilon\} = [B]\{\bar{U}\} \quad (2.59)$$

where  $[B]$  is the strain displacement gradient matrix, and  $\{\bar{U}\}$  the nodal displacement vector.

The displacements within the elements are related to the nodal displacement by

$$\{U\} = [N]\{\bar{U}\} \quad (2.60)$$

where  $[N]$  is the matrix of shape (or interpolation) functions.

Equation (2.58) can be reduced to the following matrix form:

$$[K_e]\{\bar{U}\} - \{F^{th}\} = \{F\}^b + \{F\}^s + \{\bar{F}\} \quad (2.61)$$

where  $[K_e] = \int_V [B]^T [D] [B] dV$  is the element stiffness matrix,  $\{F^{th}\} = \int_V [B]^T [D] [\varepsilon^{th}] dV$  the element thermal load vector,  $\{F\}^b = \int_V [N]^T [f^B] dV$  the element body force vector,  $\{F\}^s = \int_V [N_n]^T [P] dV$  the element pressure vector, and  $[N_n] =$  matrix of shape functions for normal displacement at the boundary surface.

Assembly of element matrices and vectors of Eq. (2.61) yields

$$[K]\{\bar{d}\} = \{\bar{R}\},$$

where  $[K]$ ,  $\{\bar{d}\}$  and  $\{\bar{R}\}$  are the global stiffness matrix, global nodal displacement vector, and global nodal load vector, respectively. Solution of the above set of simultaneous algebraic equations gives unknown nodal displacements and reaction forces.

### 2.3.2 Wave Analysis

In the analysis, the workpiece is divided into a number of elements and each element can be treated as uniform. The displacement vector is then transformed from time domain into frequency domain using fast Fourier transformation (FFT). The transform response is fed back into the governing differential equations as solved at each frequency component using finite element method (FEM) and the transient response is recovered by using the inverse FFT. Flexural wave analysis is given above in Eqs. (2.9)–(2.19).

### 2.3.3 Results and Discussions

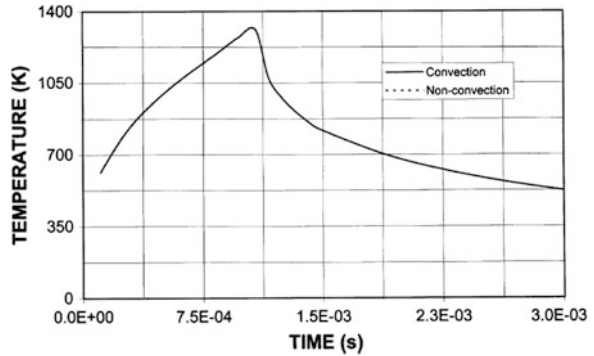
In order to investigate the wave propagation along the transverse direction in the workpiece, six locations with three located at each side from the center of the workpiece along the transverse direction are considered. This is necessary, since the workpiece material disperses the travelling waves in amplitude and frequency domain. The wave reflections from both ends of the workpiece also modify the travelling wave properties. Consequently, to analyze the influence of reflected waves emanating from the ends of the workpiece, a case in which one end of the workpiece is located at infinity is considered. This provides no reflection of the wave from one end of the workpiece.

Figure 2.14 shows the temporal variation of the surface temperature at the center of the heated spot (at  $r = 0$ ) for convective and nonconvective boundary conditions at the surface. The temperature rises rapidly in the early heating period and the rate of rise of surface temperature reduces as the heating progresses. In the cooling cycle, the decay rate of the surface temperature is faster in the beginning of the cooling cycle and the decay rate slows as the cooling period progresses. Consequently, the material response to the heating pulse changes in the cooling cycle as compared to that in the heating cycle. This is because once the laser source disappears, the rate of energy diffused from the surface vicinity of the substrate to the bulk through the conduction becomes large immediately after the laser pulse ends, i.e., the large temperature gradient attainment in the surface region during the heating cycle accelerates the conduction cooling of the surface vicinity. In the case of the long cooling period, the temperature gradient in the surface vicinity is low and the energy diffusion from the surface vicinity to the bulk of the substrate slows down. When comparing temperature profiles with and without convective boundary condition at the surface, it is evident that both temperature profiles are identical. This indicates that convective cooling of the surface is negligibly smaller than the energy input to the substrate material due to the absorption of a laser beam as consistent with the previous work [20].

Figure 2.15a shows the temporal variation of the normal (axial) component of the thermal stress while Fig. 2.15b shows the temporal variation of the equivalent strain in the surface vicinity. The equivalent strain increases as the heating progresses provided that the increase in strain is continuous even in the cooling cycle. It reduces rapidly as the cooling period progresses further. This is because the elastic response of the material is not as fast as the temperature field, i.e. the expansion is continuous for a while after the laser source vanishes. The normal component of the stress varies considerably with time. It results in two maxima; one in the heating cycle and the other in the cooling cycle. The normal component of the stress in the surface vicinity is tensile and it reaches as high as 20 MPa; which is less than the yield stress of the workpiece material.

Figure 2.16a shows the load variation with time while Fig. 2.16b shows the power spectrum density curve. The temporal variation of the load is similar to the normal stress component as shown in Fig. 2.15a, i.e. the value of the stress

**Fig. 2.14** Temporal variation of surface temperature at the center of the irradiated spot with and without convective boundary condition at the surface [13]



component is multiplied by the size of the irradiated spot to obtain the load. Since the total power in a signal is constant, the low and high frequency limits of the signal are determined from Fig. 2.16b. In the present case, Nyquist frequency ( $f_c = \frac{1}{2} \Delta t$ ; where  $\Delta t$  is the sampling rate) is selected as 2,000. It should be noted that  $f_c$  is the maximum frequency contained in the signal.

Figure 2.17 shows the flexural wave amplitude variation with time at four equally spaced locations at the workpiece surface. The first location is 12:5 cm away from the center of the heated spot and following locations are 12:5 cm away from the first location, respectively. The wave amplitude varies with time and no dominant pattern is observed in the wave. This is because the initial wave form at the center of the workpiece is modified as it travels along the workpiece due to: (i) the dispersion effect of the workpiece material, (ii) overlapping of wave modes, and (iii) the reflected waves from the free ends of the workpiece that interfere with the travelling wave. The group speed of the first wave mode is about 3,125 m/s; therefore, the reflection from the free ends takes about  $0.16 \times 10^{-3}$  s to reach the center of the workpiece. Consequently, the reflected wave modifies the travelling wave in the time and amplitude domain. As the location from the first point changes to the following point along the surface, the amplitude of the wave decreases and the travelling wave pattern changes. This indicates that the travelling wave vanishes as it travels towards the free ends of the workpiece, i.e. in the present study, damping coefficient of the workpiece material is taken as 0.025. Moreover, at locations close to the free ends of the workpiece, the wave appears as in high frequency mode. This is because the travelling wave has a low amplitude in these locations and reflected waves modify easily the travelling wave pattern.

## 2.4 Laser Pulse Heat Treatment of Metallic Surfaces

In the analysis of the flexural characteristics of the laser pulse heat treatment of metallic surfaces, the formulation and findings of the previous study [23] are considered. In this section laser induced flexural wave propagation due to recoil pressure generated at vapor-liquid interface of the evaporated surface is

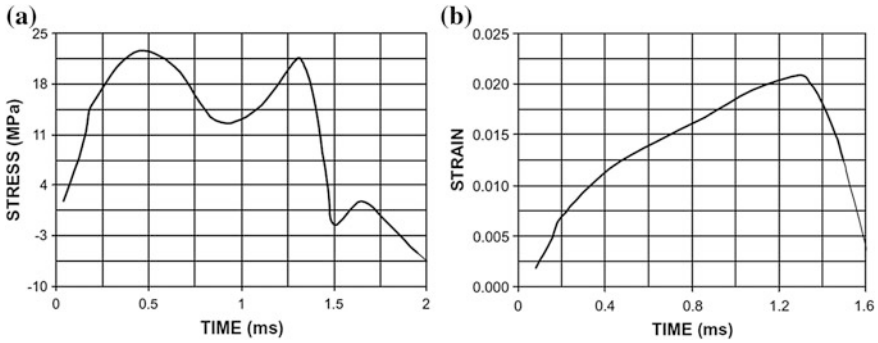


**Fig. 2.15** **a** Temporal variation of load generated in the surface vicinity of the workpiece due to normal component of the thermal stress, and **b** temporal variation of strain in the surface vicinity of the workpiece [13]

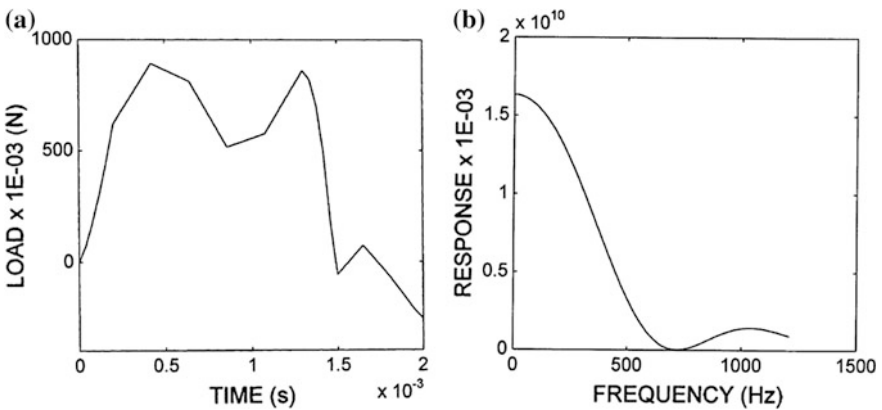


**Fig. 2.16** **a** Temporal variation of load generated due to normal component of the thermal stress, and **b** power spectrum density of thermal load [13]

investigated. The surface temperature rise during a laser heating pulse is presented analytically and recoil pressure is formulated. The flexural wave generation and propagation (due to recoil pressure) are simulated using a finite element method (FEM). The analysis is extended to include three cases of workpiece configurations; namely free-support, cantilever and fix ends.

### 2.4.1 Heat Transfer Analysis

The schematic of the interface is shown in Fig. 2.18. The heat transfer analysis is given above in Eqs. (2.20)–(2.24).

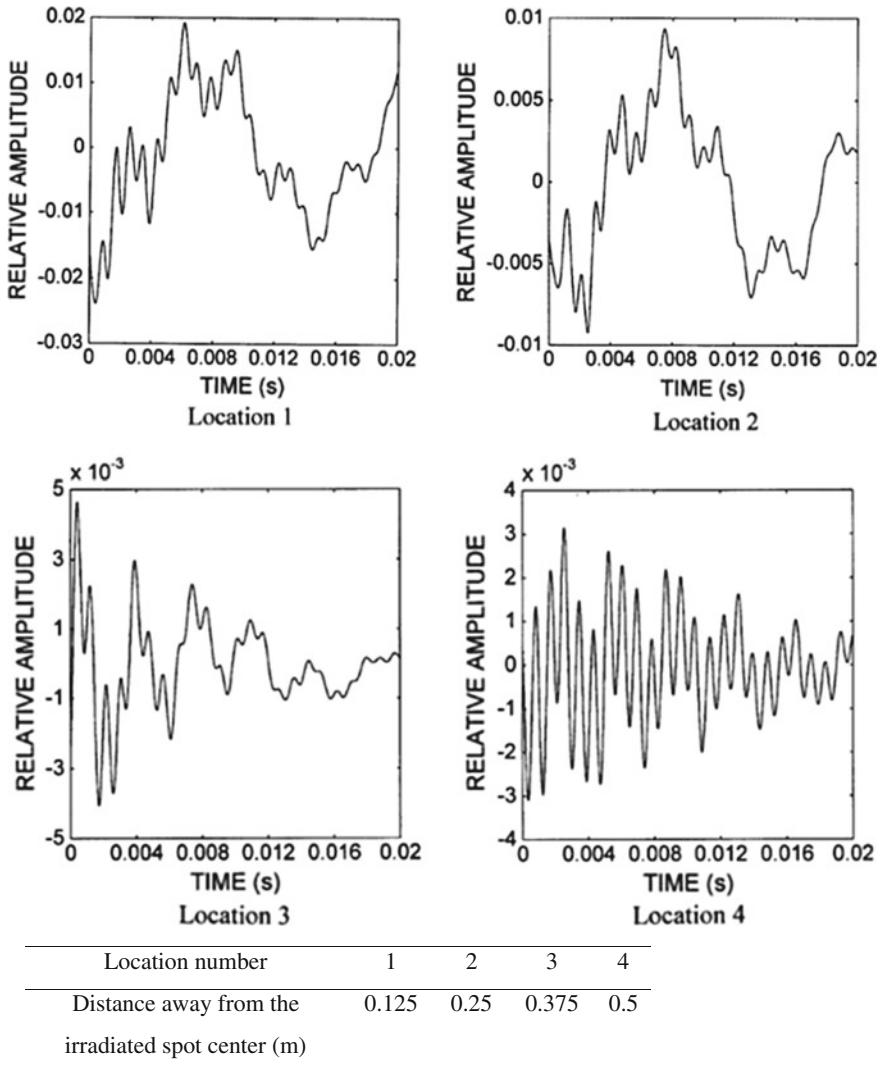


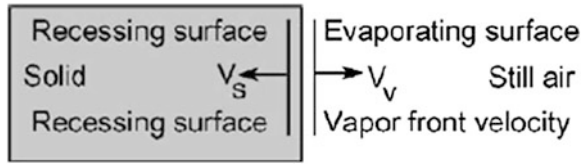
Fig. 2.17 The wave generated at different locations of the workpiece [13]

The pressure predicted is given in the previous study [6]:

$$P_v = 1.82 \times 10^{-3} \frac{\sqrt{C_p T_s I_0}}{[C_p(T_s - T_0) + L_v]} \tag{2.62}$$

The unit in Eq. (2.62) is bar.

**Fig. 2.18** Schematic view of interface [23]



### 2.4.2 Wave Analysis

In wave analysis, the workpiece is divided into a number of elements and each element can be treated as uniform (Fig. 2.19). The displacement vector is then transformed from time domain into frequency domain using fast Fourier transformation (FFT). The transform response is fed back into the governing differential equations as solved at each frequency component using FEM and the transient response is recovered by using the inverse FFT. The cross-sectional area and second moment of area at the mid of each element can be considered as constant over the entire element. Flexural wave analysis is given above in Eqs. (2.9)–(2.19).

### 2.4.3 Results and Discussion

In this case laser non-conduction heating of steel is considered. The flexural wave generation and propagation due to recoil pressure are simulated using FEM. The simulation conditions are extended to include free-supported, cantilever and fixed end workpieces. The material properties employed in the simulations are given in Table 2.4.

Figure 2.20 shows the temporal variation of recoil pressure generated during surface ablation. The pressure force calculation is based on the surface temperature predictions. Moreover, the peak values of the pressure force predicted from the present study and obtained from the previous study is in a good agreement, i.e. the difference is acceptably small which is in the order of 5 %. Moreover, the pressure force variation with time is assumed to be in exponential form.

Figure 2.21 shows the amplitude of displacement at the center of the workpiece with time for different workpiece configurations. In all workpiece configurations, displacement is negative in the early period and it becomes positive as time increases. This indicates the oscillation of the workpiece with a small amplitude. Moreover, the amplitude of the oscillation is lower for both ends fixed workpiece as compared to those corresponding to other workpiece configurations, provided that the amplitude of oscillation is maximum for the cantilever workpiece. Consequently, flexural motion of the workpiece due to a pressure force is damped for both ends fixed workpieces. The amplitude of oscillation as high as 15 mm occurs for both ends simple supported workpiece during the early oscillation period. As the time progresses, oscillation damps at the workpiece surface, except cantilever workpiece as shown in Fig. 2.22. The amplitude and frequency of oscillation is

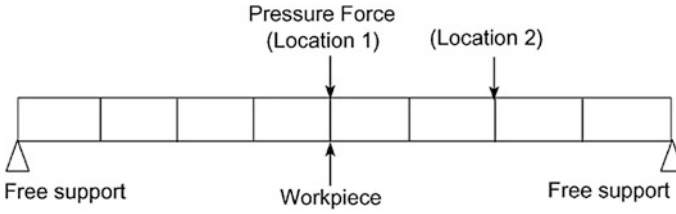


**Fig. 2.19** Schematic view of workpiece and elements used in the analysis [23]

**Table 2.4** Properties of steel and number elements used in simulations

E (GPa)	G (GPa)	$\rho$ (kg/ m <sup>3</sup> )	$\kappa$	$\nu$	$\eta$	Length (m)	Width (m)	Thickness (m)	Number of elements
207	77.6	7,836	0.67	0.3	0.025	1	0.2	0.002	8

affected by the workpiece geometric configuration, i.e. both ends fixed workpiece results in small amplitude and low frequency and oscillation damps in the early period. Moreover, the maximum amplitude of oscillation is in the order of 20 mm for cantilever workpiece arrangement. The free-support arrangement results in the oscillation in the order of 10 mm at the workpiece center.

## 2.5 Laser Ablation: Influence of Force Location

In the analysis of the flexural characteristics of laser ablation process, the formulation and findings of the previous study [24] are considered.

In this section flexural waves generated during laser ablation of the three-layer assembly are considered. The assembly consists of 200  $\mu\text{m}$  Inconel 625 alloy (top layer), 2 mm stainless steel (intermediate layer), and 200  $\mu\text{m}$  Inconel 625 alloy (bottom layer). The assembly resembles the both side Inconel 625 coated stainless steel sheet. The effect of the location of the pressure force on the flexural wave characteristics is examined.

### 2.5.1 Heat Transfer Analysis

A schematic view of laser workpiece interaction due to evaporative heating is shown in Fig. 2.23. The heat transfer analysis is given above in Eqs. (2.20)–(2.24).

The vapor pressure predicted is given in the previous study [6], i.e.:

$$\text{Pr} = 1.82 \times 10^{-3} \frac{\sqrt{C_p T_{ev} I_0}}{C_p (T_{ev} - T_o) + L_{ev}} \quad (2.63)$$

Equation (2.63) is expressed in units of bar.

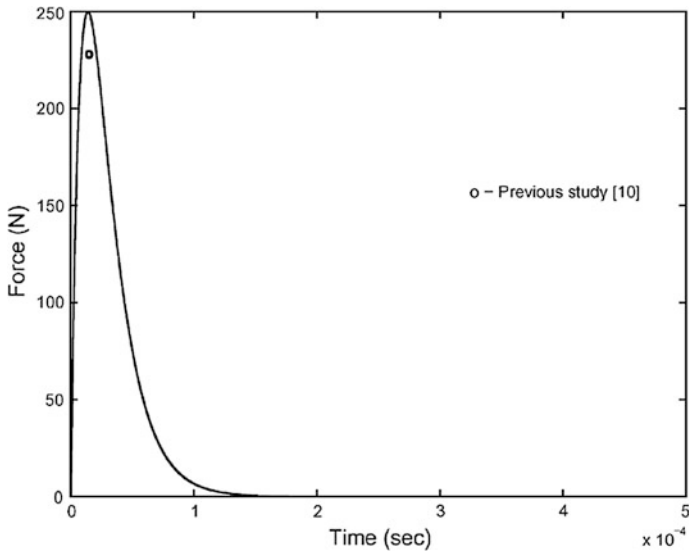


Fig. 2.20 Force response [23]

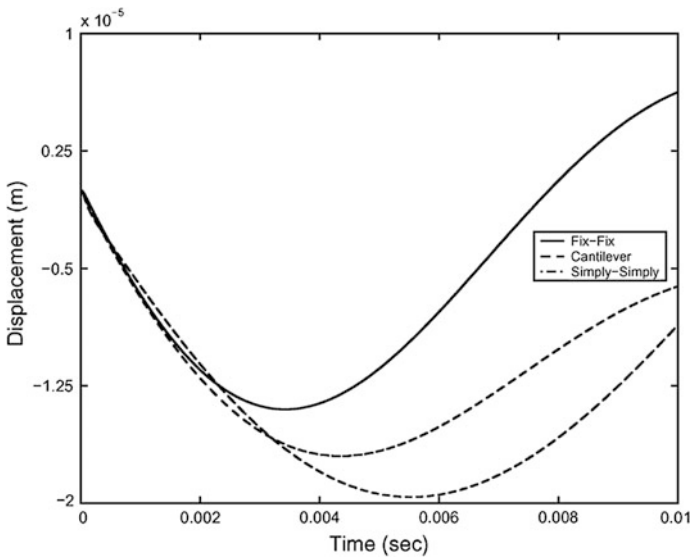
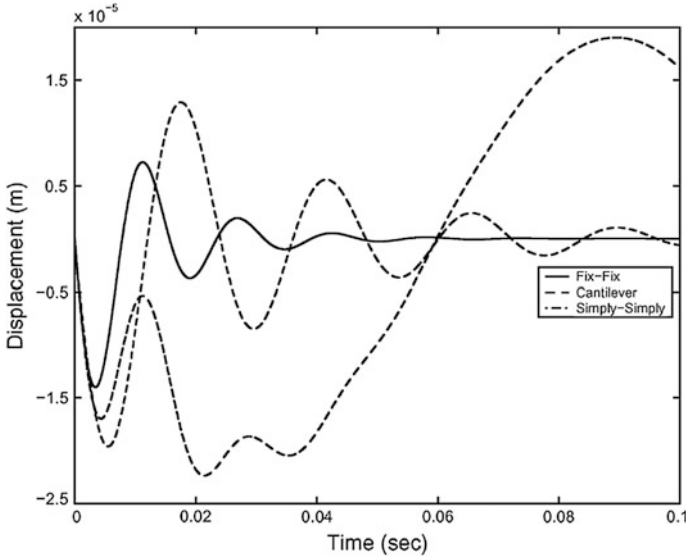


Fig. 2.21 Initial period displacement response for various configurations at the center of the beam [23]



**Fig. 2.22** Displacement response for various configurations at the center of the beam [23]

The recoil pressure is computed from Eq. (2.63). Moreover, the laser power intensity dissipated due to evaporation is:

$$I_{ev} \cong I_o - \dot{q}_{solid}$$

where  $\dot{q}_{solid}$  is the rate of energy dissipated in the solid phase. It should be noted that the rate of energy dissipated due to melting is considerably smaller than the rate of energy dissipated during evaporation; therefore, it is neglected.

The pressure force acting normal to the substrate surface can be written as:

$$F_o = \int_0^{r_e} Pr 2\pi r dr \quad (2.64)$$

where  $r_e$  is the radius of the evaporated surface. It should be noted that in the present study the evaporated surface, during the laser ablation, is considered as a circular shape with radius 0.4 mm, i.e.,  $r_e = 0.4$  mm. The variation of normal force with time is assumed as exponential, i.e.:

$$F(t) = F_o(\exp(-\beta t) - \exp(-\gamma t)) \quad (2.65)$$

where  $\beta$  and  $\gamma$  are constants. Figure 2.24 shows the normal pressure force.

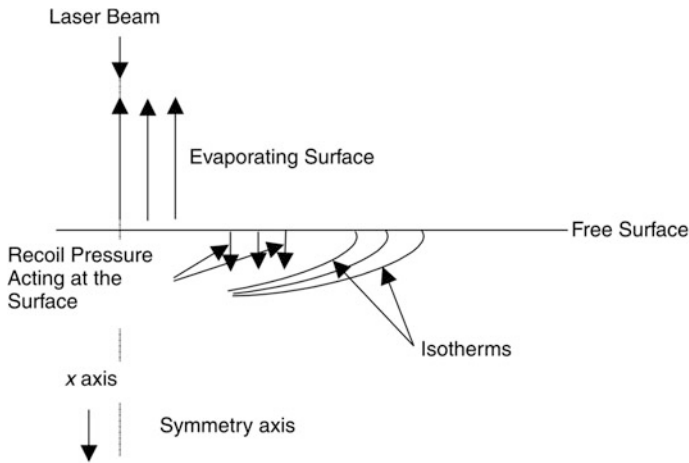


Fig. 2.23 A schematic view of laser workpiece interaction [24]

### 2.5.2 Flexural Wave Analysis

Flexural wave analysis is given above in Eqs. (2.26)–(2.40).

Initial and Boundary Conditions:

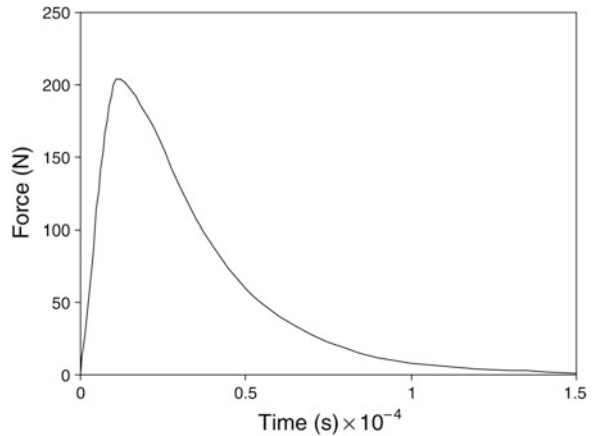
Initially the displacements are set to zero for a cantilever arrangement. At  $x = 0$  (at the fixed end), the displacement is always zero, i.e. at  $x = 0 : u = 0$ . It should be noted that in laser cutting of sheet metals, the workpiece is clamped at both ends. However, in the present situation, high magnitude flexural motion is required during the laser pulse heating process (during the cavity formation). This can be achieved by using a cantilever arrangement of the workpiece where the load due to recoil pressure should be acting at the free end of the workpiece.

### 2.5.3 Results and Discussions

In this case laser evaporative heating of three-layer assembly is considered and flexural wave generated due to the pressure force is investigated. Cantilever arrangement of the assembly is accommodated in the analysis. The location of laser evaporated spot is varied at the workpiece surface and the effect of pressure force location on the flexural wave characteristics is examined. Tables 2.5 and 2.6 give the mechanical and thermal properties of the substrate material employed in the simulations, respectively.

Figure 2.24 shows temporal variation of loading pressure force due to the recoil pressure. The magnitude of pressure force reaches as high as 200 kN. This is due to the high magnitude of recoil pressure generated during the ablation process. The

**Fig. 2.24** Temporal variation of pressure force [24]



temporal behavior of the pressure force is similar to that presented in the previous study [6].

Figure 2.25 shows the schematic view of the assembly and its geometric arrangements as well as the location of the mesh points where the flexural wave characteristics and stress levels are computed.

Figure 2.26 shows the temporal variation of the tip displacement (free end of the cantilever assembly) for different locations of the pressure force at the workpiece surface. The pressure force location is associated with the cell number as shown in Fig. 2.25. Due to high magnitude of the pressure force, the maximum flexural displacement is in order of  $45 \mu\text{m}$  at the tip of the cantilever assembly. The peak amplitude reduces sharply when the load position moves towards the fixed end of the assembly (5.1 nodal location). It should be noted that the nodal points of the elements in the assembly is shown in Fig. 2.25. The pressure force due to recoil pressure diminishes at about  $10^{-4}$  s; however, the amplitude of the flexural displacement of the assembly reaches maximum at about  $10^{-3}$  s. The time shift in the flexural displacement is due to the damping effect of the assembly arrangement and elastic and mass matrixes of the substrate material. Moreover, the location of the force does not alter the time occurrence of the peak amplitude, i.e. the peak amplitude of the flexural displacement corresponding to different locations of the pressure force occurs at the same time. Consequently, influence of pressure force on the time occurrence of the maximum displacement is insignificant.

## 2.6 Laser Ablation in Multilayer Assembly

In this section the analysis of the flexural characteristics of the multilayer assembly, the formulation and findings of the previous study [25] are considered. Thus, the flexural motion of the three- and four-layer assemblies is modelled. In

**Table 2.5** Mechanical properties of steel and Inconel 617 alloy

	Poisson's ratio $\nu$	Density ( $\text{kg/m}^3$ )	Elastic modulus (Pa)
Steel	0.3	7,830	$2.068 \times 10^{11}$
Inconel 625	0.313	8,460	$2.12 \times 10^{11}$

**Table 2.6** Thermal properties of steel and Inconel 625 alloy

	$C_p$ (J/Kg K)	$k$ (W/m K)	$\delta$ (1/m)	$\alpha$ ( $\text{m}^2/\text{s}$ )
Steel	460	80.3	$6.16 \times 10^7$	$0.22 \times 10^{-4}$
Inconel 625	425	14.4	$6.16 \times 10^7$	$0.38 \times 10^{-5}$

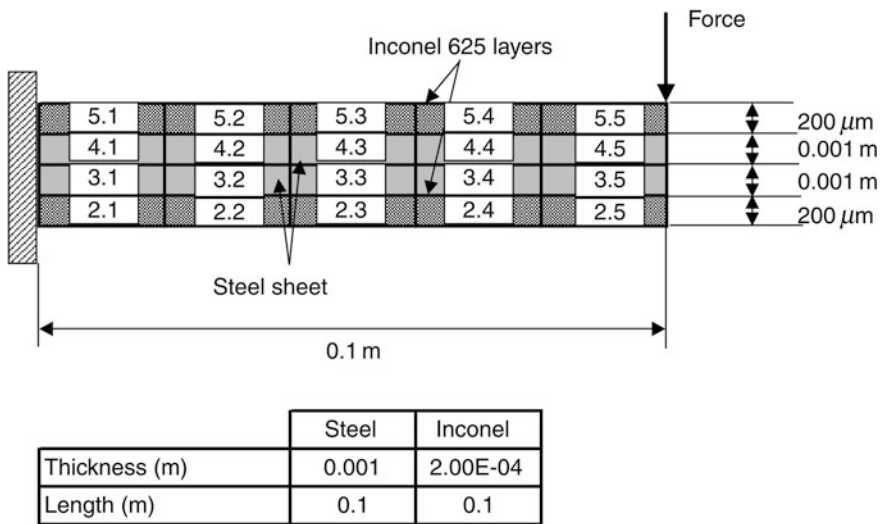


**Fig. 2.25** Workpiece arrangement and layers. *Numbers* represent the cell number for the locations in the assembly [24]

order to generate impact load at the workpiece surface for the flexural motion, the laser ablation of the surface is considered. The laser evaporative heating of the solid surface is modelled and recoil pressure generated during the evaporation process is formulated in order to account for the impact load. The three-layer assembly consists of two layers of steel and a single layer of Inconel 617 alloy, while the four-layer assembly consists of two layers of steel and two layers of Inconel 617 alloy.

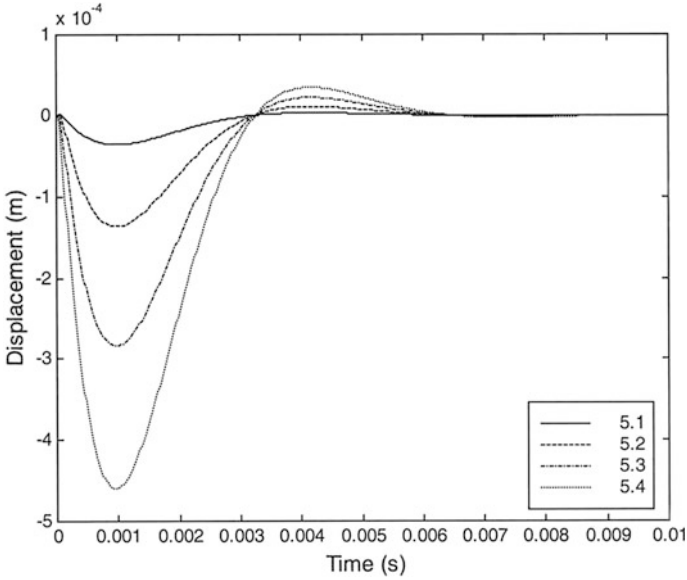


**Fig. 2.26** Temporal variation of flexural displacement for different pressure load location at the assembly surface as shown in Fig. 2.25 [24]

### 2.6.1 Heat Transfer Model

A schematic view of laser workpiece interaction for non-conduction limited heating situation is shown in Fig. 2.27. The heat transfer analysis is given above in Eqs. (2.20)–(2.24).

The pressure force acting normal to the substrate surface can be written as:

$$F_o = \int_0^{r_e} P 2\pi r dr$$

where  $r_e$  is the radius of the evaporated surface. It should be noted that in the present study the evaporated surface, during the laser ablation, is considered as a circular shape with radius 0.4 mm, i.e.,  $r_e = 0.4$  mm. The variation of normal force with time is assumed as exponential, i.e.:

$$F(t) = F_o(\exp(-\beta t) - \exp(-\gamma t))$$

where  $\beta$  and  $\gamma$  are constants. Figure 2.28 shows the normal pressure force.

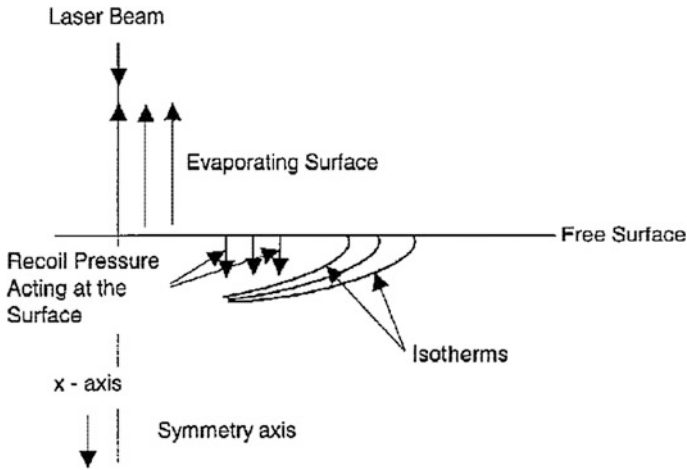


Fig. 2.27 A schematic view of laser workpiece interaction [25]

### 2.6.2 Flexural Wave Analysis

Flexural wave analysis is given above in Eqs. (2.26)–(2.40).

Initial and Boundary Conditions:

Initially the displacements are set to zero for a cantilever arrangement. At  $x = 0$  (at the fixed end), the displacement is always zero, i.e. at  $x = 0$ :  $u = 0$ . It should be noted that in laser cutting of sheet metals, the workpiece is clamped at both ends. However, in the present situation, high magnitude flexural motion is required during the laser pulse heating process (during the cavity formation). This can be achieved by using a cantilever arrangement of the workpiece where the load due to recoil pressure should be acting at the free end of the workpiece.

### 2.6.3 Results and Discussions

Laser non-conduction limited heating of multiplayer assembly is considered in this section. The recoil pressure developed at the vapor-liquid interface during the evaporation process is analyzed and the pressure force is considered as the impacting load generating the flexural motion of the workpiece. In order to obtain large amplitude flexural wave, a cantilever arrangement of the workpiece is taken into account and the impacting load is assumed to act close to the free end of the workpiece. Figure 2.29 illustrates the schematic view of the workpiece, the location of the impacting load and the elements used in the computation while Fig. 2.28 shows temporal variation of resulting pressure force (impacting load). Tables 2.7 and 2.8 give the material properties used in the simulations.

**Fig. 2.28** Temporal variation of pressure force [25]

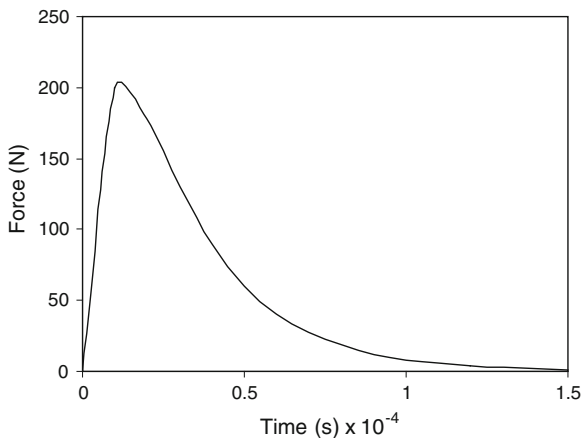


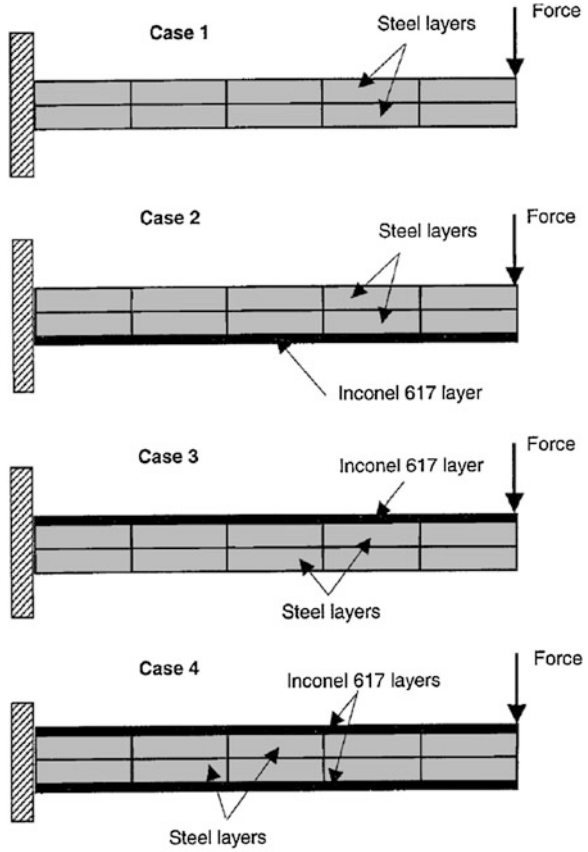
Figure 2.30 shows the displacement with time for four cases, which are illustrated in Fig. 2.29. The magnitude of displacement is higher for the case 1, and then follows the cases 2 and 3, and 4. The large displacement for case 1 is because of the number of layers in the assembly, which are 2 and the end location of cantilever arrangement of the workpiece, i.e. it results the maximum displacement of the order of 500  $\mu\text{m}$  in this region. Consequently, increasing number of layers from 2 to 4 reduces the displacement considerably despite the addition of two layers have thickness in the order of 400  $\mu\text{m}$ , i.e. each layer thickness is 200  $\mu\text{m}$  which is 1/10 of the steel layer thickness. However, thin layer of Inconel alloy reduces the amplitude of the flexural motion of the workpiece due to its properties as seen from Table 2.7, i.e. it has a high density. The cases for 2 and 3, in which the Inconel alloy layer is either at top or bottom, indicate that the location of Inconel alloy layer (whether at top or bottom) has no influence on the amplitude of the flexural motion.

Figure 2.31 shows equivalent stress (Fig. 2.29) for four cases. The maximum stress in the order of 20 MPa, which is less than the yield strength of the substrate materials. The time, at which the maximum stress occurs, corresponds to the time when the magnitude of displacement is maximum. It should be noted that although the displacement for cases 2 and 3 are almost identical, the magnitude of equivalent stress differs slightly, which is more pronounced when the stress is maximum. The stress level reduces to zero when the magnitude of displacement becomes zero.

Figure 2.32 shows shear stress with time for four cases. Shear stress behavior is similar to that corresponding to equivalent stress, provided that the maximum magnitude of shear stress is higher than that of equivalent stress. The small magnitude of shear stress is because of small displacement, which is in the order of  $10^{-4}$  m.

Figure 2.33 shows the maximum displacement for different cases. The maximum displacement is almost identical for the cases 2 and 3 and its magnitude

**Fig. 2.29** Workpiece arrangement and layers [25]



	Steel	Inconel
Thickness (m)	0.001	2.00E-04
Length (m)	0.1	0.1

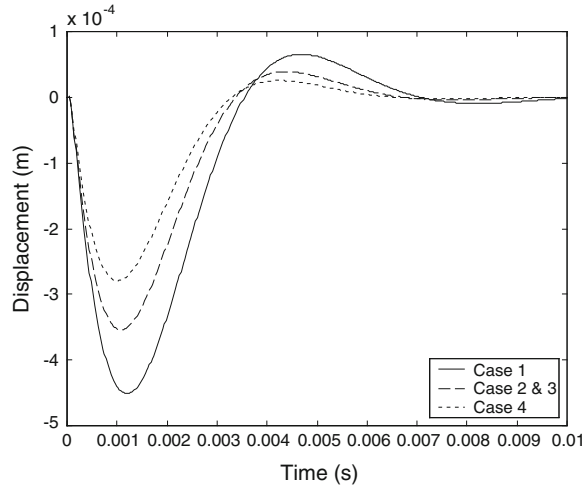
**Table 2.7** Mechanical properties of steel and Inconel 617 alloy

	Poisson's ratio $\nu$	Density ( $\text{kg/m}^3$ )	Elastic modulus (Pa)
Steel	0.3	7,830	$2.068 \times 10^{11}$
Inconel 617	0.312	8,440	$2.11 \times 10^{11}$

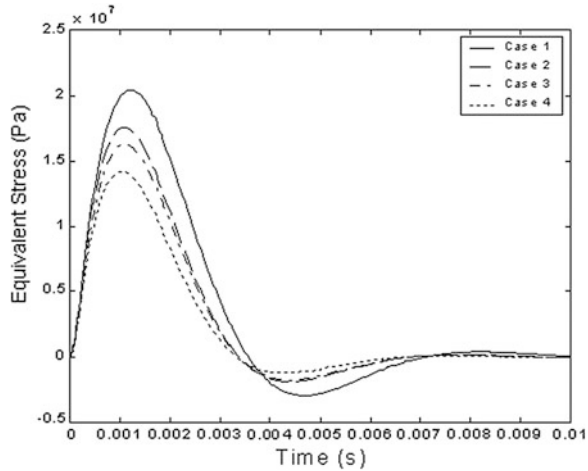
**Table 2.8** Thermal properties of steel and Inconel 617 alloy

	$C_p$ (J/Kg K)	$k$ (W/m K)	$\delta$ (1/m)	$\alpha$ ( $\text{m}^2/\text{s}$ )
Steel	460	80.3	$6.16 \times 10^7$	$0.22 \times 10^{-4}$
Inconel 617	419	13.4	$6.16 \times 10^7$	$0.38 \times 10^{-5}$

**Fig. 2.30** Temporal variation of displacement for different arrangements of workpiece layers (cases) [25]



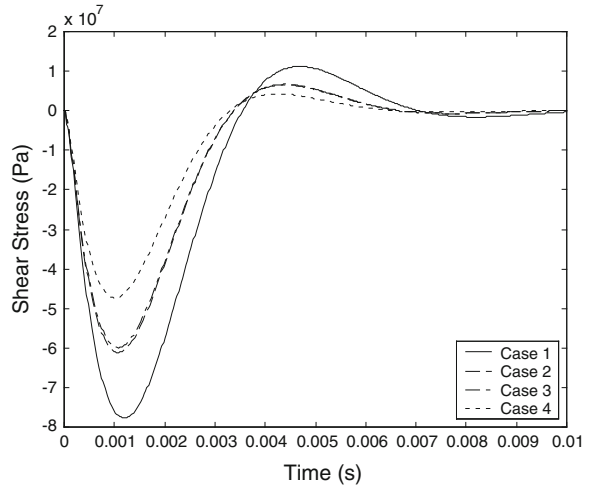
**Fig. 2.31** Temporal variation of equivalent stress for different arrangements of workpiece layers (cases) [25]



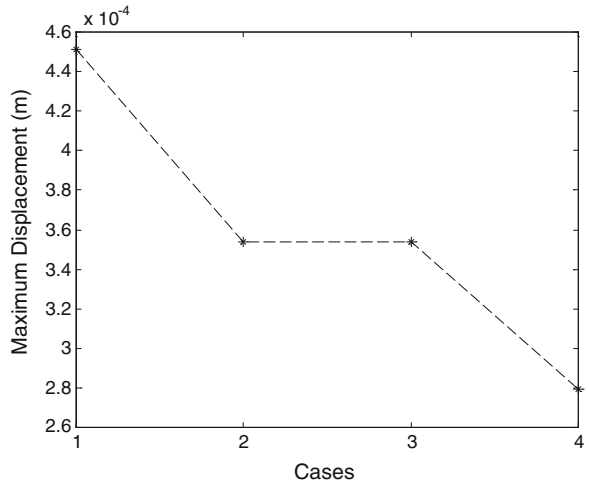
reduces more than 50 % for the case 4. Consequently, addition of thin Inconel layer influences the amplitude of the flexural motion considerably.

Figure 2.34 shows the maximum equivalent stress for different cases. The variation in equivalent stress with cases is not as considerable as the variation of maximum displacement. In this case, the magnitude of maximum equivalent stress reduces about 25 % for the case 4 while the magnitude of displacement reduces about 50 % for the same case.

**Fig. 2.32** Temporal variation of shear stress for different arrangements of workpiece layers (cases) [25]



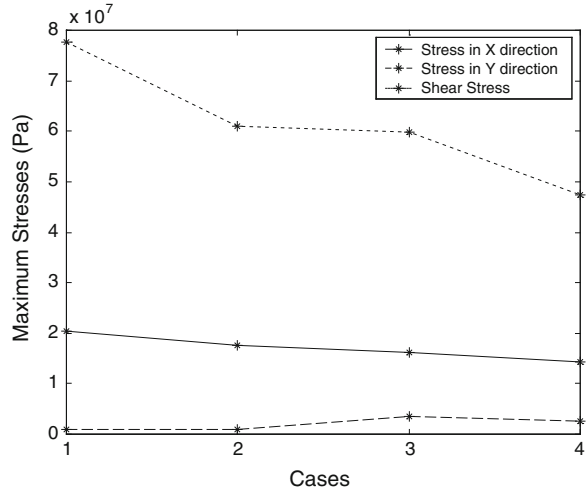
**Fig. 2.33** Maximum displacement for different arrangements of workpiece layers (cases) [25]



## 2.7 Cantilever Plate Heated at Fixed End

In the analysis of the flexural characteristics of the cantilever plate heated at fixed end, the formulation and findings of the previous study [26] are considered. In the present case, consider locally heated flat plated in a cantilever arrangement. Thus the effect of the size of the heat source on the flexural motion of the plate when subjected to the impulsive force at the free end of the plate is examined. A numerical scheme employing a Finite Element Method (FEM) is used to predict the frequency and the amplitude of the flexural motion of the plate. The influence of the size of the heat source is then correlated with the change in the frequency and the amplitude of the resulting flexural motion.

**Fig. 2.34** Temporal variation of maximum stress for different arrangements of workpiece layers (cases) [25]



**2.7.1 Mathematical Modeling Numerical Solution**

Consider a flat solid-like of finite thickness as shown in Fig. 2.35, where the geometry is defined by:

$$\bar{D} = \{(x,y,z): 0 \leq x \leq l; \quad 0 \leq y \leq h; \quad 0 \leq z \leq w\}$$

where  $\bar{D}$  is the space vector.

**2.7.2 Heat Transfer Analysis**

The transient diffusion equation based on the Fourier heating model can be written in the Cartesian coordinates as:

$$\rho c_p \frac{\partial T}{\partial t} = k \left( \frac{\partial^2 T}{\partial x^2} + \frac{\partial^2 T}{\partial y^2} + \frac{\partial^2 T}{\partial z^2} \right) \tag{2.66}$$

where  $\rho$  is the density,  $c_p$  is the specific heat capacity and  $k$  is the thermal conductivity. In a matrix form, Eq. (2.66) is written as:

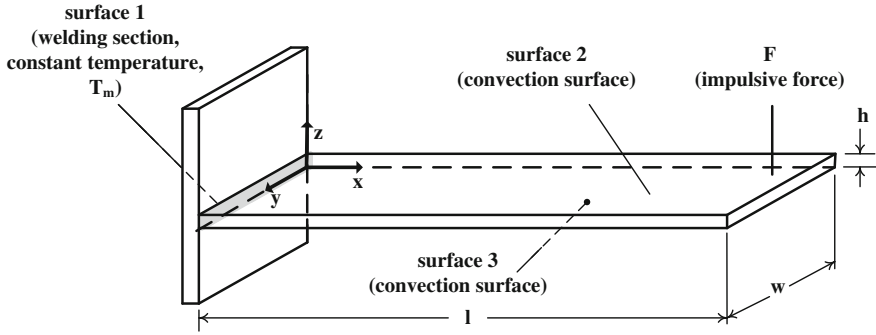


Fig. 2.35 The plate coordinate system [26]

$$\rho c_p \frac{\partial T}{\partial t} + [L]^T [q] = 0 \tag{2.67}$$

or

$$\rho c_p \frac{\partial T}{\partial t} = [L]^T ([D^t] [L] T) \tag{2.68}$$

where \$[q]\$ is the heat flux vector, \$[D^t]\$ is the thermal conductivity matrix:

$$[D^t] = \begin{bmatrix} k & 0 & 0 \\ 0 & k & 0 \\ 0 & 0 & k \end{bmatrix} \tag{2.69}$$

and \$[L]\$ is the vector operator and is defined as:

$$[L] = [\partial/\partial x \quad \partial/\partial y \quad \partial/\partial z]^T = \text{vector operator}$$

The thermal boundary conditions of the flat solid are as follows:

A constant temperature heat source is assumed at one of the following locations: surface 1 (as shown in Fig. 2.36) of the flat solid, i.e.,

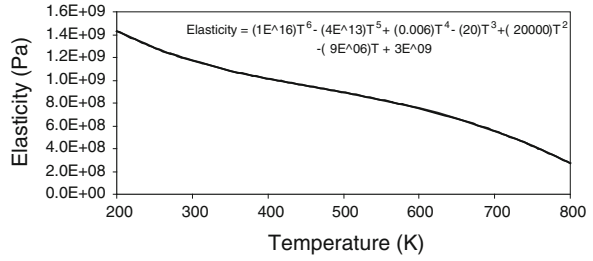
$$T = T_m \quad \text{at } x = 0, 0 \leq y \leq h, 0 \leq z \leq w$$

where \$T\_m\$ is the melting temperature of the flat solid material.

At the free surfaces (surfaces 2 and 3) (in \$x\$-\$y\$ plane at \$z = 0\$ and \$z = h\$) a convective boundary is assumed, therefore, the corresponding boundary condition is:

$$[q]^T [\eta] = h_f [T_s - T_B] \quad \text{at } z = 0 \text{ (surface 2) and } z = h \text{ (surface 3)}$$

**Fig. 2.36** Elastic modulus versus temperature curve [26]



where  $[\eta]$  is the unit outward normal vector,  $h_f$  is the heat transfer coefficient and  $T_s$  and  $T_B$  are the surface temperature and bulk temperature of adjacent fluid, respectively.

Initially the substrate material is assumed to be at a reference temperature,  $T_o$ , therefore, the initial condition becomes:

$$T = T_o \quad \text{at } t = 0$$

The thermal properties of the flat solid material used are given in Table 2.9. In finite element domain the flat solid is divided into SOLID98 ANSYS elements. The coupled-field 10-node (i, j, k, l, m, n, o, p, q and r) tetrahedral element has a quadratic displacement behavior. Each of the ten nodes has 3 structural (translations:  $u_x$ ,  $u_y$  and  $u_z$ ), and one thermal degrees of freedom at each node (temperature,  $T$ ) [27]. The heat balance equations for the finite element, in matrix form, is written as:

$$[C_e^t][\dot{T}_e] + ([K_e^{tb}] + [K_e^{tc}])[T_e] = [Q_e^c] \quad (2.70)$$

where

$$[C_e^t] = \rho \int_{\forall} c_p [N][N]^T d\forall = \text{element specific heat matrix}$$

$$[T_e] = [T_i \ T_j \ T_k \ T_l \ T_m \ T_n \ T_o \ T_p \ T_q \ T_r]^T = \text{nodal temperature vector of element}$$

$$[K_e^{tb}] = \int_{\forall} [B^t]^T [D^t] [B^t] d\forall = \text{element diffusion conductivity matrix}$$

$$[K_e^{tc}] = \int_{S_2} h_f [N][N]^T dS_2 + \int_{S_3} h_f [N][N]^T dS_3 = \text{element convection surface conductivity matrix}$$

$$[Q_e^c] = \int_{S_2} T_B h_f [N] q dS_2 + \int_{S_3} T_B h_f [N] q dS_3 = \text{element convection surface heat flow vector}$$

The element shape functions matrix,  $[N]$  relates the temperature variable,  $T$ , which is allowed to vary in both space and time, with the nodal temperature vector of element as follows:

**Table 2.9** The thermal properties of the flat solid material used in the simulations

Thermal conductivity, $k$ (W/m K)	53
Specific heat, $c_p$ (J/kg K)	520
Poisson's ratio, $\nu$	0.29
Thermal expansion coefficient, $\alpha$ (1/K)	$1.5 \times 10^{-5}$
Density, $\rho$ (kg/m <sup>3</sup> )	7,880
Damping coefficient	0.015

$$T(x,y,z,t) = [N]^T [T_e] \tag{2.71}$$

For a 10-node tetrahedral ANSYS element, the shape functions matrix (for all degrees of freedom) is written as:

$$[N] = \begin{bmatrix} (2L_1 - 1)L_1 & 0 & 0 & 0 & 0 & 0 & 0 & 0 & 0 & 0 \\ 0 & (2L_2 - 1)L_2 & 0 & 0 & 0 & 0 & 0 & 0 & 0 & 0 \\ 0 & 0 & (2L_3 - 1)L_3 & 0 & 0 & 0 & 0 & 0 & 0 & 0 \\ 0 & 0 & 0 & (2L_4 - 1)L_4 & 0 & 0 & 0 & 0 & 0 & 0 \\ 0 & 0 & 0 & 0 & 4L_1L_2 & 0 & 0 & 0 & 0 & 0 \\ 0 & 0 & 0 & 0 & 0 & L_2L_3 & 0 & 0 & 0 & 0 \\ 0 & 0 & 0 & 0 & 0 & 0 & L_1L_3 & 0 & 0 & 0 \\ 0 & 0 & 0 & 0 & 0 & 0 & 0 & L_1L_4 & 0 & 0 \\ 0 & 0 & 0 & 0 & 0 & 0 & 0 & 0 & L_2L_4 & 0 \\ 0 & 0 & 0 & 0 & 0 & 0 & 0 & 0 & 0 & L_3L_4 \end{bmatrix} \tag{2.72}$$

where  $L_1, L_2, L_3$  and  $L_4$  are the normalized coordinates going from 0.0 at a vertex to 1.0 at the opposite side. Matrix  $[B^t]$  is defined as:

$$[B^t] = [L] [N] T \tag{2.73}$$

### 2.7.3 Flexural Wave Analysis

The finite element, in matrix form, description of the flexural motion of the flat solid is written as:

$$[M_e^s] [\ddot{U}_e] + [C_e^s] [\dot{U}_e] + [K_e^s] [U_e] = [F_e^{th}] + [F_e^{nd}] \tag{2.74}$$

where

$$[M_e^s] = \rho \int_V [N]^T [N] dV = \text{element mass matrix}$$

$$[U_e] = [u_i \ u_j \ u_k \ u_l \ u_m \ u_n \ u_o \ u_p \ u_q \ u_r]^T = \text{nodal displacement vector of element}$$

$$[C_e^s] = \text{structural damping matrix}$$

$$[\mathbf{K}_e^s] = \int_{\forall} [\mathbf{B}^s]^T [\mathbf{D}^s] [\mathbf{B}^s] d\forall = \text{element stiffness matrix}$$

$$[\mathbf{F}_e^{\text{th}}] = \int_{\forall} [\mathbf{B}^s]^T [\mathbf{D}^s] [\boldsymbol{\varepsilon}^{\text{th}}] d\forall = \text{element thermal load vector}$$

$$[\mathbf{F}_e^{\text{nd}}] = \text{vector of nodal forces applied to the element}$$

where  $[\mathbf{B}^s]$  is the strain-displacement matrix, based on the element shape factors and relates the strain displacement vector,  $[\boldsymbol{\varepsilon}]$ , with the nodal displacements vector,  $[\mathbf{U}]$  by:

$$[\boldsymbol{\varepsilon}] = [\mathbf{B}^s] [\mathbf{U}] \quad (2.75)$$

and  $[\mathbf{D}^s]$  is the elasticity matrix and defines the relation between stress and strain vectors as:

$$[\boldsymbol{\sigma}] = [\sigma_x \sigma_y \sigma_z \sigma_{xy} \sigma_{yz} \sigma_{xz}]^T = [\mathbf{D}^s] [\boldsymbol{\varepsilon}^{\text{el}}] = [\mathbf{D}^s] \left[ [\boldsymbol{\varepsilon}] - [\boldsymbol{\varepsilon}^{\text{th}}] \right] \quad (2.76)$$

where:

$$[\boldsymbol{\varepsilon}^{\text{el}}] = \text{elastic strain vector} \quad (2.77)$$

$$[\boldsymbol{\varepsilon}^{\text{th}}] = (T - T_0) [\alpha \alpha \alpha 0 0 0]^T = \text{thermal strain vector} \quad (2.78)$$

and

$$[\boldsymbol{\varepsilon}] = [\varepsilon_x \varepsilon_y \varepsilon_z \varepsilon_{xy} \varepsilon_{yz} \varepsilon_{xz}]^T = \text{total strain vector} \quad (2.79)$$

where  $\alpha$  is the thermal expansion coefficient of the flat solid material. The structural properties of the flat solid material are given in Table 2.10, while Fig. 2.36 presents the elastic modulus (E) versus temperature (T). The elasticity matrix,  $[\mathbf{D}^s]$ , is inversely defined as the flexibility (or compliance) matrix,  $[\mathbf{D}^s]^{-1}$ , which is written as:

$$[\mathbf{D}^s]^{-1} = \frac{1}{E} \begin{bmatrix} 1 & -\nu & -\nu & 0 & 0 & 0 \\ -\nu & 1 & -\nu & 0 & 0 & 0 \\ -\nu & -\nu & 1 & 0 & 0 & 0 \\ 0 & 0 & 0 & 2(1+\nu)/E & 0 & 0 \\ 0 & 0 & 0 & 0 & 2(1+\nu)/E & 0 \\ 0 & 0 & 0 & 0 & 0 & 2(1+\nu)/E \end{bmatrix} \quad (2.80)$$

where  $\nu$  is Poisson's ratio.

The structural boundary conditions of the flat solid are as follows:

At the fixed end, the displacement in all directions is always zero i.e. at  $x = 0$ :  $u_x = u_y = u_z = 0$ . It should be noted that in laser cutting of sheet metals, the workpiece is clamped at both ends. However, in the present situation, high

**Table 2.10** Description of the impulsive loads employed in the present study

Size of constant heating source (w)	Heating time at which impulsive load is applied (s)	Amplitude of impulsive load, F (N)	Duration of impulsive load (s)
0.25	2.5	1	0.001
0.50	5	1	0.001
0.75	7.5	1	0.001
1	10	1	0.001

magnitude flexural motion is required during the laser pulse heating process (during the cavity formation). This can be achieved by using a cantilever arrangement of the workpiece where the load due to recoil pressure should be acting at the free end of the workpiece. Initially the displacements are set to zero for a cantilever arrangement.

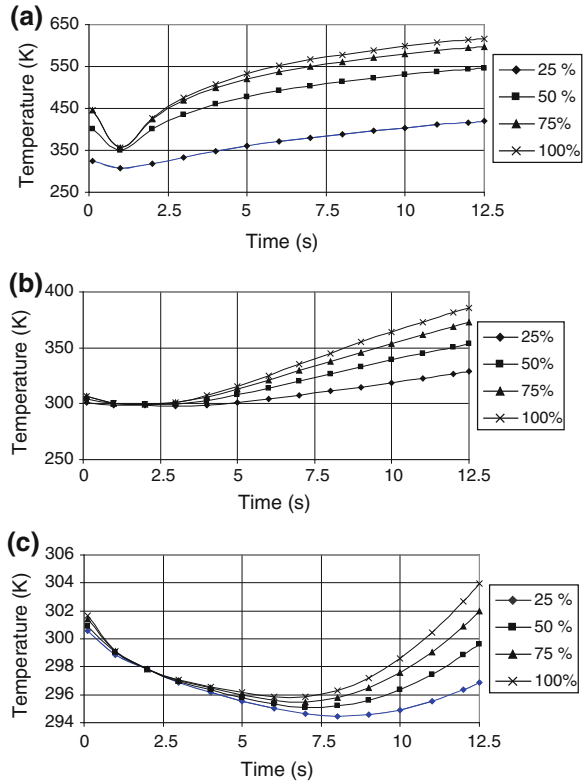
The grid size independency heat transfer and flexural studies were carried to determine the optimum grid size of the flat solid. The flat solid dimensions employed in the present study were as follows: 0.15 m for length,  $l$ , 0.05 m for width,  $w$ , and 0.0015 m for thickness,  $h$ . The impulsive force exciting the free end of plate is as described in Table 2.10. The flexural properties of the plate material are presented in Fig. 2.36.

#### 2.7.4 Results and Discussion

The flexural motion of cantilever assembly heated at the fixed end is considered and the effect of the size of the heat affected zone in the flexural motion is examined. The constant temperature heat source is assumed at the fixed edge while an impulsive load is applied at the free end of the cantilever assembly. The size of the heat source is varied while the load level is kept constant in the analysis. Temperature dependent thermal and mechanical properties of steel are accommodated in the simulations.

Figure 2.37 shows temporal variation of temperature at 0.5 width of the plate in the z-axis (mid-plane of the plate) and at different x-axis locations for various sizes of the constant temperature heat source at the fixed end of the cantilever assembly. Temperature rises rapidly in the early heating periods and temperature rise becomes gradual as the heating progresses with time. This is particularly true for the location  $x = L/15$  ( $L$  being the length of the plate). The rapid rise of temperature in the early heating period is associated with the conduction heat transfer in the vicinity of the heat source, since location  $x = L/15$  is close to the heat source at the fixed end. In the early heating period, temperature gradient is high in the neighborhood region of the heat source. This enhances the heat conduction from the heat source to its neighborhood. Consequently, temperature in the neighborhood of the fixed end rises rapidly. As the time progresses, the temperature gradient becomes low due to initially rapid rise of temperature in the region

**Fig. 2.37** Temporal variations of temperature at plate mid-plane ( $z = 0.5$  W) for different  $x$ -locations [26].  
**a**  $x = 0.01$  m ( $x = L/15$ ).  
**b**  $x = 0.03$  m ( $x = L/5$ ).  
**c**  $x = 0.05$  m ( $x = L/3$ )



next to the heat source. This results in gradual rise of temperature with progressing time. Similar arguments are true for all the sizes of the heat source, provided that magnitude of temperature increases slightly with size of the heat source at the end of 12.5 s of heating duration. However, temperature rise is low as the  $x$ -axis location increases to  $x = L/5$  for all the sizes of the heat source. This is because of the time taken for temperature rise through the heat conduction, which is long.

Figure 2.38 shows the flexural motion of the cantilever plate for different sizes of the constant temperature heat source. It should be noted that the time shift of the flexural response of the cantilever plate is obtained through subtracting the time response of the corresponding flexural motion with heating and no heating situations. Moreover, the amplitude shift is obtained through the maximum amplitude difference of the corresponding flexural motion with heating and without heating situations. When the size of the heat source increases, the changes in the amplitude of the flexural motion increases sharply and this increase becomes gradual as the size of the heat source increases further. This is associated with the temperature field in the substrate material, which modifies the elastic modulus of the substrate material (Fig. 2.36). In this case, increasing the size of the heat source enhances the high temperature region in the material through heat diffusion. This lowers the elastic modulus and modifies the displacement of the flexural motion of the

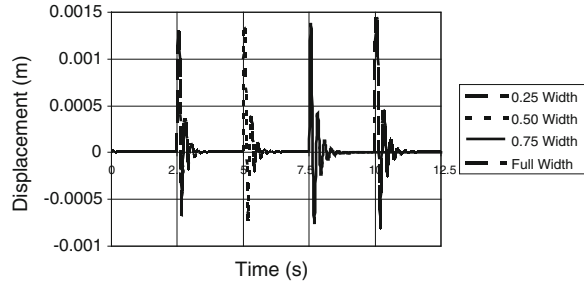
cantilever plate. Moreover, once the size of the heat source increase further, the heat diffusion enhances into the substrate material modifying the elastic modulus further, provided that the amplitude of the flexural motion is not affected significantly. This is because of the size of high temperature ( $T > 500$  K) region, which does not extend significantly as compared to the extension of the low temperature region in the plate ( $T < 500$  K). It should be noted that the elastic modulus varies in a non-linear form with temperature and the magnitude of this variation becomes high for temperatures greater than 500 K. The limited size of extension of the high temperature region in the substrate material is associated with the diffusion mechanism, which is governed by the temperature gradient. Since the constant temperature heat source has temperature less than the melting temperature of the substrate material, due to avoiding the phase change process, the temperature gradient remains low in the region next to the heat source. However, as the distance from the heat source increases further along the x-axis, the temperature gradient reduces significantly enhancing the heat diffusion (Fig. 2.38). Therefore, high temperature region is only limited with the small size in the neighborhood of the heat source. Consequently, amplitude of the flexural motion does not vary much with further increasing of the constant heat temperature source size.

In the case of the time shift, of the flexural motion (Fig. 2.38), a gradual increase in the time shift with the size of the constant temperature heat source is observed. The gradual change in the time shift is because of the temporal response of the substrate material to the constant heat source. Since, for each case, the excitation loads is applied from the free end of the plate after the 2.5 s time steps, which is also seen from Fig. 2.38, heat diffusion into the substrate material enhances with progressing time and elastic modulus is modified accordingly. Therefore, the time shift between no-heating and heating situations is affected by the heating duration prior to the excitation load is applied. Moreover, the region where the heat is diffused increases with increasing the rise of the constant temperature heat source. Consequently, by the time, at which the excitation load is applied, heat diffusion enhances with increasing heat source size. This, in turn, increases the time shift between the frequency of the flexural motion corresponding to heating and no-heating situations of the plate. It is, therefore, expected that the time shift of the flexural motion with and without heating situations enables to determine the size of the heat source at the fixed end of the cantilever plate. It is also equally true that the measuring the maximum amplitude difference between the flexural waves with heating and no-heating situations of the palate enables to determine the size of the heat source at the fixed end of the cantilever plate.

## 2.8 Welding of Bar to Rigid Body

The mathematical analysis and the findings for welding of bar to rigid body are presented below in line with the previous study [28]. Flexural motion of a bar, resembling cantilever beam, subjected to one side welding is discussed in this

**Fig. 2.38** Flexural motion of plate for different sizes of constant heat source [26]



section. The wave characteristics of the bar motion will be correlated with the size of the heat affected zone during the welding process.

The bar which has a finite thickness is shown in Fig. 2.39. The bar dimensions employed in the present study were as follows: 0.15 m for length,  $l$ , 0.05 m for width,  $s$ , and 0.0015 m for thickness,  $w$ .

### 2.8.1 Heat Transfer Analysis

The transient diffusion equation based on the Fourier heating model can be written in the Cartesian coordinates as:

$$\rho c_p \frac{\partial T}{\partial t} = k \left( \frac{\partial^2 T}{\partial x^2} + \frac{\partial^2 T}{\partial y^2} + \frac{\partial^2 T}{\partial z^2} \right) \quad (2.81)$$

where  $\rho$  is the density,  $c_p$  is the specific heat capacity and  $k$  is the thermal conductivity.

The thermal boundary conditions of the bar are as follows:

A constant temperature heat source is assumed at the fixed end (surface 1) of the bar, i.e.

$$T = T_m \quad \text{at } x = 0, 0 \leq y \leq s, 0 \leq z \leq w$$

where  $T_m$  is the melting temperature of the flat solid material.

At the free surfaces (surfaces 2 and 3) (in  $x$ - $y$  plane at  $z = 0$  and  $z = w$ ) a convective boundary is assumed, therefore, the corresponding boundary condition is:

$$[q]^T [\eta] = h_f [T_s - T_B] \quad \text{at } z = 0 (\text{surface 2}) \text{ and } z = w (\text{surface 3})$$

where  $[\eta]$  is the unit outward normal vector,  $h_f$  is the heat transfer coefficient and  $T_s$  and  $T_B$  are the surface temperature and bulk temperature of adjacent fluid, respectively.

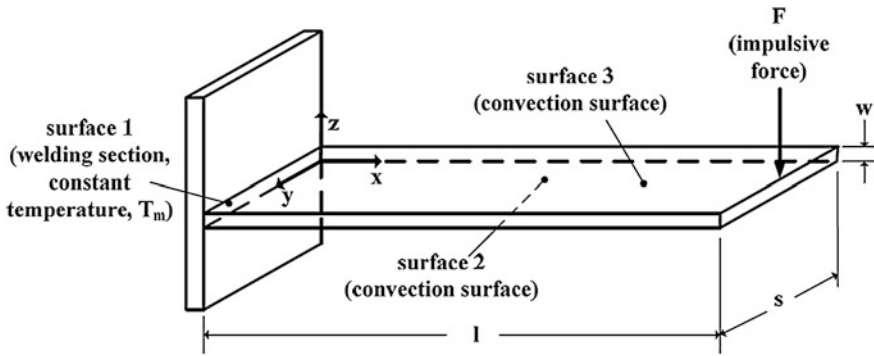


Fig. 2.39 Heating situation and coordinate system [28]

Initially the substrate material is assumed to be at a reference temperature,  $T_0$ , therefore, the initial condition becomes:

$$T = T_0 \quad \text{at } t = 0$$

The thermal properties of the bar material used are given as: 53 W/m K for thermal conductivity and 520 J/kg k for specific heat. In finite element domain the bar is divided into SOLID98 ANSYS elements. The coupled-filed 10-node tetrahedral element has a quadratic displacement behavior.

Each of the ten nodes has 3 structural translations and one thermal degrees of freedom at each node (temperature, T).

### 2.8.1.1 Flexural Motion Analysis

The finite element, in matrix form, description of the flexural motion of the bar is written as:

$$[M_e^s] [\ddot{U}_e] + [C_e^s] [\dot{U}_e] + [K_e^s] [U_e] = [F_e^{th}] + [F_e^{nd}] \quad (2.82)$$

where,

- $[M_e^s]$  = element mass matrix
- $[U_e]$  = nodal displacement vector of element
- $[C_e^s]$  = structural damping matrix
- $[K_e^s]$  = element stiffness matrix
- $[F_e^{th}]$  = element thermal load vector
- $[F_e^{nd}]$  = vector of nodal forces applied to the element

The structural boundary conditions of the bar are as follows: at the fixed end (at  $x = 0$ ), the displacement in all directions is always zero. It should be noted that in

laser cutting of sheet metals, the workpiece is clamped at both ends. However, in the present situation, high magnitude flexural motion is required during the laser pulse heating process (during the cavity formation). This can be achieved by using a cantilever arrangement of the workpiece where the load due to recoil pressure should be acting at the free end of the workpiece. Initially the displacements are set to zero for a cantilever arrangement. The structural material properties are given as:  $7,880 \text{ kg/m}^3$  for density, 0.015 for damping coefficient and  $1.5 \times 10^{-5} \text{ 1/K}$  for thermal expansion coefficient.

The grid size independency heat transfer and flexural studies were carried to determine the optimum grid size of the flat solid. For obtaining a maximum accuracy of results, it was decided to use a grid size of 438 elements. In carrying the grid independency studies, the time step size used for integration was taken as 0.0006 s, which was determined, based from studies that were carried to determine the required time step size.

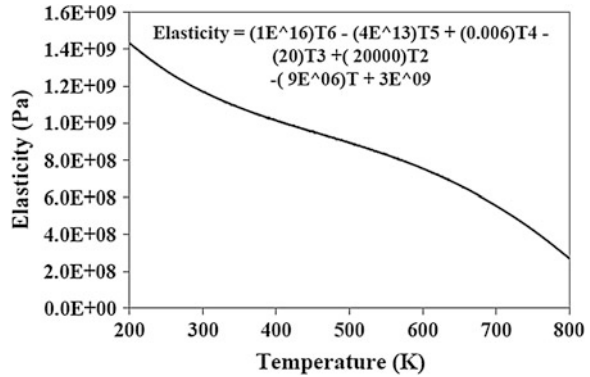
### 2.8.2 Results and Analysis

Heating of a bar resembling a welding situation is considered and temperature field is predicted. The bar is fixed at one end and heated at constant temperature at the fixed end. The temperature of the heat source is maintained at melting temperature of the bar material. (800 K). Since the elastic modulus changes with temperature (see Fig. 2.40), flexural motion of the bar when excited at the free end with an impulsive force as described in Fig. 2.41, is modeled. The impulse force is applied at different heating durations and displacements as well as frequency of the flexural motion of the bar are computed accordingly. Moreover, knowing the temperature distribution and the size of the heat affected zone, wave characteristics of the flexible motion are related to the temperature field in the bar.

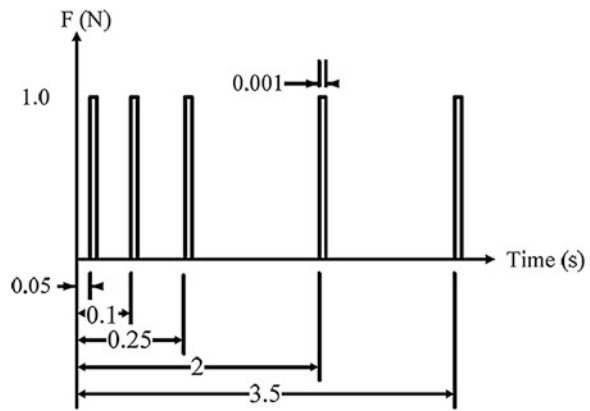
Figure 2.42 shows temperature distribution at the centerline for different heating durations. Temperature difference in region close to the heating section decays sharply and as the distance increases towards the bar free end, the temperature decays gradually. This is more pronounced in the early heating period. In this case, internal energy gain of the substrate material from the heat source increases and conduction losses towards bar free end becomes low in the early heating period. This results in sharp decay of the temperature in the vicinity of the heat source. However, as the time progresses temperature gradient remains high and heat diffusion from high temperature region to the bar end enhances, which lowers temperature decay in the region close to the heated zone. Since the modulus of elasticity varies with temperature, increasing temperature in the heated region of the bar lowers the modulus of elasticity. This becomes significant as the heating period progresses, i.e. the variation in the modulus of elasticity extends towards the free end of the bar with progressing heating period.

Figure 2.43 shows the wave behavior of flexural motion at different heating durations when the bar is excited by an impulsive force at different heating

**Fig. 2.40** Elastic modulus versus temperature curve [28]

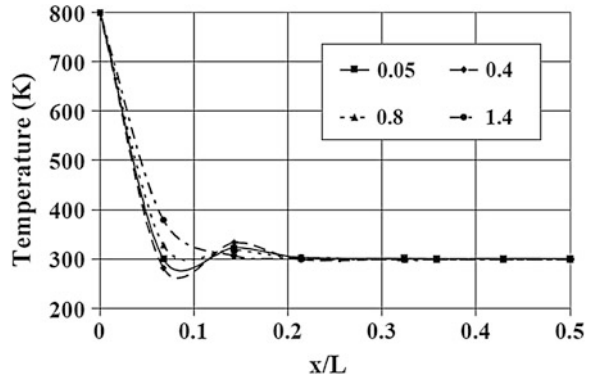


**Fig. 2.41** Description of the impulsive loads employed in the present study [28]



durations as well as when the bar is excited with no heating situation. The wave characteristics are computed at the free end of the flat solid where amplitude of flexural motion is the maximum. The characteristics of flexural waves (amplitude and frequency) due to heating and no heating situations is almost the same at time 0.05 s when the impulse force is applied, i.e. slight variation in amplitudes is observed for both flexural waves corresponding to heating and no heating conditions. The flexural wave amplitude is smaller for no heating situation than that of heating situation due to the change in the modulus of elasticity with temperature. However, difference in amplitude of both waves is more pronounced for heating periods of 0.1 and 0.25 s. this is because of the variation in modulus of elasticity, which results in change of flexural wave characteristics. Consequently, the wave characteristics are modified by the temperature field through change in modulus of elasticity. As the heating period progresses, the difference between both wave characteristics becomes small; in which case, the difference in wave amplitude due to heating and no heating situations becomes small. This is because of the reflected wave from the free end of the bar, which modifies the wave characteristics as well

**Fig. 2.42** Temperature distributions at bar center line during different heating durations [28]



as temperature field which extends into the bar with progressing time modifying the elastic module in the heated region. Consequently, change of the elastic modulus due to temperature field and the reflected wave from the free end of the bar modifies the wave characteristics during the long heating period.

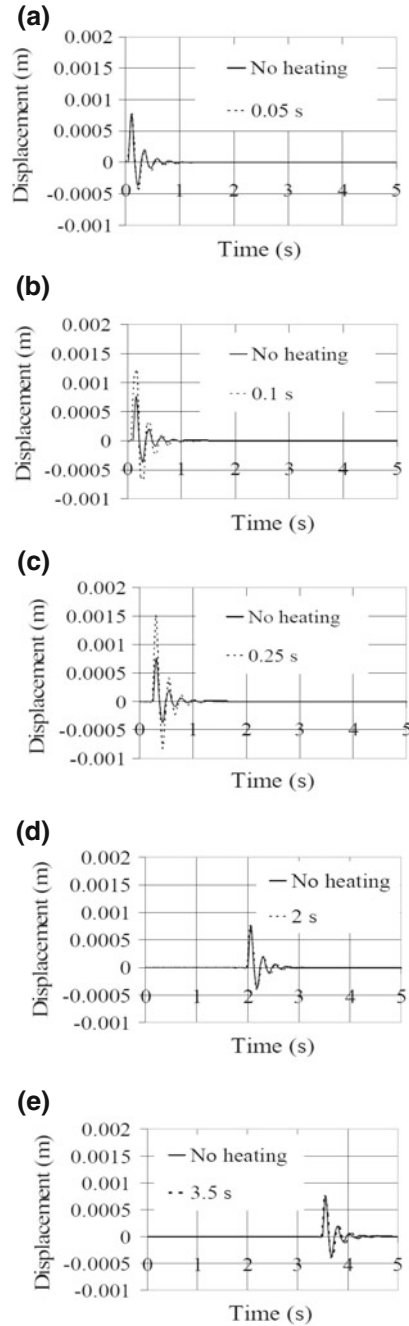
As the heating progresses, high temperature region extends into the bar with gradual temperature decay towards the bar end. This causes the modulus of elasticity decay gradually in this region. Consequently, the wave characteristics of the flexural motion are modified in such a way that the maximum amplitude difference in both waves becomes small. Therefore, the effect of temperature decay in the bar on the maximum amplitude is significant as similar to the time shift of both waves.

## 2.9 Local Heating of a Bar: Effect of Heat Source Location

In the current analysis of the flexural characteristics of the bar, the formulation and findings of the previous study [29] are considered. The flexural behavior of a uniform rectangular bar considered in this case has a  $w$  width, a  $l$  length and  $h$  thickness with cantilever arrangement, as shown in Fig. 2.44. The effects of the local heat source, resembling the immediately after the electric resistance welding process, on the wave characteristics are examined when an impulsive load is applied at the tip of the bar. The heat source is introduced along the width of the bar and the location of the heat source is changed along the length of the bar (at  $x = 0, 0.25, 0.5$  and  $0.75l$ ). Since the elastic modulus of the bar is considered as temperature dependent, the change of the location of the heat source modifies the wave characteristics. This enables examination of the change of heat source location and corresponding variation of the magnitude and frequency of the flexural wave.

**Fig. 2.43** Flexural motion at different heating durations when the bar is excited by an impulsive force at different heating durations [28].

- a** Impulsive load applied at heating time = 0.05 s.
- b** Impulsive load applied at heating time = 0.1 s.
- c** Impulsive load applied at heating time = 0.25 s.
- d** Impulsive load applied at heating time = 2.0 s.
- e** Impulsive load applied at heating time = 3.5 s



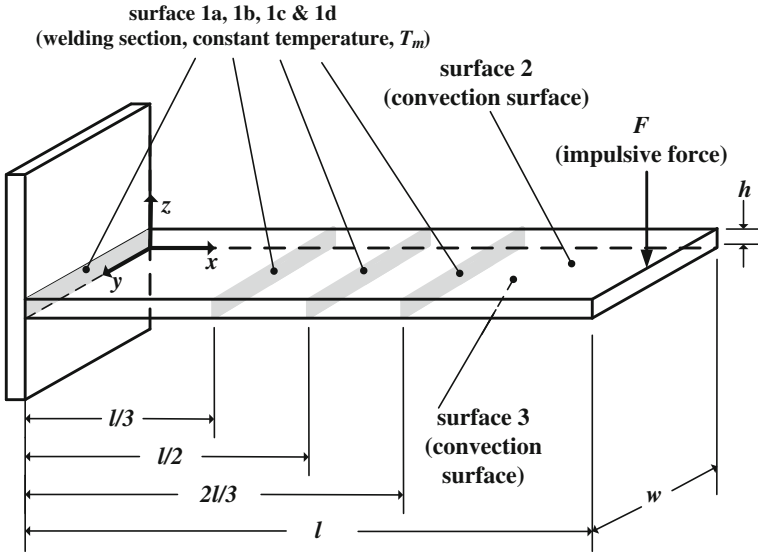


Fig. 2.44 The plate coordinate system and locations of heating load [29]

### 2.9.1 Mathematical Modeling Numerical Solution

The transient diffusion equation based on the Fourier heating model can be written in the Cartesian coordinates as:

$$\rho c_p \frac{\partial T}{\partial t} = k \left( \frac{\partial^2 T}{\partial x^2} + \frac{\partial^2 T}{\partial y^2} + \frac{\partial^2 T}{\partial z^2} \right) \tag{2.83}$$

where  $\rho$  is the density,  $c_p$  is the specific heat capacity and  $k$  is the thermal conductivity. The thermal boundary conditions of the flat solid are as follows:

A constant temperature heat source is assumed at one of the following locations: 1a or 1b or 1c or 1d, as shown in Fig. 2.44, of the uniform bar, i.e.,

$$T = T_m \quad \text{at } 0 \leq y \leq h, \quad 0 \leq z \leq w$$

where  $T_m$  is the melting temperature of the flat solid material.

At the free surfaces (surfaces 2 and 3) (in  $x$ - $y$  plane at  $z = 0$  and  $z = h$ ) a convective boundary is assumed, therefore, the corresponding boundary condition is:

$$[q]^T [\eta] = h_f [T_s - T_B] \quad \text{at } z = 0 \text{ (surface 2) and } z = h \text{ (surface 3)}$$

where  $[\eta]$  is the unit outward normal vector,  $h_f$  is the heat transfer coefficient and  $T_s$  and  $T_B$  are the surface temperature and bulk temperature of adjacent fluid, respectively.

Initially the substrate material is assumed to be at a reference temperature,  $T_o$ , therefore, the initial condition becomes:

$$T = T_o \quad \text{at } t = 0$$

The properties of the uniform bar material used are given in Table 2.11. In finite element domain the uniform bar is divided into SOLID98 ANSYS elements. The coupled-filed 10-node tetrahedral element has a quadratic displacement behavior. Each of the ten nodes has 3 structural translations and one thermal degrees of freedom at each node (temperature, T) [27].

To compare the numerical predictions with the analytical solution presented in the open literature for the no heating situation, the analytical formulation is introduced. In this case, the differential equation describing the flexural motion of a bar with no heating condition is given as [30]:

$$\frac{d^4 z}{dx^4} - \left( \frac{\omega^2 m}{EI} \right) y = 0 \quad (2.84)$$

where  $\omega$  represents the natural frequency values satisfying solution of Eq. (2.84) for certain boundary conditions. E is the modulus of elasticity of the bar material, I is the mass moment of inertia and m is the mass per unit length of the bar. The general solution of Eq. (2.84) is presented as follows:

$$\begin{aligned} z = & A \cosh \left( \left( \frac{m\omega^2}{EI} \right)^{1/4} x \right) + B \sinh \left( \left( \frac{m\omega^2}{EI} \right)^{1/4} x \right) \\ & + C \cos \left( \left( \frac{m\omega^2}{EI} \right)^{1/4} x \right) + D \sin \left( \left( \frac{m\omega^2}{EI} \right)^{1/4} x \right) \end{aligned} \quad (2.85)$$

where A, B, C and D are the integration constants and can be found after substituting the following boundary conditions in Eq. (2.85): at the clamped end of the uniform bar ( $x = 0$ ):

$$y|_{x=0} = 0 \quad \text{and} \quad \left. \frac{dy(x)}{dx} \right|_{x=0} = 0$$

at the free end ( $x = l$ ):

$$\left. \frac{d^2 y(x)}{dx^2} \right|_{x=l} = 0 \quad \text{and} \quad \left. \frac{d^3 y(x)}{dx^3} \right|_{x=l} = 0,$$

which reduces Eq. (2.85) into:

**Table 2.11** The thermal properties of the flat solid material used in the simulations

Thermal conductivity, $k$ (W/m K)	53
Specific heat, $c_p$ (J/kg K)	520
Poisson's ratio, $\nu$	0.29
Thermal expansion coefficient, $\alpha$ (1/K)	$1.5 \times 10^{-5}$
Density, $\rho$ (kg/m <sup>3</sup> )	7,880
Damping coefficient, $\zeta$	0.015

$$\cosh \left( \left( \frac{m\omega^2}{EI} \right)^{1/4} l \right) \cos \left( \left( \frac{m\omega^2}{EI} \right)^{1/4} l \right) + 1 = 0 \quad (2.86)$$

According to [30, 31], the resulting fundamental natural frequency corresponding to the first mode of motion for the uniform bar is:

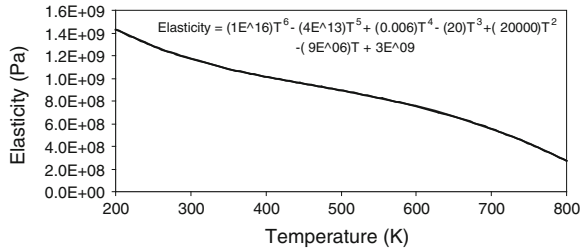
$$\omega_{fundamental} = 1.875^2 \sqrt{\frac{EI}{ml^4}} \quad (2.87)$$

Figure 2.45 presents the elastic modulus (E) versus temperature (T). The impulsive force exciting the free end of bar is as described in Table 2.12. The grid size independency heat transfer and flexural studies were carried to determine the optimum grid size of the bar. It was found that 572 elements are required to simulate accurately the flexural behavior of the bar; however, for the purpose of producing a better presentation for the temperature contours of the bar, when subjected to welding at different locations, a higher number of elements were used. The numbers of elements used for finding the results when the bar is heated at  $x = 0, 0.25, 0.5$  and  $0.75l$  were respectively 572, 1,002, 994 and 983 elements. The integration time step independency tests were as well conducted and the value of 0.0006 s was used in the study for performing the time integrations. The Newmark ANSYS time integration method for implicit transient analysis was employed [27]. The dimensions for the uniform bar are as follows: 0.15 m for length,  $l$ , 0.05 m for width,  $w$ , and 0.0015 m for thickness,  $h$ . The fundamental natural frequency was calculated according to Eq. (2.87) and found to be equal to 26.436 rad/s. The damped natural frequency is calculated according to the following formula [30]:

$$\omega_d = \omega_{fundamental} \sqrt{1 - \zeta^2} \quad (2.88)$$

where  $\zeta$  is the damping coefficient of the uniform bar and taken as 0.015 for the uniform bar. The resulting damped natural frequency is 26.433 rad/s. For the sake of validating the numerical results, the damped natural frequency was calculated for the case when the bar was simulated under no heating conditions (when the temperature is equal to 300 K and the corresponding elasticity is equal to 1.2 GPa), The resulting damped time period was found as 0.238 s and the corresponding damped natural frequency ( $\omega_{d, \text{numerical}} = 2 \times \pi / \text{damped time period}$ ) is

**Fig. 2.45** Elastic modulus versus temperature curve [29]



**Table 2.12** Description of the impulsive loads employed in the present study

Location of heating source	Heating time at which impulsive load is applied (s)	Amplitude of impulsive load, F (N)	Duration of impulsive load (s)
0l	2.5	1	0.001
1/3	2.5	1	0.001
1/2	2.5	1	0.001
2l/3	2.5	1	0.001

calculated to be 26.363 rad/s. The percentage difference between the results of the analytical solution and the numerical damped natural frequencies, obtained from ANSYS simulation, for the uniform bar is found to be 0.07 %.

### 2.9.2 Results and Discussion

Heating of a bar, resembling the situation immediately after the electric resistance welding process and the effect of the location of the heated region on the flexural motion of the bar are examined. It should be noted that in a simulation, a heat source, resembling immediately after the welding process is applied at a particular x-axis location and along the y-axis of the plate. The location subjected to welding is treated as one of the boundary conditions, by fixing the temperature of the welding location to the metal melting temperature,  $T_m$ , at all the nodes of the welding location. In ANSYS, this can be done by defining a thermal load function at all the time points of the desired solution and the value of the thermal load function will always be equal to the melting temperature of the metal. The transient effects across the plate due to the welding process in the y and z directions are incorporated in solving the heat conduction equation [Eq. (2.83)]. Figure 2.46 shows temperature distribution at different locations in the plate, while Fig. 2.47 shows temperature variation along the dimensionless axial length ( $x/l$ ) at different locations in the plate. Since the temperature heat source is considered, temperature attains high values at the locations of the heat source and decays sharply as the distance in the vicinity of the heat source increases in the axial direction (along the x-axis). Although convection boundary is considered at the top and bottom

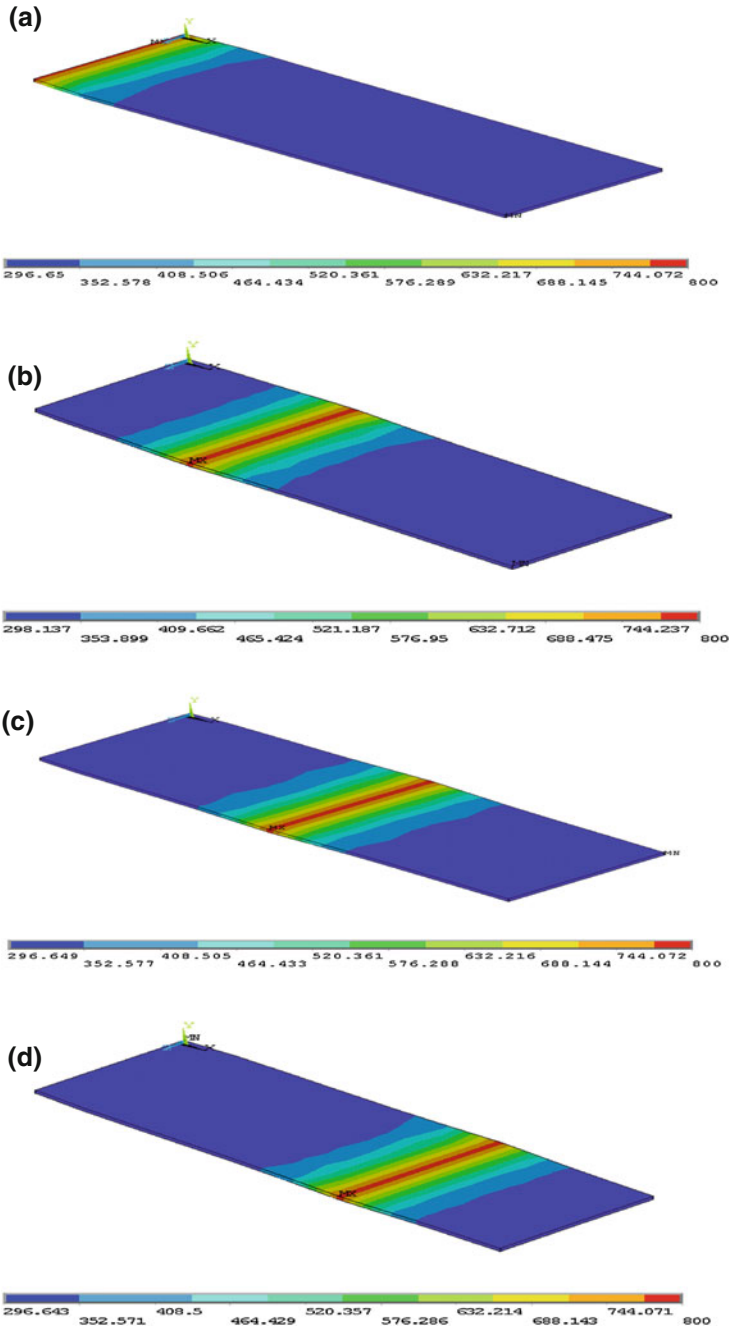


**Fig. 2.46** Temperature contours of plate for different heating locations [29]. **a** Heating location at  $x = 0l$ . **b** Heating location at  $x = l/3$ . **c** Heating location at  $x = l/2$ . **d** Heating location at  $x = 2l/3$

**Fig. 2.47** Spatial variations of temperature at plate mid-plane ( $y = 0.5 w, z = 0.5 h$ ) for different locations of heating [29]

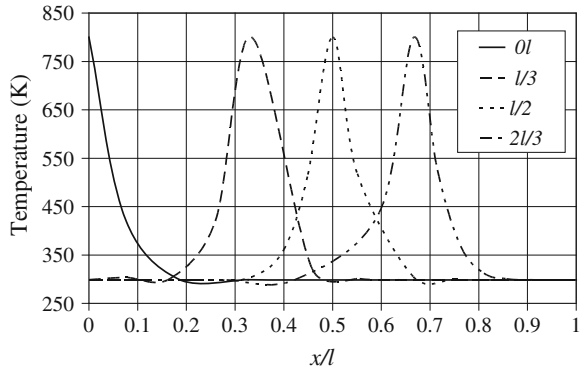
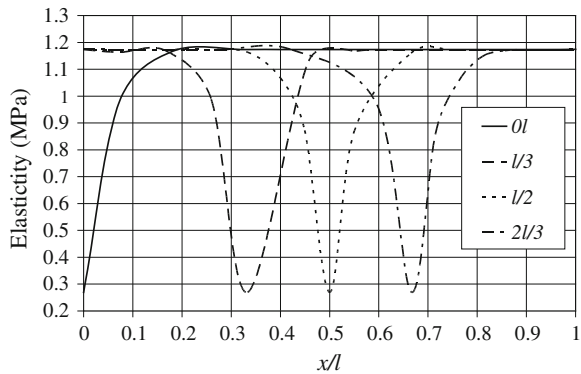


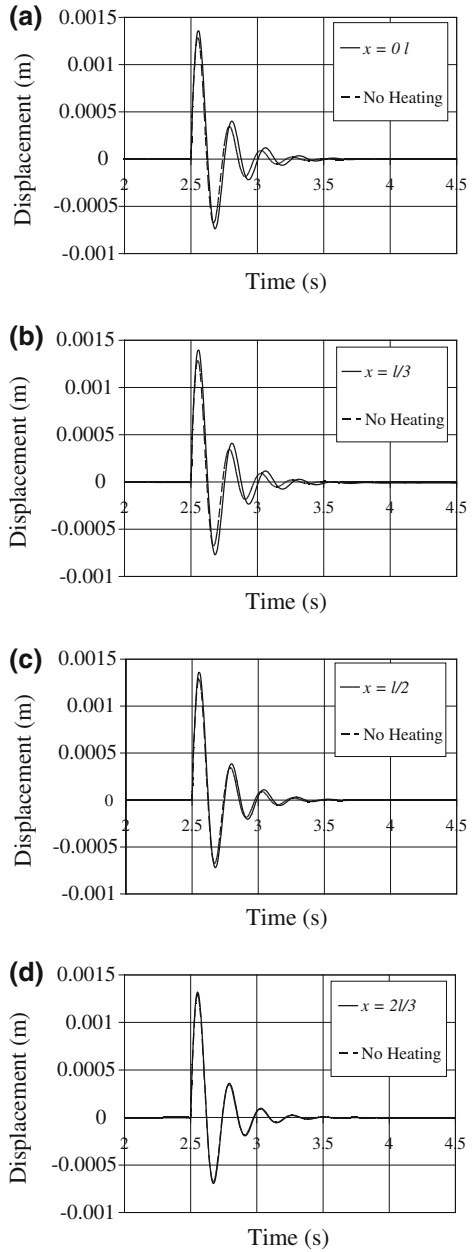
**Fig. 2.48** Spatial variations of elasticity at plate mid-plane ( $y = 0.5 w, z = 0.5 h$ ) for different locations of heating [29]



surfaces of the plate, heat transfer through diffusion in the plate is dominant. This is because of the magnitude of the heat transfer coefficient at the surface, which is low, i.e. in the order of  $10 \text{ W/m}^2 \text{ K}$  due to the natural convection. Since the heat source is considered to be at constant temperature, the temperature gradient becomes the same in the region front and back of the heat source. This results in similar elastic modulus variation around the heat source. This situation is seen from Fig. 2.48, in which elastic modulus of the substrate material is shown in the axial direction (along the x-axis). It should be noted that the elastic modulus is considered to be temperature dependent. Moreover, the location of the heat source is changed along the axial distance for the each case simulated. Consequently, for each case, elastic distribution varies similarly along the x-axis, provided that the location of the maximum elastic modulus changes along the x-axis for the each case.

Figure 2.49 shows tip displacement of the plate (at  $x = l$ ) due to the flexural motion resulted through the applied force. It should be noted that for each case, where the location of the heat source is changed along the axial distance, with heating and no-heating situations are considered. The resulting displacements for no-heating and heating situations are plotted in each figure. Since the cantilever

**Fig. 2.49** Flexural motion of plate tip (at  $x = 1$ ) for different sizes of constant heat source [29]. **a** Heating location at  $x = 0l$ . **b** Heating location at  $x = 1/3$ . **c** Heating location at  $x = 1/2$ . **d** Heating location at  $x = 2/3$



arrangement of the plate is considered and the load is applied at the free end of the plate, the flexural displacement is the maximum at the free end of the plate. The small difference in the displacement is observed with heating and no-heating

situations. This difference diminishes where location of the heat source is moved to  $x = 2l/3$ . In addition, small shift in the frequency of the flexural displacement is observed. It also diminishes for the heat source locations at  $x = 2l/3$ . This indicates that the location of the heat source in the plate modifies the flexural wave characteristics of the plate due to change of elastic modulus with temperature.

## 2.10 Laser Welding of Cantilever Plate: Influence of Speed of the Heating Source

The mathematical analysis and the findings for laser welding of cantilever plate are presented below in line with the previous study [32]. Consider the flexural characteristics of the cantilever plate, which is heated by a moving source at fixed end. The influence of the moving heat source speed, located at the fixed end, on the flexural characteristics of the cantilever plate is computed using the finite element method. The plate is excited by an impulsive force at the free end. In the analysis, temperature dependent Young's modulus is accommodated to simulate the nonlinear effect of the Young's modulus on the amplitude and the time shift of the flexural motion of the plate. The simulations are repeated for three heat source speeds.

### 2.10.1 Mathematical Modeling and Numerical Solution

In the analysis, a flat plate with cantilever arrangement (length,  $L = 0.075$  m, height,  $H = 0.00075$  m, and width,  $W = 0.025$  m), as shown in Fig. 2.50, is considered. The flexural impulsive load at the free end of the plate is introduced.

In finite element domain the flat solid is divided into SOLID98 ANSYS elements, which is a coupled-field 10-node tetrahedral element. It has quadratic displacement behavior, is introduced. Each of the ten nodes has 3 structural (translations:  $u_x$ ,  $u_y$  and  $u_z$ ), and one thermal degrees of freedom at each node (temperature,  $T$ ) [27]. The transient diffusion equation based on the Fourier heating model can be written in the Cartesian coordinates as:

$$\rho c_p \frac{\partial T}{\partial t} = k \left( \frac{\partial^2 T}{\partial x^2} + \frac{\partial^2 T}{\partial y^2} + \frac{\partial^2 T}{\partial z^2} \right) \quad (2.89)$$

where  $\rho$  is the density,  $c_p$  is the specific heat capacity and  $k$  is the thermal conductivity. The finite element, in matrix form, description of the flexural motion of the flat solid is written as:

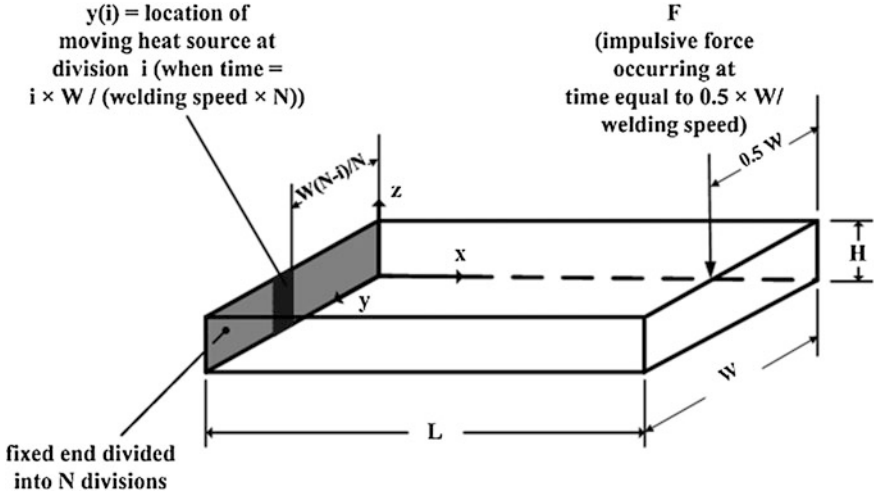


Fig. 2.50 The cantilever plate [32]

$$[M_e^s] [\ddot{U}_e] + [C_e^s] [\dot{U}_e] + [K_e^s] [U_e] = [F_e^{th}] + [F_e^{nd}] \quad (2.90)$$

where,

$[M_e^s]$  = element mass matrix

$[U_e]$  = nodal displacement vector of element

$[C_e^s]$  = structural damping matrix

$[K_e^s]$  = element stiffness matrix

$[F_e^{th}]$  = element thermal load vector

$[F_e^{nd}]$  = vector of nodal forces applied to the element

The modulus of elasticity of the cantilever plate material varies with temperature and is given as follows:

$$E = (10^{16} \times T^6) - (4 \times 10^{13} \times T^5) + (0.006 \times T^4) - (20 \times T^3) + (20,000 \times T^2) - (9 \times 10^6 \times T) + 3 \times 10^9 \quad (2.91)$$

where E is in Pascal and T in Kelvin.

At the free surfaces of the cantilever, a convective boundary is assumed. Initially the substrate material is assumed to be at a reference temperature equal to the room temperature. The moving heat source along the width of the plate (in the y-direction) at the fixed end, where the heating action due to the welding process takes place, is simulated as follows:

The width of the plate at the fixed end, W, is divided into equal number of divisions, N, where the area of each division is equal to  $H \times W/N$ .

An index is assigned to each of the divisions i.e.;  $i = 1, 2, \dots, N$ , where the starting location for each of the divisions in the y-direction is  $y(i) = (W/N) \times (N - i)$ .

The overall heating time is divided into equal number of time steps, each of is equal to  $W/(\text{welding speed} \times N)$ . When the moving heat source reaches to a division at a time equal to  $i \times W/(\text{welding speed} \times N)$ , as shown in Fig. 2.50, the temperature of all the finite element nodes at the surface of the division (at  $x = 0$ ) is fixed to a temperature equal to the melting temperature of the metal (800 K) for a time duration equal to a single time step ( $W/(\text{welding speed} \times N)$ ).

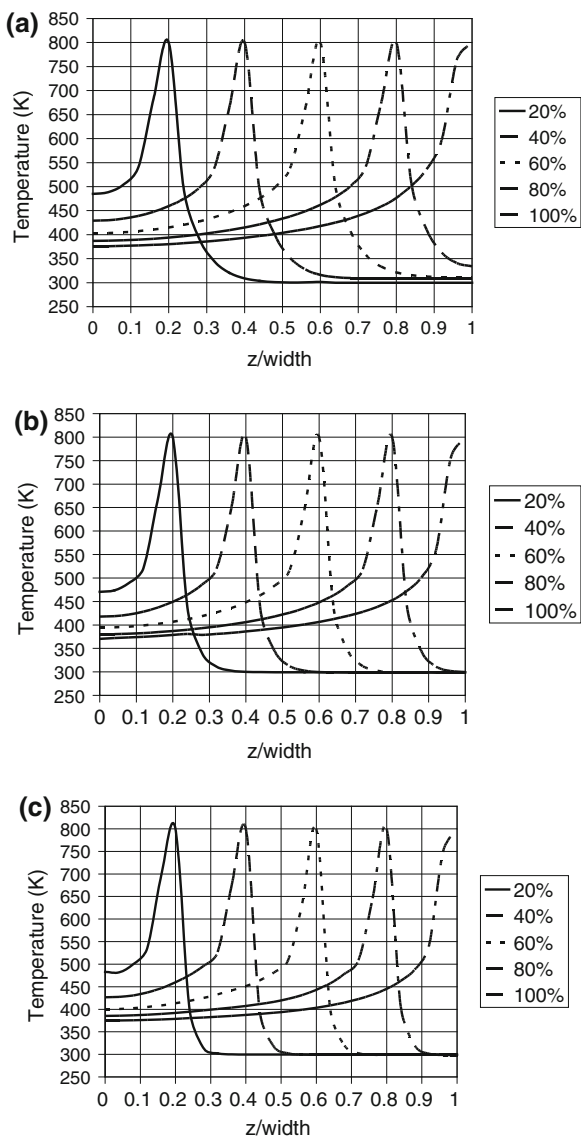
The plate material has the following properties: 53 W/m K for thermal conductivity, 520 J/kg K for specific heat,  $1.5 \times 10^{-5}$  for thermal expansion coefficient, 7,880 kg/m<sup>3</sup> for density and 0.01 for damping coefficient. At the fixed end, the displacement in all directions is always zero. The impulsive load duration is 0.01 s and was applied at a time equal to 50 % of total heating time ( $= 0.5 \times W/(\text{welding speed})$ ) after starting the heating process (Fig. 2.50).

### 2.10.2 Results and Discussion

In this case the flexural motion of the one side-heated cantilever plate is considered. A moving heat source is considered to resemble the laser heating situations in relation to welding. The influence of the heated zone on the resulting temperature field and the dynamic motion of the plate excited by an impulsive force from the free end are examined.

Figure 2.51 shows temperature distribution along the z-axis, where the heat source movement takes place, for different heating periods and moving heat source speeds, while Fig. 2.52 shows the contour plots of temperature for the same time periods and heat source speeds. Temperature rises to reach its maximum and decays sharply for all time periods and heat source speeds. However, the temperature gradient changes from low to high at temperature about 500 K. This change is more pronounced for the low speed when the heating is completed (heat source reaches to the other end along the plate width). This is because of the initial heating of the distance along the width during the movement of the heat source. Moreover, the temperature gradient in the region before the attainment of the maximum temperature is different than in the region during the decay of temperature from its maximum. This is because of the unheated region in front of the moving heat source. In this case, heat diffusion for the moving heat source to the area in front of the source is not considerable due to short time period. Consequently, temperature decays sharply in front of the moving heat source resulting in the high temperature gradient in this region. This situation is the same for all moving heat source speeds. It should be noted that in the frontal region of the moving source, gradual decay of temperature is observed, which starts at about 400 K. However, this decay changes with the heat source speed; in which case,

**Fig. 2.51** Temperature variation in the welding direction ( $z$ ) at different stages of the total welding time [32]. **a** Welding speed = 1 cm/s. **b** Welding speed = 2 cm/s. **c** Welding speed = 3 cm/s



increasing moving heat source speed enhances temperature rise and decay along the  $z$ -axis.

Figure 2.53 shows the displacement at the free end of cantilever for three moving heat source speeds. It should be noted that the displacements with and without heating situations are given for the comparison reason. The time shift between the flexural responses with heating and without heating situations is due to the time for the impacting force applied at the free end of the plate. In this case, when heat source reaches to half of the plate width the impact force was applied.

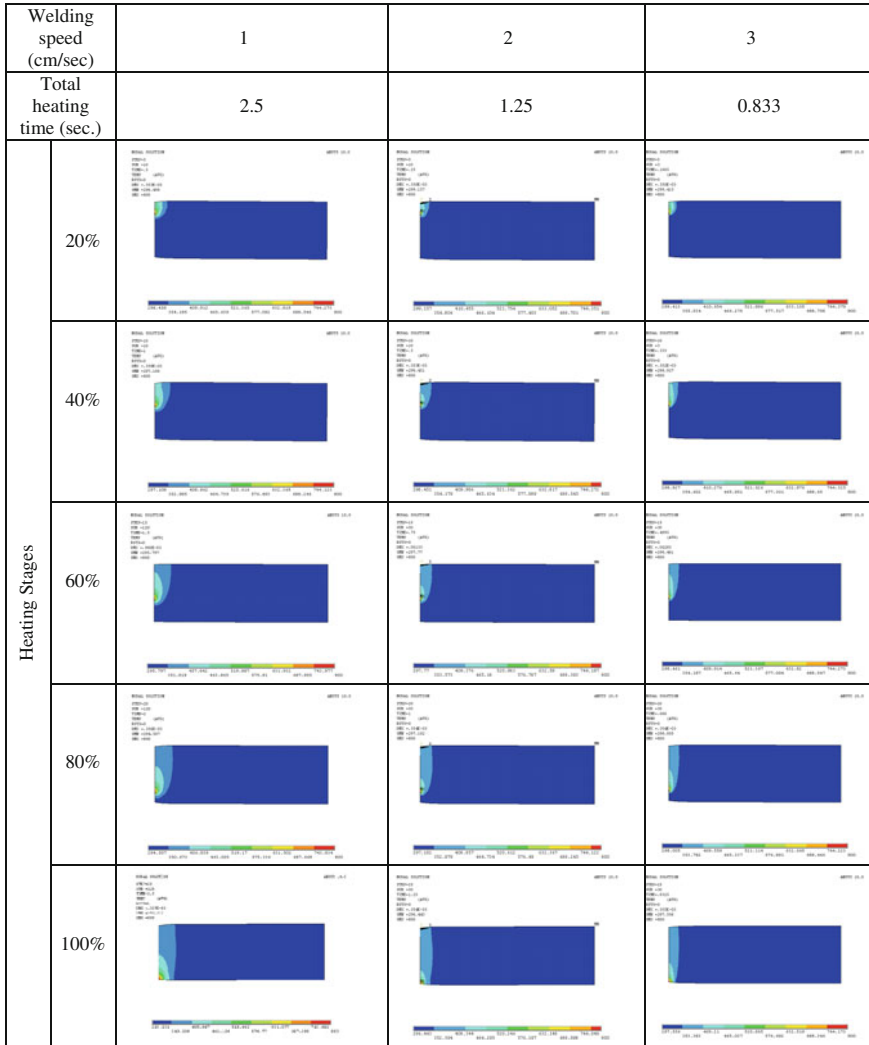
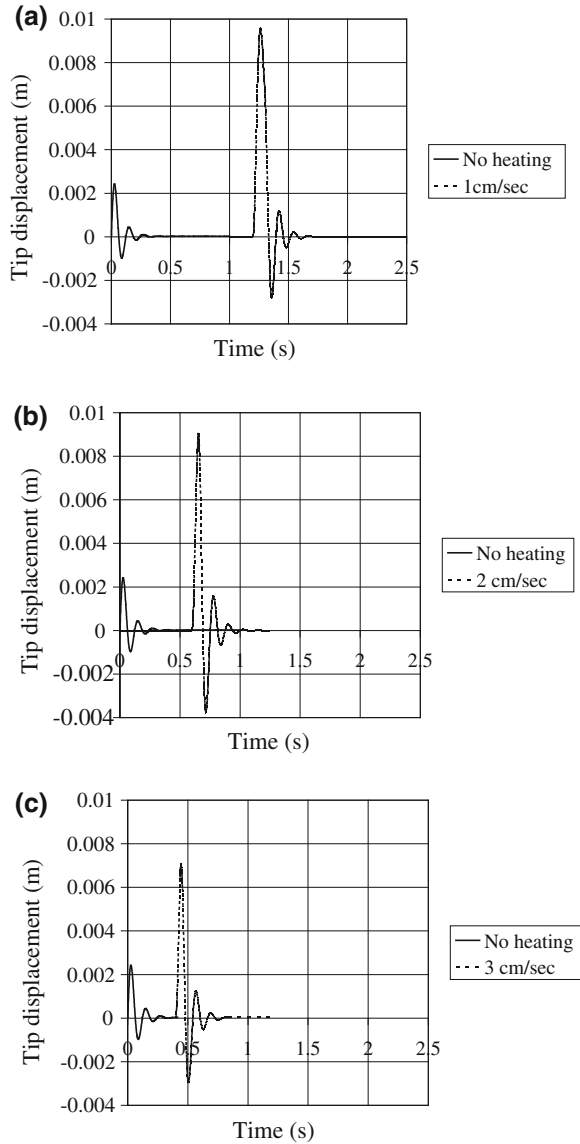


**Fig. 2.52** Temperature contours of the heated plate at different heating stages according to three welding speeds [32]

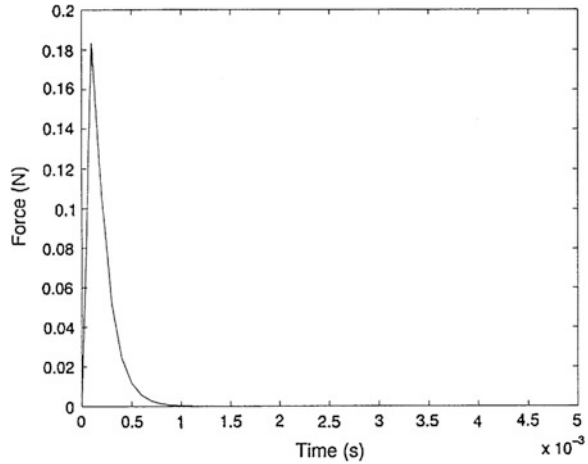
Moreover, the displacement corresponding to the heating situation is significantly larger than the without heating situation. This is because of the elastic modulus of the plate material, which changes with temperature. Once the speed of the heating source is increased, the time difference between displacements due to heating and without heating situations becomes less. This is because of the time taken for the heat source reaching at the mid of the plate width becomes less. The magnitude of the displacement reduces with increasing heat source speed. This can be explained in terms of the temperature field. In this case, heat diffusion to the solid bulk

**Fig. 2.53** Flexural response of the plate tip when the plate is heated according to different welding speeds [32].  
**a** Welding speed = 1 cm/s.  
**b** Welding speed = 2 cm/s.  
**c** Welding speed = 3 cm/s



enhances with low heat source speed due to increased time for the energy transfer via conduction from the moving heat source for the solid bulk in the plate becomes smaller for the high heat source speeds. Consequently, high temperature region extends into the solid bulk for low heat source speed. This, in turn, modifies the elastic modulus of the plate material in a large region where temperature is high. Therefore, the magnitude of displacement increases for low heat source speed due to modification of the elastic modulus in a large region of the plate.

**Fig. 2.54** Force input applied on the workpiece [33]



## 2.11 Laser Pulse Heating of Two-Layer Assembly

In the following analysis of the flexural characteristics of the two-layer assembly, the formulation and findings of the previous study [33] are considered. In this case laser evaporative heating of the cantilever workpiece consisting of two layers is considered. The first layer is Inconel 625 alloy, which can be formed by the high-velocity oxygen fuel (HVOF) coating with thicknesses in the range of 200  $\mu\text{m}$ , and the second layer is 1 mm thick stainless steel. The recoil pressure and the loading force are formulated analytically. The flexural motion of the workpiece is modelled and wave motion is predicted numerically. The simulations are repeated for four thicknesses of the first layer. The influence of the thickness layer on the displacement of the resulting flexural motion is discussed.

### 2.11.1 Heat Transfer Analysis

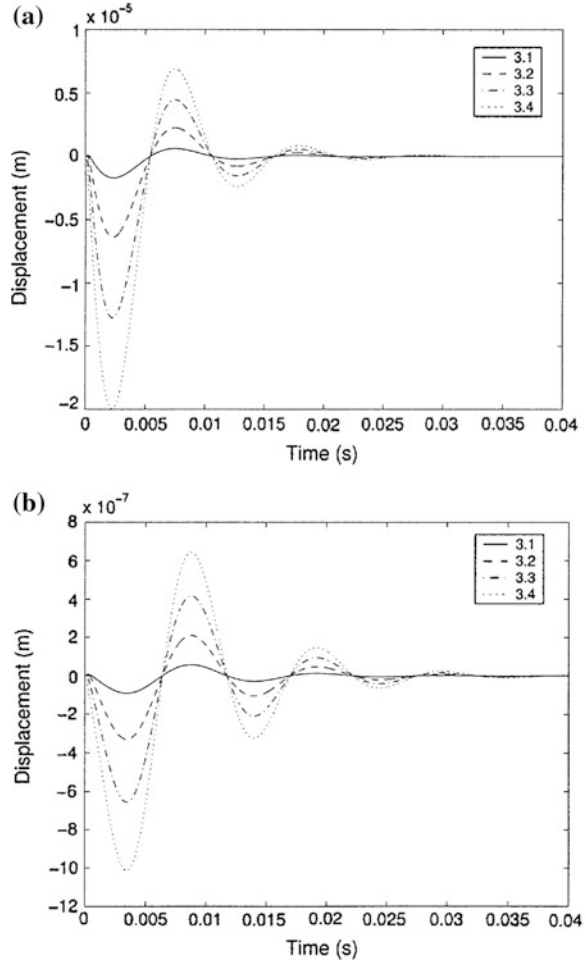
Figure 2.54 shows the normal pressure force of laser power intensity distribution. The heat transfer analysis is given above in Eqs. (2.20)–(2.24).

The pressure force acting normal to the substrate surface can be written as

$$F_0 = \int_0^{r_e} 2\pi r P dr \tag{2.92}$$

where  $r_e$  is the Radius of evaporated surface ( $r_e = 0.4 \text{ mm}$ ). The variation of normal pressure force with time is assumed to be exponential, i.e.

**Fig. 2.55** **a** Displacement response of the cantilever beam for a top layer thickness of 180 μm. **b** Difference in displacement response of the cantilever beam for a top layer thickness of 180 μm [33]



$$F(t) = F_0[\exp(-\beta t) - \exp(-\gamma t)]$$

where  $\beta$  and  $\gamma$  are constants.

### 2.11.2 Flexural Wave Analysis

The finite element method (FEM) is applied as a numerical tool for the analysis of flexural wave behavior for a workpiece as shown in Fig. 2.55. The rectangular finite elements for the workpieces contain pseudo-internal degrees of freedom (DOF). The internal DOF are for better representation of bending moments

generated by the external actuators and are condensed into the physical DOF using Guyan reduction technique [12].

Hamilton's principle is given by

$$\delta \int_{t_1}^{t_2} (K_i - \Pi) dt = 0 \quad (2.93)$$

$K_i$  in the above equation is the kinetic energy defined as

$$K_i = \frac{1}{2} \int_V \rho \dot{\mathbf{u}}^T \dot{\mathbf{u}} dV \quad (2.94)$$

In Eq. (2.93), the potential energy  $\Pi$  is given by

$$\Pi = - \int_V \mathbf{u}^T \mathbf{P}_b dV - \int_S \mathbf{u}^T \mathbf{P}_s dS - \mathbf{u}^T \mathbf{P}_c \quad (2.95)$$

$\mathbf{P}_b$  is the vector of body forces applied to volume  $V$ ,  $\mathbf{P}_s$  is the vector of surface force and  $\mathbf{P}_c$  is the concentrated load vector.

The following relations are defined for the finite element formulation:

$$\mathbf{u}_e = N_u \mathbf{u}_i$$

where  $N_u$  is the shape function matrix and  $\mathbf{u}_i$  is the vector of nodal displacement. The subscript 'e' in the equations stands for the element. Relating strain to displacement

$$S_e = L_u \mathbf{u}_e = [L_u N_u] \mathbf{u}_i = B_u \mathbf{u}_i$$

where  $S_e$  is the elemental strain and  $L_u$  is the differential operator which is given by

$$L_u = \begin{bmatrix} \frac{\partial}{\partial x} & 0 & 0 \\ 0 & \frac{\partial}{\partial y} & 0 \\ 0 & 0 & \frac{\partial}{\partial z} \\ \frac{\partial}{\partial y} & \frac{\partial}{\partial x} & 0 \\ 0 & \frac{\partial}{\partial z} & \frac{\partial}{\partial y} \\ \frac{\partial}{\partial z} & 0 & \frac{\partial}{\partial x} \end{bmatrix} \quad (2.96)$$

Substituting the above equations in (2.93) gives

$$M_{uu}\ddot{\mathbf{u}} + K_{uu}\mathbf{u} = \mathbf{F} \quad (2.97)$$

where the element matrices and vectors are given by

$$M_{uu} = \int_{V_e} \rho N_u^T N_u dV : K_{uu} = \int_{V_e} B_u^T c B_u dV$$

$$\mathbf{F}_e = \int_{V_e} N_u^T \mathbf{P}_b dV + \int_{S_e} N_u^T \mathbf{P}_s dS + N_u^T \mathbf{P}_c$$

For a rectangular element of size ( $2a \times 2b \times 2c$ ), the shape functions are given as

$$N_1 = \frac{1}{8} \left(1 - \frac{x}{a}\right) \left(1 - \frac{y}{b}\right) \left(1 + \frac{z}{c}\right) \quad N_2 = \frac{1}{8} \left(1 + \frac{x}{a}\right) \left(1 - \frac{y}{b}\right) \left(1 + \frac{z}{c}\right)$$

$$N_3 = \frac{1}{8} \left(1 + \frac{x}{a}\right) \left(1 + \frac{y}{b}\right) \left(1 + \frac{z}{c}\right) \quad N_4 = \frac{1}{8} \left(1 - \frac{x}{a}\right) \left(1 + \frac{y}{b}\right) \left(1 + \frac{z}{c}\right)$$

$$N_5 = \frac{1}{8} \left(1 - \frac{x}{a}\right) \left(1 - \frac{y}{b}\right) \left(1 - \frac{z}{c}\right) \quad N_6 = \frac{1}{8} \left(1 + \frac{x}{a}\right) \left(1 - \frac{y}{b}\right) \left(1 - \frac{z}{c}\right)$$

$$N_7 = \frac{1}{8} \left(1 + \frac{x}{a}\right) \left(1 + \frac{y}{b}\right) \left(1 - \frac{z}{c}\right) \quad N_8 = \frac{1}{8} \left(1 - \frac{x}{a}\right) \left(1 + \frac{y}{b}\right) \left(1 - \frac{z}{c}\right)$$

Internal DOF are added to the element to give a better representation to the bending moments caused by the piezoelectric effects. Two shape functions are defined for this purpose, which are given as follows:

$$N_9 = \frac{a^2 - x^2}{a^2} \quad N_{10} = \frac{b^2 - y^2}{b^2} \quad N_{11} = \frac{c^2 - z^2}{c^2}$$

The shape functions vanish at the element boundaries when  $x = \pm a$  and  $y = \pm b$ . The displacement vector,  $\mathbf{u}_e$ , is now expressed as

$$\mathbf{u}_e = N_u \mathbf{u}_i + X \mathbf{a}_j \quad (2.98)$$

The strain vector,  $\mathbf{S}_e$ , is now written as

$$\mathbf{S}_e = B_u \mathbf{u}_i + Y \mathbf{a}_j \quad (2.99)$$

where  $\mathbf{a}_j$  is the added generalized coordinate vector and  $X$  and  $Y$  in the above equations are given by

$$X = \begin{bmatrix} 0 & 0 & 0 \\ 0 & 0 & 0 \\ N_9 & N_{10} & N_{11} \end{bmatrix} \quad \text{and} \quad Y = L_u X = \begin{bmatrix} 0 & 0 & 0 \\ 0 & 0 & 0 \\ 0 & 0 & \frac{-2z}{c^2} \\ 0 & 0 & 0 \\ 0 & \frac{-2y}{b^2} & 0 \\ \frac{-2x}{a^2} & 0 & 0 \end{bmatrix} \quad (2.100)$$

The new matrix,  $K_{uu}^*$  is the global elastic stiffness matrix which is composed of  $[K_{uu}]_e^*$  and given by

$$[K_{uu}]_e^* = [K_{uu}]_e - [K_{ua}]_e [K_{aa}]_e^{-1} [K_{au}]_e \quad (2.101)$$

where  $[K_{ua}]_e$  and  $[K_{aa}]_e$  are partitioned stiffness matrices which is given by

$$[K_{ua}]_e = \int_V B_u^T c Y dV \quad \text{and} \quad [K_{aa}]_e = \int_V Y^T c Y dV \quad (2.102)$$

where C is a constant matrix. Hence the final equation becomes

$$M_{uu} \ddot{u} + K_{uu}^* u = F \quad (2.103)$$

### 2.11.2.1 Initial and Boundary Conditions

Initially, the displacements are set to zero for the cantilever case. Also, at  $x = 0$ , i.e. at the fixed end, the displacement is always zero, which is given as at  $x = 0$ ,  $u = 0$ .

### 2.11.2.2 Method of Solution

In the finite element analysis, the workpiece is divided into 16 elements where the number of divisions are uniform in both  $x$  and  $z$  directions and the thickness is considered to be uniform. The elemental stiffness and mass matrices are determined, which are then assembled to yield the global matrices.

### 2.11.2.3 State-Space Method

The equation of motion is converted into state-space form. For a deterministic system, it is given as

$$\dot{z} = Az + BF \quad (2.104)$$

$$\mathbf{u} = Cz \quad (2.105)$$

where  $z$  is the complete state vector and  $u$  is the required displacement.  $A$ ,  $B$  and  $C$  are the system, input and output matrices respectively, given as

$$A = \begin{bmatrix} 0 & I \\ -M_{uu}^{-1}K_{uu} & -M_{uu}^{-1}C_{uu} \end{bmatrix} \quad \text{and} \quad B = \begin{bmatrix} 0 \\ -M_{uu}^{-1}F \end{bmatrix} \quad (2.106)$$

where  $C_{uu}$  is the proportional damping introduced through the following equations:

$$C_{uu} = \alpha M_{uu} + \beta K_{uu}$$

$\alpha$  and  $\beta$  in the above equation are the damping coefficients.  $C$  in Eq. (2.105) is a matrix defining the location where displacement is required.

These matrices are introduced through Matlab code and simulated for a given force and time interval to obtain the displacement  $u$  at various locations.

#### 2.11.2.4 Determination of Stresses

The strain for a given element is given by  $\mathbf{S}_e = B_u \mathbf{u}_e$ , where  $B_u = L_u N_u$  and  $N_u$  is given by

$$N_u = \begin{bmatrix} N_1 & 0 & 0 & N_2 & 0 & 0 & N_3 & 0 & 0 & N_4 & 0 & 0 & N_5 & 0 & 0 & N_6 & 0 & 0 & N_7 & 0 & 0 & N_8 & 0 & 0 \\ 0 & N_1 & 0 & 0 & N_2 & 0 & 0 & N_3 & 0 & 0 & N_4 & 0 & 0 & N_5 & 0 & 0 & N_6 & 0 & 0 & N_7 & 0 & 0 & N_8 & 0 & 0 \\ 0 & 0 & N_1 & 0 & 0 & N_2 & 0 & 0 & N_3 & 0 & 0 & N_4 & 0 & 0 & N_5 & 0 & 0 & N_6 & 0 & 0 & N_7 & 0 & 0 & N_8 & 0 \end{bmatrix}$$

The stress is obtained using the stress–strain relationship which is given by  $\sigma_e = E\mathbf{S}_e$ . These elemental stresses are properly mapped with respect to global node numbering to obtain the global stress. The so obtained global stress  $\sigma$  is given by

$$\sigma = \begin{bmatrix} \sigma_x \\ \sigma_y \\ \tau_{xy} \\ \tau_{yz} \\ \tau_{xz} \end{bmatrix} \quad (2.107)$$

Hence, the equivalent stress is given by

$$\sigma_{eq} = \sqrt{0.5 [(\sigma_x - \sigma_y)^2 + (\sigma_y - \sigma_z)^2 + (\sigma_x - \sigma_z)^2]} \quad (2.108)$$

**Table 2.13** Mechanical properties of steel and Inconel 625 used in simulations

	Steel	Inconel 625
E (Pa)	$2.068 \times 10^{11}$	$205.5 \times 10^9$
$\rho$ (kg/m <sup>3</sup> )	7,830	8,440
$\nu$	0.3	0.312

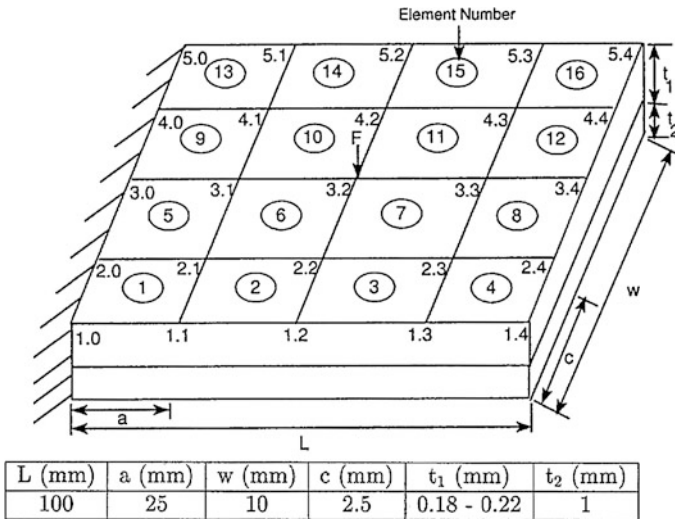
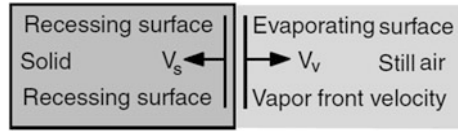


**Fig. 2.56** Layout and dimensions of the workpiece employed in simulations [33]

### 2.11.3 Results and Discussions

In this case laser ablation of the substrate surface and recoil pressure generation across the vapor front and the workpiece surface are presented. The flexural motion of the workpiece with a cantilever arrangement is modelled and frequency as well as magnitude of the wave are predicted. The workpiece is considered as consisting of two layers. The first layer is Inconel 625 alloy with thicknesses of about 200  $\mu\text{m}$ , which resembles the coating formed by HVOF, while the second layer is stainless steel with 1 mm thickness. The simulations are repeated with different thicknesses of the first layer. This provides information on the variation of the flexural wave characteristics with layer thickness and enables a prediction to be made of the coating thickness without destructive testing. Since the laboratory facilities are limited at present, the authors could not conduct the experiment in this regard. However, a high-speed laser velocimeter based on the reflection of the coated surface may be used to collect the beam data for the frequency and amplitude measurements of the workpiece oscillation; i.e. predictions may be validated using the measurement. Table 2.13 gives the properties of the layers employed in the simulations. Figure 2.54 shows the temporal variation of the

**Fig. 2.57** Schematic view of interface [34]



pressure force (loading force) determined from the recoil pressure and used in the analysis. The peak value of the load is in the order of 0.19 N.

Figure 2.55a shows displacement of the workpiece with time at different locations on the workpiece (where Fig. 2.56 shows the location and dimensions of the elements on the workpiece) while Fig. 2.55b shows the displacement difference for the first layer thickness of 180  $\mu\text{m}$ . The displacement difference corresponds to the displacement difference due to the workpiece with and without a first layer. The magnitude of displacement at different location changes; i.e. displacement corresponding to the location close to the free end of the workpiece (location 3.4 in Fig. 2.56) is higher than that corresponding to the fixed end (location 3.1). The displacement decays with time due to the cantilever arrangement of the workpiece. The maximum magnitude of displacement is of the order of 2 mm and the period of the wave motion is of the order of 0.012 s. The displacement difference (Fig. 2.55b) has a slightly higher period than that of the displacement, but its maximum magnitude is less than 1 mm. Consequently, the first layer, which is 180  $\mu\text{m}$  thick, results in a slight increase in frequency but a substantial increase in magnitude of the wave motion; i.e. the value increases to almost twice.

## 2.12 3D Analysis of Laser Evaporative Heated Cantilever Workpiece

The mathematical analysis and the findings for the 3D analysis of laser evaporative heated cantilever workpiece are presented below in line with the previous study [34]. The present case consider modeling the flexural motion and stress field inside the substrate material. The recoil pressure is integrated over an irradiated area to obtain a normal force, which initiates the flexural motion of the workpiece. When solving the wave and stress equations finite element method (FEM) is adopted. Steel plate is selected as a workpiece material while copper element is introduced in the workpiece to examine its influence on the flexural motion and stress field. In the analysis, cantilever arrangement of the workpiece is considered.

### 2.12.1 Heat Transfer Analysis

The irradiated surface due to receding surface is shown in Fig. 2.57. The heat transfer analysis is given above in Eqs. (2.20)–(2.24).

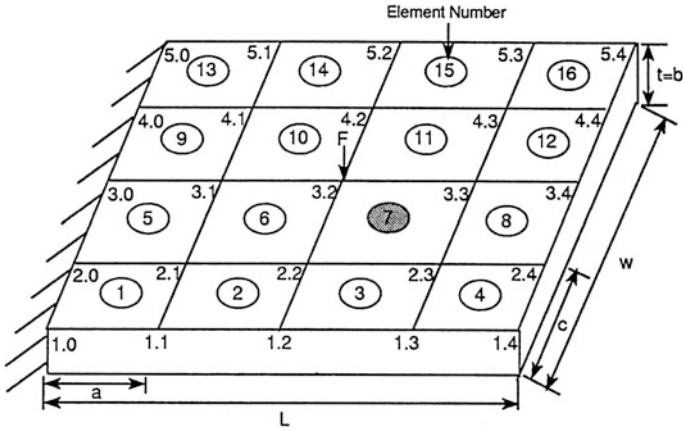
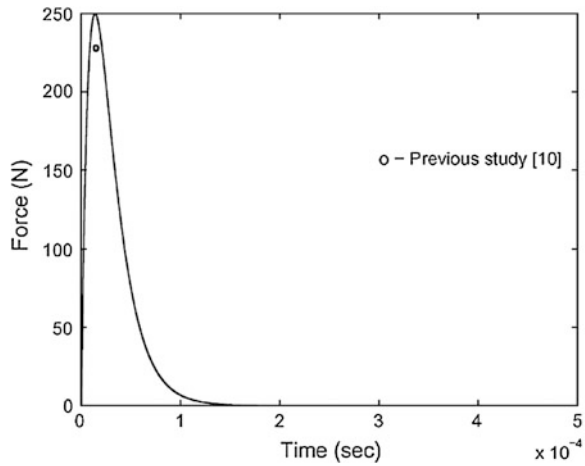


**Fig. 2.58** Schematic view of cantilever workpiece showing the seventh element as copper.  $a = 0.025$  m,  $c = 0.0025$  m;  $L = 0.1$  m,  $t = 0.002$  m,  $w = 0.01$  m [34]

**Table 2.14** Mechanical properties of steel and copper used in simulations

	Steel	Copper
E (Pa)	$2.068 \times 10^{11}$	$1.3 \times 10^{11}$
$\rho$ (kg/m <sup>3</sup> )	7,830	8,920
$\nu$	0.3	0.34

**Fig. 2.59** Force response [34]



The pressure predicted is given in the previous study [6]

$$P_v = 1.82 \times 10^{-3} \frac{\sqrt{C_p T_s I_0}}{[C_p(T_s - T_0) + L_{ev}]} \tag{2.109}$$

The unit in Eq. (2.109) is bar.

**Fig. 2.60** Displacement response of the cantilever beam [34]

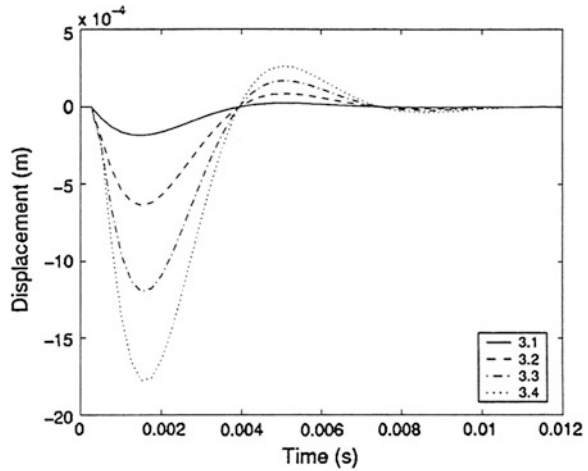
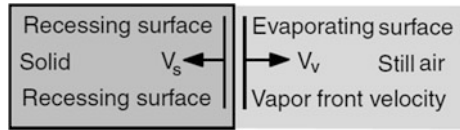


**Fig. 2.61** Schematic view of interface [35]



### 2.12.2 Flexural Wave Analysis

FEM is applied as a numerical tool for the analysis of flexural wave behavior for a workpiece as shown in Fig. 2.58. Flexural wave analysis is given above in Eqs. (2.93)–(2.108).

### 2.12.3 Results and Discussions

Laser induced flexural motion in cantilever steel plate is analyzed. Pressure force is considered to initiate the flexural motion of the workpiece. Table 2.14 gives the material properties used in the simulations. Figure 2.59 shows the variation of pressure force with time. The peak pressure force is in the order of 250 N, which acts normal to the surface of the workpiece. Since the evaporation process is time dependent, variation of pressure force with time is assumed as exponential. Figure 2.60 shows the temporal variation of displacement at different locations in the workpiece (elements) due to flexural motion while Fig. 2.58 shows the location of the elements. The magnitude of displacement is high at the free end of the workpiece and it is lowest close to the fixed end. This is due to the cantilever arrangement of the workpiece. Moreover, the frequency of oscillation is in the

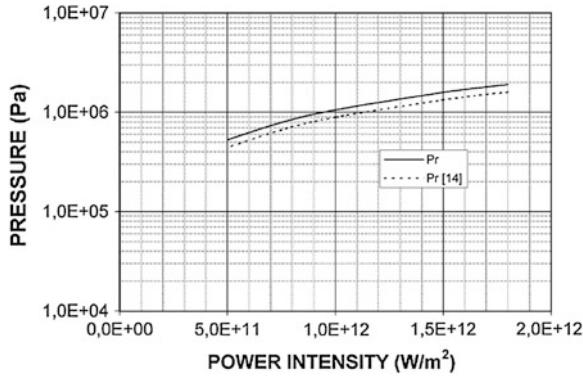


Fig. 2.62 Interface pressure with power intensity [35]

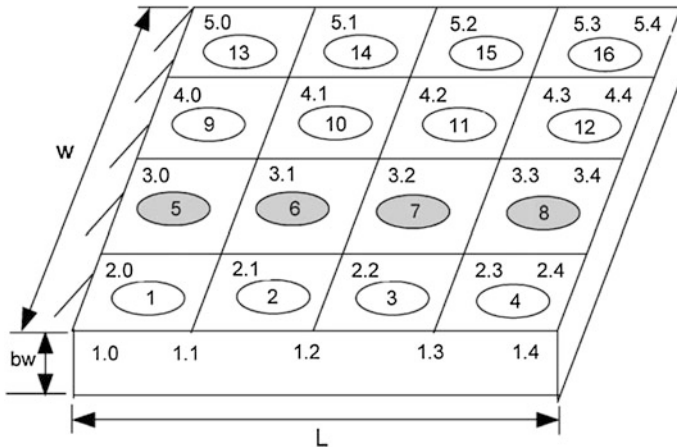


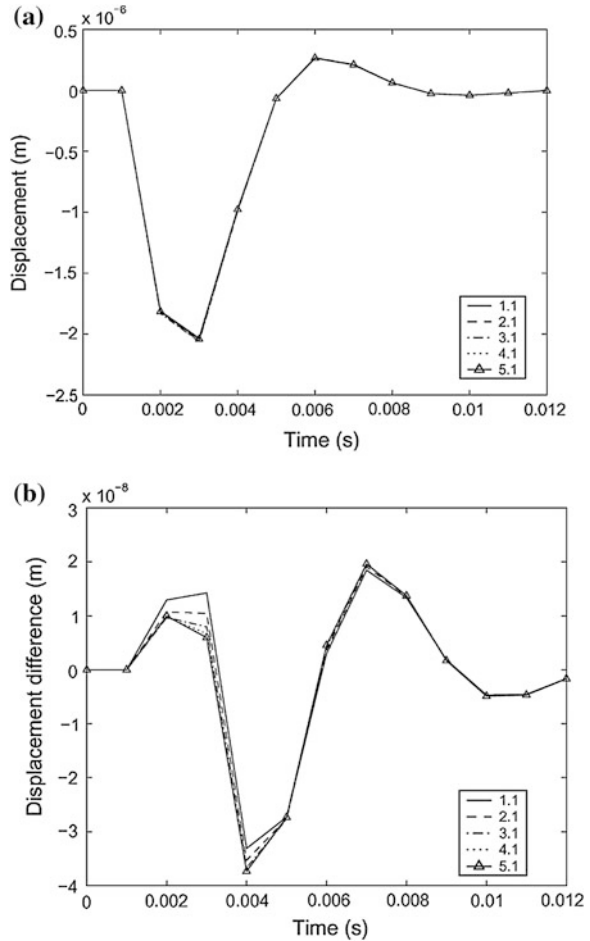
Fig. 2.63 Cantilever workpiece finite element model [35]

order of 0.2 kHz, provided that the oscillation dies out as the time progresses to 12 ms. The maximum displacement in the order of 20  $\mu\text{m}$  is resulted at around 3 ms. Due to the flexural motion of the workpiece, the stresses are developed.

### 2.13 Laser Induced Flexural Wave: Aluminum in Steel Substrate

In the following analysis of the flexural characteristics of the beam, the formulation and findings of the previous study [35] are considered. Laser induced flexural wave generation is considered in this case. The evaporation of the surface

**Fig. 2.64** **a** Displacement response in the transverse direction when aluminum is in the sixth position for the first points. **b** Difference in transverse displacement when aluminum is in the sixth position for the first points [35]



is modeled and the interface pressure acting at the vapor–solid interface is formulated. The flexural wave analysis is carried out in three-dimensional domain and resulting surface displacement is obtained for cantilever arrangement. The simulations are carried out for steel substrate with existence of locally imbedded single aluminum cell in the substrate material. In order to investigate the effect of aluminum cell on the resulting flexural wave displacement, the location of the cell is varied in the substrate material.

### 2.13.1 Heat Transfer Analysis

The schematic view of the interface is shown in Fig. 2.61. The heat transfer analysis is given above in Eqs. (2.20)–(2.24).

The irradiated surface due to receding surface is shown in Fig. 2.61.

The pressure predicted is given in the previous study [6].

$$P_v = 1.82 \times 10^{-3} \frac{\sqrt{C_p T_s I_0}}{[C_p(T_s - T_0) + L_{ev}]} \quad (2.110)$$

The unit in Eq. (2.110) is bar.

### 2.13.2 Flexural Wave Analysis

Flexural wave analysis is given above in Eqs. (2.93)–(2.108).

### 2.13.3 Results and Discussions

The flexural wave analysis during laser evaporation of the steel surface is considered. The interface pressure is formulated and the pressure force acting normal to the workpiece is employed as a loading force for the flexural wave generation. The geometric arrangement of the workpiece is a cantilever arrangement. The effect of locally imbedded aluminum element on the workpiece displacement is investigated. In order to comprehend the influence of the aluminum element on the temporal and spatial resolution of the displacement of the workpiece, the differences in the surface displacements corresponding to with and without additional element (aluminum cell) is considered, i.e.,

$$D_{\text{difference}} = D_{\text{without add. element}} - D_{\text{with add. element}}$$

where  $D_{\text{difference}}$  is the displacement difference of the surface,  $D_{\text{without add. element}}$  the displacement of the surface when there is no additional aluminum element imbedded in the workpiece and  $D_{\text{with add. element}}$  the displacement of the surface when the additional element is locally added in the substrate material.

Figure 2.62 shows the pressure predicted from the present and the previous studies [14]. The equation derived previously predicts the interface zone pressure as high as 500 kPa. The values of the pressure predicted from the present study agree well with the previous results. The finite element model of the cantilever workpiece is shown in Fig. 2.63.

Figure 2.64a shows the temporal variation of the surface displacement due to flexural wave motion at different mesh points and the differential element is at sixth location (Fig. 2.63). The displacement attains high values at certain periods, provided that it reaches its peak value at about 3 ms after the laser pulse ends. Moreover, as the time progresses, the magnitude of displacement reduces. The displacement corresponding to different locations in the transverse direction does not vary considerably. This indicates that the flexural motion of the surface at each

location along the transverse direction is almost identical. The displacement difference due to with and without aluminum element is shown in Fig. 2.64b for the same condition of Fig. 2.64a. The displacement difference reaches its peak value almost 4 ms after the laser pulse ends. Consequently, the time at which the peak values of displacement and displacement difference occur does not coincide. This is because of the aluminum element, which modifies slightly the mode of flexural motion of the surface.

## References

1. B.S. Yilbas, F. Mahmood, Flexural waves generated due to pressure force during the laser induced evaporation process. *J. Laser Appl.* **13**(3), 118–124 (2001)
2. B.S. Yilbas, A.Z. Sahin, R. Davies, Laser heating mechanism including evaporation process initiating laser drilling. *Int. J. Mach. Tools Manuf.* **35**, 1047–1062 (1995)
3. Y.V. Afanasev, O.N. Krokhin, Vaporization of matter exposed to laser emission. *Sov. Phys. JETP* **25**, 639–647 (1967)
4. B.S. Yilbas, Z. Yilbas, Some aspects of laser-metal vapour interaction. *Pramana J. Phys.* **31**, 365–381 (1988)
5. B.S. Yilbas, A.F.M. Arif, Laser short pulse heating and elastic–plastic wave generation. *Jpn. J. Appl. Phys.* **39**, 5879–5888 (2000)
6. M. Hugenschmidt, R. Schmitt, Pulsed laser-targets effects and high resolution process diagnostics. *Opt. Quantum Electron.* **27**, 1231–1242 (1995)
7. J.F. Doyle, *Wave Propagation in Structures* (Springer, New York, 1989)
8. F. Mahmood, Transient response of varying thickness Timoshenko beam under point load. M.Sc. thesis, Mechanical Engineering Department, KFUPM, Dhahran, 1999
9. B.S. Yilbas, S.J. Hyder, S.Z. Shuja, Flexural wave generation and stress analysis during laser evaporative heating of steel. *Proc. Inst. Mech. Eng. [C]* **216**, 531–542 (2002)
10. B.S. Yilbas, M. Sami, A. Al-Ferayedhi, Closed form and numerical solutions to the laser heating process. *Proc. Inst. Mech. Eng. [C]* **212**(C2), 141–151 (1998)
11. B.G. Loh, P.I. Ro, Changing the propagation direction of flexural ultrasonic progressive waves by modulating excitation frequency. *J. Sound Vib.* **238**, 171–178 (2000)
12. R.J. Guyan, Reduction of stiffness and mass matrices. *Am. Inst. Aeronaut. Astronaut. J.* **3**, 380–386 (1965)
13. B.S. Yilbas, M. Faisal, S.Z. Shuja, A.F.M. Arif, Laser pulse heating of steel surface and flexural wave analysis. *Opt. Lasers Eng.* **37**, 63–83 (2002)
14. S.Z. Shuja, B.S. Yilbas, Gas-assisted repetitive pulsed heating of a steel surface. *Proc. Inst. Mech. Eng. [C]* **212**, 741–757 (1998)
15. T.B. Gotski, M.Y. Hussaini, J.L. Lumley, *Simulation and Modeling of Turbulent Flows* (Oxford University Press, New York, 1996)
16. C.B. Scruby, L.E. Drain, *Laser Ultrasonics: Techniques and Applications* (Adam Hilger, Bristol, 1990)
17. F.P. Incropera, D.P. Dewitt, *Introduction to Heat Transfer F Appendix* (Wiley, New York, 1985), pp. 667–696
18. H.K. Versteeg, W. Malalasekera, *An Introduction to Computational Fluid Dynamics: The Finite Volume Method* (Longman Scientific and Technical, New York, 1995)
19. S.Z. Shuja, Simulation of three-dimensional gas-assisted heating of solid substance. Ph.D. thesis, Mechanical Engineering Department, KFUPM, Dhahran, 1998
20. B.S. Yilbas, Laser heating process and experimental validation. *Int. J. Heat Mass Transf.* **40**(5), 1131–1143 (1997)

21. S.V. Patankar, *Computer Analysis of Fluid Flow and Heat Transfer* (Swansea, Pinridge, 1981), pp. 223–252 (Chap. 8)
22. K.J. Bathe, *Finite Element Procedures* (Englewood Cliffs, NJ, Prentice-Hall, 1996), pp. 148–192 (Chap. 6)
23. B.S. Yilbas, S.J. Hyder, Laser pulse heating and flexural wave generation during treatment of metallic surfaces. *J. Mater. Process. Technol.* **141**, 1–8 (2003)
24. B.S. Yilbas, J. Hyder, Flexural motion due to laser ablation: influence of force location on the flexural motion. *Proc. Inst. Mech. Eng. [C]* **218**(12), 1411–1420 (2004)
25. B.S. Yilbas, J. Hyder, Influence of layers on flexural motion of multilayer assembly due to laser ablation process. *Proc. Inst. Mech. Eng. [C]* **217**, 945–954 (2003)
26. T. Al-Zaharnah, B.S. Yilbas, Effect of heat transfer on the flexural characteristics of cantilever plate heated at fixed end. *J. Mech.* **25**(1), 1–8 (2009)
27. ANSYS, Inc., Theory Reference, Release 10.0
28. I.T. Alzaharnah, S. Al-Kaabi, B.S. Yilbas, Effect of temperature field on flexural wave characteristics of a bar resembling welding to rigid body. *Adv. Mater. Res.* **83–86**, 1212–1219 (2010)
29. I.T. Alzaharnah, B. S. Yilbas, Investigation into flexural characteristics of a bar subjected to local heating: the effect of heat source location. *Proc. IMechE. [B]* **222**, 1355–1362 (2008)
30. W.T. Thomson, M.D. Dahleh, *Theory of Vibration with Applications*, 5th edn. (Prentice Hall, Englewood Cliffs, NJ, 1998)
31. A. Meirovitch, *Elements of Vibration Analysis*, 2nd edn (McGraw-Hill Book Company, 1986)
32. I.T. Alzaharnah, B.S. Yilbas, S.A. Al-Kaabi, Flexural characteristics of a laser welded cantilever plate: influence of speed of the heating source. *Lasers Eng.* **18**, 337–350 (2008)
33. B.S. Yilbas, S.J. Hyder, Analysis of flexural wave due to laser heating pulse: two-layer assembly case. *Proc Inst. Mech. Eng. [C]* **216**, 1165–1174 (2002)
34. S.J. Hyder, B.S. Yilbas, S.Z. Shuja, Flexural Motion in laser evaporative heated cantilever workpiece: three-dimensional analysis. *Opt. Quant. Electron.* **35**, 111–128 (2003)
35. S.J. Hyder, B.S. Yilbas, S.Z. Shuja, Laser induced flexural wave analysis: an aluminum element in steel substrate. *J. Mater. Process. Technol.* **136**, 24–34 (2003)



<http://www.springer.com/978-3-642-54976-2>

Flexural Testing of Weld Site and HVOF Coating  
Characteristics

Yilbas, B.S.; Alzaharnah, I.; Sahin, A.Z.

2014, XI, 167 p. 117 illus., 8 illus. in color., Hardcover

ISBN: 978-3-642-54976-2